

**GALACTIC MICROLENSING
BINARY-LENS LIGHT CURVE MORPHOLOGIES AND
RESULTS FROM THE ROSETTA SPACECRAFT BULGE
SURVEY**

Christine Elisabeth Liebig

**A Thesis Submitted for the Degree of PhD
at the
University of St Andrews**



2014

**Full metadata for this item is available in
Research@StAndrews:FullText
at:**

<http://research-repository.st-andrews.ac.uk/>

Please use this identifier to cite or link to this item:

<http://hdl.handle.net/10023/4881>

This item is protected by original copyright

**This item is licensed under a
Creative Commons License**

Galactic Microlensing

Binary-lens light curve morphologies and
results from the Rosetta spacecraft bulge survey

CHRISTINE ELISABETH LIEBIG

Submitted for the degree of

DOCTOR OF PHILOSOPHY IN ASTRONOMY

26th January 2014



University
of
St Andrews

Declaration

I, Christine Liebig, hereby certify that this thesis, which is approximately 20.000 words in length, has been written by me, that it is the record of work carried out by me and that it has not been submitted in any previous application for a higher degree.

Date

Signature of candidate

I was admitted as a research student in January 2010 and as a candidate for the degree of PhD in January 2010; the higher study for which this is a record was carried out in the University of St Andrews between 2010 and 2013.

Date

Signature of candidate

I hereby certify that the candidate has fulfilled the conditions of the Resolution and Regulations appropriate for the degree of PhD in the University of St Andrews and that the candidate is qualified to submit this thesis in application for that degree.

Date

Signature of supervisor

Copyright Agreement

In submitting this thesis to the University of St Andrews we understand that we are giving permission for it to be made available for use in accordance with the regulations of the University Library for the time being in force, subject to any copyright vested in the work not being affected thereby. We also understand that the title and the abstract will be published, and that a copy of the work may be made and supplied to any bona fide library or research worker, that my thesis will be electronically accessible for personal or research use unless exempt by award of an embargo as requested below, and that the library has the right to migrate my thesis into new electronic forms as required to ensure continued access to the thesis. We have obtained any third-party copyright permissions that may be required in order to allow such access and migration, or have requested the appropriate embargo below.

The following is an agreed request by candidate and supervisor regarding the electronic publication of this thesis:

Access to Printed copy and electronic publication of thesis through the University of St Andrews.

Date

Signature of candidate

Date

Signature of supervisor

Abstract

For 20 years now, gravitational microlensing observations towards the Galactic bulge have provided us with a wealth of information about the stellar and planetary content of our Galaxy, which is inaccessible via other current methods. This thesis summarises work on two research topics that arose in the context of exoplanetary microlensing, but we take a step back and consider ways of increasing our understanding of more fundamental phenomena: firstly, stellar microlenses in our Galaxy that were stereoscopically observed and, secondly, the morphological variety of binary-lens light curves.

In autumn 2008, the ESA Rosetta spacecraft surveyed the Galactic bulge for microlensing events. With a baseline of ~ 1.6 AU between the spacecraft and ground observations, significant parallax effects can be expected. We develop a photometry pipeline to deal with a severely undersampled point spread function in the crowded fields of the Galactic bulge, making use of complementary ground observations. Comparison of Rosetta and OGLE light curves provides the microlens parallax π_E , which constrains the mass and distance of the observed lenses. The lens mass could be fully determined if future proper motion measurements were obtained, whereas the lens distance additionally requires the determination of the source distance.

In the second project, we present a detailed study of microlensing light curve morphologies. We provide a complete morphological classification for the case of the equal-mass binary lens, which makes use of the realisation that any microlensing peak can be categorised as one of only four types: cusp-grazing, cusp-crossing, fold-crossing or fold-grazing. As a means for this classification, we develop a caustic feature notation, which can be universally applied to binary lens caustics. Ultimately, this study aims to refine light curve modelling approaches by providing an optimal choice of initial parameter sets, while ensuring complete coverage of the relevant parameter space.

Contents

Abstract	7
Table of Contents	10
I Galactic gravitational microlensing	11
1 Gravitational lensing	13
2 Microlensing fundamentals	17
2.1 Lens equation	17
2.2 Einstein ring	20
2.3 Lens magnification	21
2.4 Paczyński curve	22
2.5 Single lens events	23
2.6 Multiple lenses	24
2.7 Higher-order effects	26
2.8 Modelling	28
3 Exoplanetary microlensing	31
II Rosetta bulge microlensing campaign	35
4 Rosetta spacecraft and mission	39
5 Photometric analysis	41
5.1 Observations	41
5.2 Analysis	43
5.3 Limitations of the photometric analysis	48
6 Microlens parallax	51

7	Results	57
7.1	Rosetta microlensing events	57
7.2	Paczynski fit	57
7.3	Microlens parallax measurement	60
7.4	Physical properties	61
8	Conclusion and future prospects	63
III Morphology of binary-lens light curves		65
9	Microlensing of the equal-mass binary lens	71
10	Classification scheme	77
10.1	The four peak types in microlensing	77
10.2	Notation for binary-lens caustic features	81
11	Methodology	87
11.1	Light curve simulation and processing	87
11.2	Iso-maxima regions	88
12	Results	93
12.1	Classes overview	96
12.2	Further considerations	102
13	Conclusion and future prospects	107
14	Appendix Morphology	109
14.1	$s = 0.65$	109
14.2	$s = 0.7$	112
14.3	$s = 0.85$	115
14.4	$s = 1.0$	118
14.5	$s = 1.5$	121
14.6	$s = 2.05$	124
14.7	$s = 2.5$	127
Bibliography		131

Part I

Introduction to gravitational microlensing towards the Galactic bulge

1 | Gravitational lensing

Gravitational lensing occurs when the light of a background source is deflected by an intervening massive body. This phenomenon can be observed on all astronomical scales. At the cosmological distance scale, quasars are gravitationally lensed by foreground galaxies, and early galaxies are lensed by galaxy clusters. In the Local Group, we can detect star-on-star lensing. In the phenomenon named “strong lensing” single or multiple images of the same source can be observed that will be more or less distorted from their original shape. A single point-mass lens acting on a single background source will create an Einstein ring (Figure 1.1), if source, lens and observer are perfectly aligned, but if that is not the case it always produces two (distorted) images of the background source, one outside and another one, mirror-inverted and flipped, inside the imaginary Einstein ring. As long as the angular distance between the source and the lens is substantially larger than the Einstein ring radius, the inner image will be vanishingly small and the outer image matches the unlensed source. But if the angular separation is of the order of the Einstein radius or smaller, then the inner image will increase in size and the centroid of the outer image is increasingly shifted away from the projected source position. In “microlensing” the images cannot be resolved in normal observations, simply because the angular scale is so much smaller in Galactic gravitational lensing with an Einstein ring size of the order of milliarcseconds rather than arcseconds (Figure 1.2)¹. Because of this, star-on-star lensing is next to impossible to discover in static systems². But transient events that occur whenever there is a relative transverse movement of source and lens can be detected

¹Microlensing *does* happen in the extragalactic setting as well, when the macro images of a quasar pass through a dense stellar field of the lensing galaxy and individual stars act as (secondary) lenses.

²As Einstein (1936) put it: “no great chance of observing this phenomenon”.

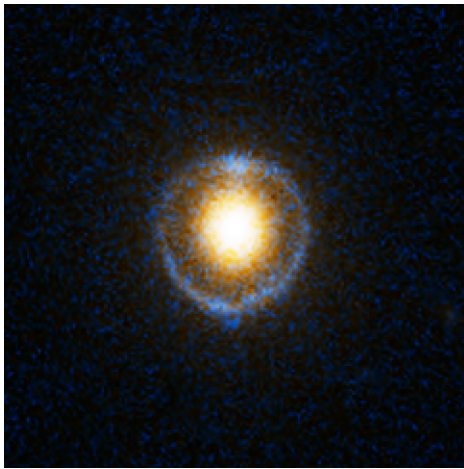


Figure 1.1: Hubble ACS B- and I-band image of gravitational lens SDSS J232120.93-093910.2. The light of a (blue) background galaxy is deflected by the (yellow) foreground galaxy to form the Einstein ring. The image is 8 arcseconds wide.

Credit: NASA, ESA, A. Bolton (Harvard-Smithsonian CfA) and the SLACS Team.

as a passing increase in brightness. A single point-mass lens is then detected through a symmetric rise and fall in flux; the light curve can be expressed in a strictly analytic form. The fundamental equations of gravitational lensing are discussed in Chapter 2. The lens system can be more complex: exoplanetary research (Chapter 3) is interested in cases that are composed of a host star with one or more planetary companions. Due to the unique way that multiple lenses manifest themselves in extended “caustic” structures (imaginary lines, where the background source star is formally infinitely magnified), the detection of extrasolar planets via microlensing does not depend on the brightness of their host star and is sensitive to planets in icy orbits (several AU) around distant (several kpc) host stars. With extrasolar planets having been detected in their hundreds since the first exciting discoveries in the 1990’s, exoplanetary microlensing might not be leading the numbers game, but is the method uniquely suited to fill in the parameter space of distant, cool and even solivagant planets (Gould et al., 2010; Gaudi, 2012; Cassan et al., 2012; Sumi et al., 2011). Only by combining all available methods, we will be able to gain a full picture of the planetary population of the Milky Way (Dominik et al., 2008).

While the principal mechanisms of microlensing are well understood, the method still poses unsolved challenges. Even for the single lens, one cannot directly obtain a full solution, as the physical parameters of the lensing system are all contained within a single observable, the event duration. In Part II, we can measure a second independent observable through microlens parallax effects between ground and space observations. For the

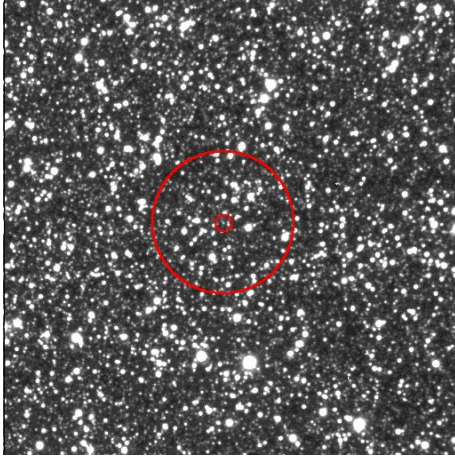


Figure 1.2: Microlensing target OGLE-2008-BLG-510, marked with two red concentric circles, in a typical bulge field. I-band image taken with the DFOSC instrument on the Danish 1.54m telescope at ESO La Silla, Chile. The image is 200 arcseconds wide.
Own observation for MiNDSTEp.

binary lens, the transient magnification cannot be expressed in a closed analytical form. The model optimisation has to work on a highly non-linear parameter space, while each individual model evaluation is time-costly because typically hundreds of data points from different telescopes have to be fitted. Modelling the physical characteristics of an observed lens system often runs into competing solutions; it is essential to increase our understanding of the parameter space and the topography of the optimisation surface, which is explored in Part III.

2 | Microlensing fundamentals

2.1 Lens equation

From Einstein's general theory of relativity (Einstein, 1916) it follows that light is deflected by massive bodies or, more precisely, that light always follows the null geodesics of spacetime, but spacetime is bent under the influence of gravitation. General relativity predicts that a light ray which passes a point mass M at a minimum distance ξ will be deflected by an angle

$$\tilde{\alpha} = \frac{4GM}{c^2\xi}, \quad (2.1)$$

where G denotes the Gravitational constant, c the speed of light. The deflection angle was first confirmed by Dyson, Eddington & Davidson (1920) during the solar eclipse in 1919, when they observed the apparent astrometric shifts of the positions of the bright stars of the Hyades cluster caused by the mass of the sun.

The point mass or point lens approximation is justified in a Galactic lensing situation, where slowly rotating and nearly spherical stars align to form a gravitational lens system, assuming that all light rays from the source star pass at a distance from the centre of the lensing body which is larger than the radius of that body. We can also make the thin-lens approximation: since the length of the optical system is much larger than the extent of the lensing body along the line of sight, it is safe to approximate the action of deflection as instantaneous and as taking place in an imaginary plane at the location of the lensing mass, the so called *lens plane*. The hyperbolic light paths can then be approximated as straight

lines with a sharp bend at the lens plane. We apply these considerations in Figure 2.1.

The gravitational lensing of a single source by a point mass will generally result in two images of the source. In Galactic stellar microlensing scenarios these arc-shaped images will be within a milliarcsecond or so of each other and generally photometrically detected as an apparent amplification of the background source light. Astrometric stellar microlensing, by means of measuring the light source centroid shift that is caused by the asymmetric geometry of the two images, has also been proposed. Promising impending events have been identified by Sahu et al. (2014)¹ and by Proft, Demleitner & Wambsganss (2011)², but the effect has not yet been observed in practice. In the Galactic context, we most commonly observe bulge stars “lensed” by other bulge or disk stars, which sometimes reveal themselves to be in binary systems and/or hosting planets. This kind of star-on-star lensing is – with today’s methods – only detected in transient events, where source and lens star have a non-zero relative proper motion μ_{LS} .

If one considers the geometry of Figure 2.1, one can directly infer the lens equation

$$\beta D_S = \theta D_S - \tilde{\alpha} D_{LS}. \quad (2.2)$$

The the small-angle approximation, $\tan x \approx x$, is applied here – justified by the fact that $\tilde{\alpha}, \beta, \theta \ll 1$ in (almost) all astronomical settings, with the notable exception of black-hole lensing where the deflection angle can be large, see Bozza (2010a).

Using the *scaled deflection angle* (i.e. scaled to the *observer plane*),

$$\alpha = \tilde{\alpha} \frac{D_{LS}}{D_S}, \quad (2.3)$$

the lens equation can be written as

$$\beta = \theta - \alpha. \quad (2.4)$$

¹Two Proxima Centauri events, measurable later this year with HST’s single-observation ~ 0.2 mas precision.

²Event predictions relying on *Gaia*’s single-observation ~ 100 μ as precision.

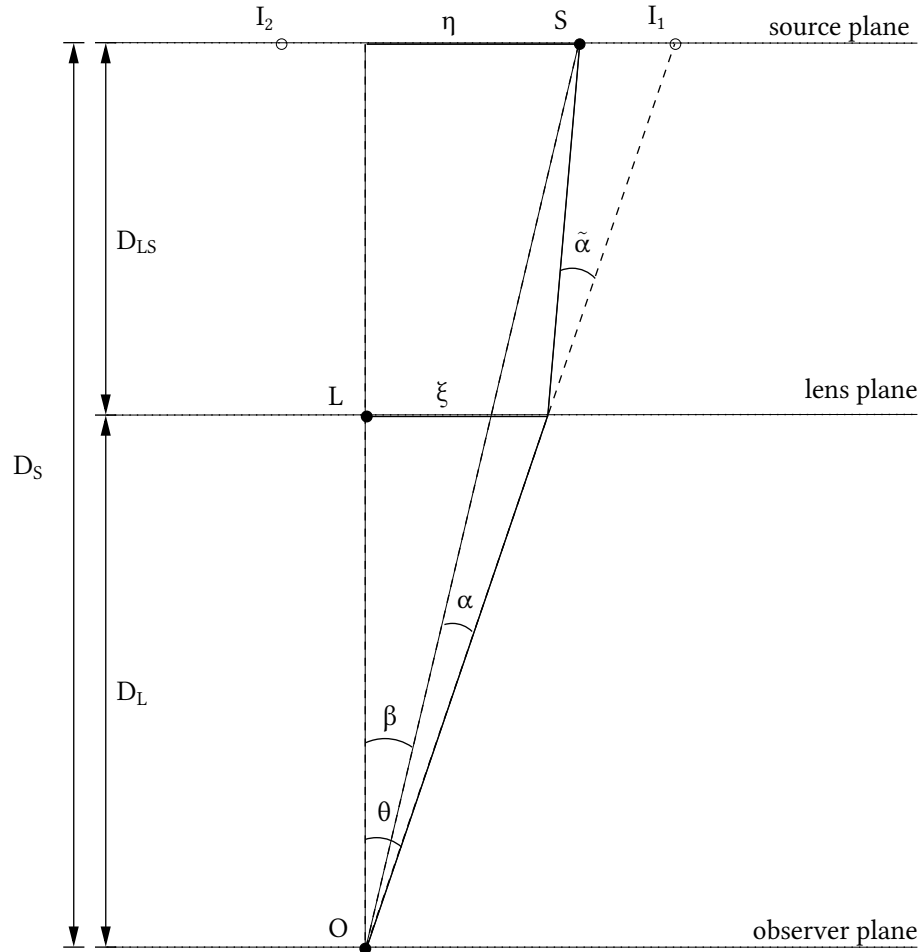


Figure 2.1: Sketch of a gravitational lensing system. The light of a background source S at a distance D_S is deflected by the angle $\tilde{\alpha}$ as it follows the null geodesic in the spacetime, curved by the lensing mass L at a distance D_L , before it reaches the observer O. The light path is shown in the thin-lens approximation, with a sharp bend at the lens plane, not in the true hyperbolic form. I_1 and I_2 denote the apparent locations of the two images of the source. For the observer's view compare Figure 2.2. Since $\tilde{\alpha}, \beta, \theta \ll 1$ in (almost) all astronomical settings, one can apply the small-angle approximation and directly read the *lens equation* off the diagram: $\beta D_S = \theta D_S - \tilde{\alpha} D_{LS}$.

It is a mapping $\mathbb{R}^2 \mapsto \mathbb{R}^2$, from the lens plane to the source plane. The apparent source position (i.e. the image position) θ maps to the true source position β . Knowing the image position θ , the lens equation can be solved for the source position β for any given mass distribution in the lens plane. Problematic is the inversion of the lens equation. Determining the image positions θ_i for a given source position β can, in general, not be done analytically.

2.2 Einstein ring

If observer, lens and source are perfectly aligned, the two images merge into one *Einstein ring* as the angular source position becomes $\beta = 0$.

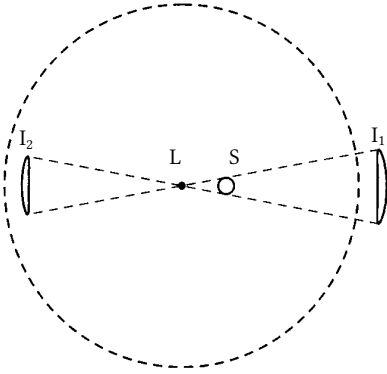


Figure 2.2: View of the lens plane from the observing point O. The source S is not directly visible and is only depicted here to mark the true source position in relation to the images I_i (see also Figure 2.1). The (theoretical) Einstein ring is indicated by the dashed circle. If the angular separation between L and S is decreased, the two images will further elongate into arcs and follow the Einstein ring more closely. If the source is directly behind the lens, the two images merge into one ring-shaped image. Figure reproduced from Paczyński (1996).

With the minimum distance $\xi = \theta D_L$, we can rewrite the lens equation 2.4,

$$\beta = 0 = \theta - \frac{4GM}{c^2\theta} \frac{D_{LS}}{D_L D_S} \quad (2.5)$$

and solve for the angular *Einstein radius*,

$$\theta_E = \sqrt{\frac{4GM}{c^2} \frac{D_{LS}}{D_L D_S}} = \sqrt{\frac{4GM}{c^2} \left(\frac{1}{D_L} - \frac{1}{D_S} \right)}, \quad (2.6)$$

where in the non-cosmological distance scale of our galaxy $D_{LS} = D_S - D_L$ holds true.

More than being just a singularity, the Einstein radius θ_E determines the angular scale of a gravitational lensing system. We can now rewrite the general lens equation (still

restricted to the point mass lens) in terms of the Einstein radius:

$$\beta = \theta - \frac{\theta_E^2}{\theta} \quad (2.7)$$

This equation has two solutions corresponding to the two images of the source (Figure 2.2),

$$\theta_{1,2} = \frac{1}{2} \left(\beta \pm \sqrt{\beta^2 + 4\theta_E^2} \right). \quad (2.8)$$

2.3 Lens magnification

The magnification A of an image is defined as the ratio between the solid angle of the magnified image and the solid angle of the original source,

$$A = \frac{\theta d\theta}{\beta d\beta}, \quad (2.9)$$

in other words, the ratio of the two-dimensional image and source areas as seen by an observer.

Since the surface brightness is conserved in the gravitational lensing process (because of Liouville's theorem, cf. Misner, Thorne & Wheeler (1973), p. 586), the increased image area equals an magnification in source brightness when integrating over the image. In *microlensing*, where the images are not resolvable by definition, one can only detect the total brightness magnification changing over time. Substituting β from Equation (2.7) and employing the useful dimensionless quantity u , defined as the angular separation of the source from the lens in units of the Einstein angle,

$$u = \frac{\beta}{\theta_E}, \quad (2.10)$$

two solutions for the two images arise:

$$A_{1,2} = \left(1 - \left(\frac{\theta_E}{\theta_{1,2}} \right)^4 \right)^{-1} = \frac{1}{2} \pm \frac{u^2 + 2}{2u\sqrt{u^2 + 4}}. \quad (2.11)$$

One image will always lie inside the Einstein ring. In Figure 2.1, this is I_2 , leading to a negative impact parameter and formally negative magnification, $\theta_2 < \theta_E \Rightarrow u_2 < 0 \Rightarrow A_2 < 0$. The image I_2 has negative parity with respect to the source, i.e. it appears mirrored and flipped. While the formal sum of the two magnifications thus is unity, $A_1 + A_2 = 1$, the total flux magnification of the source is obtained by summing over the two absolute values,

$$A = |A_1| + |A_2| = \frac{u^2 + 2}{u\sqrt{u^2 + 4}}. \quad (2.12)$$

If the source is located at an angular separation from the lens of exactly one Einstein angle, $\beta = \theta_E \Leftrightarrow u = 1$, the total magnification will become,

$$A(\beta = \theta_E) = \frac{3}{\sqrt{5}} \approx 1.34. \quad (2.13)$$

Translating this (dimensionless) magnification of the source flux into the apparent brightening compared to the unlensed source in magnitudes via $mag = -2.5 \log_{10} A$, this corresponds to an increase in brightness of $\Delta mag = -0.32$.

2.4 Paczyński curve

If the relative projected positions of a point-mass lens and a point source star change over time and under the assumption that they move uniformly and on rectilinear paths, the angular lens-source separation can be parameterised as a function of time,

$$u(t) = \sqrt{u_0^2 + \left(\frac{t - t_0}{t_E} \right)^2}, \quad (2.14)$$

where u_0 is the *impact parameter*, i.e. the separation angle at the time t_0 of closest approach. The Einstein time t_E is the time it takes the source to cross the Einstein radius ($t_E = \theta_E/\mu_{LS}$), providing a characteristic time scale for an individual transient event. Plugging $u(t)$ into Equation (2.12) gives the time dependent magnification,

$$A(t) = \frac{u(t)^2 + 2}{u(t)\sqrt{u(t)^2 + 4}}, \quad (2.15)$$

corresponding to the magnitude variation ($\propto \log A(t)$) in the plot on the right-hand side of Figure 2.3. This function is known as the *point-source, point-lens* (PSPL) light curve or the *Paczynski curve* as it was first shown in Paczyński (1986). In Equation (2.15) the magnitude variation is only dependent on the one parameter u , which itself is a function of t , t_0 and t_E .

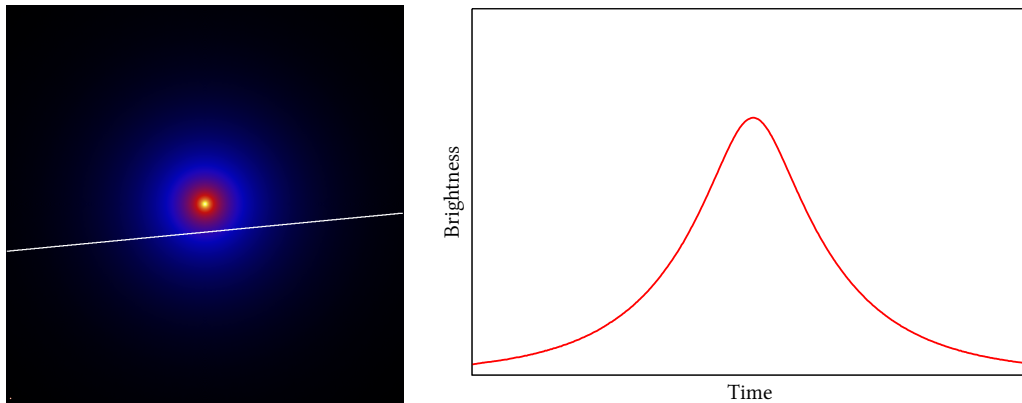


Figure 2.3: If a source star passes behind a lens star (centre) along the source trajectory depicted in the magnification map on the left, this gives rise to a point-source, point-lens light curve, also called *Paczynski curve*, following the analytic form of Equation (2.15).

2.5 Single lens events

Light curves such as the one in Figure 2.3 can be observed in star-on-star lensing and thousands of these “regular” microlensing events are observed each year by groups who

survey the Galactic bulge, such as OGLE³ and MOA⁴, although the probability for an individual event is only “one in a million” (Paczynski, 1986; Griest, 1991).

The single-lens light curve is observed as the magnified source star flux F_S , which can be blended with unmagnified flux F_{blend} from unresolved neighbouring sources (or light from the lens star itself),

$$F(t) = A(t)F_S + F_{\text{blend}} = (A(t) + g)F_S, \quad (2.16)$$

where we have $A(t)$ from Equation (2.15) and we introduce the blend factor $g = F_{\text{blend}}/F_S$.

The fluxes F_S and F_{blend} are specific to the observing instrument, because the filter bandpass and resolution obviously affect the collection of photons from the target and nearby targets. When data points from different telescopes are combined for the model search (as is common practice in Galactic microlensing), the number of free parameters is therefore increased by a pair of $[F_S^i, F_{\text{blend}}^i]$ per instrument and filter.

2.6 Multiple lenses

Much attention in current Galactic microlensing is paid to multiple-lens systems, which may or may not contain planetary lenses. For the projected positions, which are now two- rather than one-dimensional, one can use complex coordinates. Let η be the source position in the lens plane and ξ an image position. For N point-mass lenses the lens equation then becomes (Witt, 1990; Gaudi, Naber & Sackett, 1998)

$$\eta = \xi + \sum_{i=1}^N \frac{q_i}{\xi_i - \xi}, \quad (2.17)$$

where q_i is the mass ratio between lens i and the primary lens ($q_i = \frac{M_i}{M_0}$), which is conveniently placed at the origin ($\xi_0 = \mathbf{0}$). The magnification is now obtained as the inverse of

³Optical Gravitational Lensing Experiment (Udalski et al., 1992)

⁴Microlensing Observations in Astrophysics (Muraki et al., 1999)

the determinant of the Jacobian of the mapping equation (2.17),

$$A = \frac{1}{\det J(\xi)} \text{ with } \det J(\xi) = 1 - \frac{\partial \eta}{\partial \bar{\xi}} \frac{\partial \bar{\eta}}{\partial \xi}. \quad (2.18)$$

In the case $J(\xi) = 0$, a hypothetical point source would undergo infinite magnification (whereas a real, extended source will be highly, but finitely magnified). The mapping of all image positions satisfying $J = 0$ (called *critical curves*) to the source plane forms *caustics*, lines of formally infinite magnification that arise when the lens system is not circularly symmetric or when it is a continuous mass distribution⁵. Caustic lines offer a visualisation of the “optics” of a gravitational lens system.

In Figure 2.4, we see a magnification map with caustic structures and an extracted light curve, while Figure 2.5 shows the three topologies of binary lens caustics.

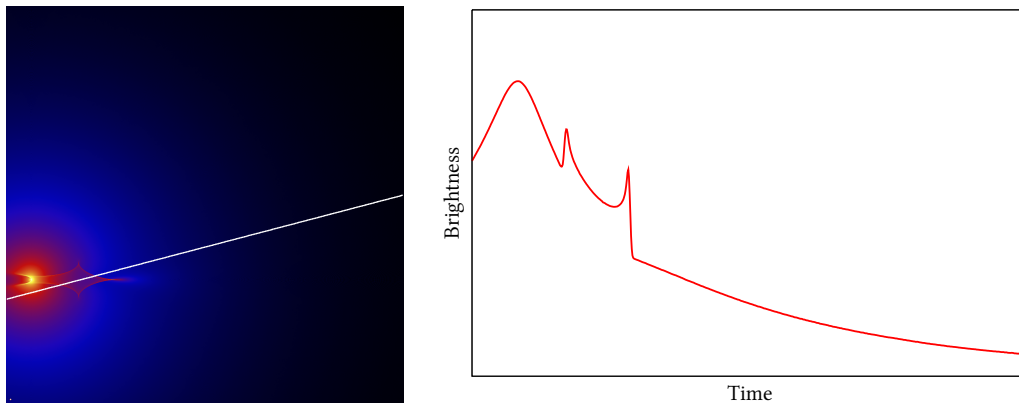


Figure 2.4: Caustics form when there an asymmetric lens mass distribution, for example, several point lenses. The magnification map, on the left, corresponds to a star-planet binary, with a mass ratio of 10^{-3} . If the source trajectory crosses the caustic lines, this often gives rise to a characteristic deviation from the Paczyński curve, a binary signature.

The multiple lens case is much more complex than the single lens case that we looked at before. The simple quadratic form of Equation (2.7) now gives way to a fifth-order polynomial with 3 solutions, or 5 if the source is inside the caustic lines, in the case of a binary lens (Schneider & Weiß, 1986), whereas for a triple lens the polynomial is already

⁵For a single point lens, the “caustic” is a single point at the position of the lens and the Einstein ring is the critical curve.

of 10th order with 4 up to 10 solutions, where an extra pair is created or destroyed at every caustic crossing (Rhie, 1997). The number of solutions corresponds to the number of images of the source. While this is theoretically true it can conjure up a misleading idea: when $\eta \rightarrow \infty$, there are still three images for a binary lens system, one coinciding with the unmagnified source star and the other two at the two lens positions ξ_i , but with zero magnification they cannot be seen as physical images. When the source moves closer to the lens system, the latter two images move away from the lens positions and have a non-zero photon flux.

2.7 Higher-order effects

2.7.1 Extended source effects

Generally speaking, an extended source will “blur” caustic lines and broaden and flatten peaks of high magnification. The simple model of a point source can be sufficient for single-lens cases as long as the minimum angular distance to the lens is at least of the order of several angular source radii ρ , but it breaks down when an extended source gets very close to the lens (Gould, 1994a; Witt & Mao, 1994). If the lens is a binary, extended-source effects become significant whenever the source is close to a caustic line, which is observed in the majority of binary microlensing events (see, for example, Jaroszyński et al. (2010)). Night, Di Stefano & Schwamb (2008) however argues that this might eventually be traced back to a selection effect, as “smoothly-perturbed” binary light curves are much easier to miss in the data noise.

Events that reach a very high magnification can display chromatic limb-darkening effects (see, for example, Alcock et al., 1997; Zub et al., 2011).

2.7.2 Microlens parallax

Parallax effects can be detected, when event observations from more than one location are combined or when the assumption of uniform, rectilinear motion between source, lens

and observer breaks down. An example of the latter is the *Earth-orbital parallax*: the orbital movement of the Earth around the Solar system barycentre can cause a wave-like perturbation in long-timescale events with a period of one year with the non-uniform change in angular lens-source separation, $\dot{u}(t) \neq 0$. In medium time-scale events it can still be detected as a significant asymmetry, as in the first detected microlens parallax effect (Alcock et al., 1995). The same effect on the light curve can be caused by a source star that is orbiting a binary companion, although it can be assumed that the probability for it to match the annual period and orientation is low. This latter effect is sometimes called *xallarap*, to emphasise that it is a kind of “reverse parallax” effect (Poindexter et al., 2005).

The very steep gradient of caustic crossings sometimes allows to detect *terrestrial parallax* effects, when telescopes spread across the globe observe the exact peak of the caustic crossing at slightly different times due to the (minute) differences in perspective, in effect “time-shifting” the light curve. The first successful observations of this effect are described in Gould et al. (2009).

Of course, the effect persists on a larger scale: *Earth-spacecraft parallax* is the term commonly used, when two quasi-independent light curves of the same source-lens system are observed by telescopes that are separated by a baseline of the order of AUs. In Part II of this work, we discuss observations of this effect and treat the theory of the microlens parallax in more detail (Chapter 6).

2.7.3 Orbital motion

In most Galactic binary microlensing events, with a typical timescale of $t_E \sim 1$ month, orbital motion can be ignored in the modelling, but the longer the duration of the event, the more likely are perturbations to the static model (Dominik, 1998). The orbital motion rotates and changes the shape of the binary caustic. This kind of caustic change was detected in the triple-lens, two-planet system OGLE-2006-BLG-109 and helped to constrain the orbit parameters (Gaudi et al., 2008).

2.7.4 Binary sources

Smoothly perturbed, i.e. non-caustic-crossing, binary lens light curves can be virtually indistinguishable from a microlensed *binary source*, where the Paczyński curve of the first source star is followed and superposed by that of its binary companion to give the impression of a smooth double-peaked cusp-grazing light curve as caused by a single source (Griest & Hu, 1992). Jaroszyński et al. (2010), for example, show competing binary-source and binary-lens models for many binary events from the 2006-2008 OGLE-III database. In principle, these can be distinguished by colour effects, which was originally proposed by Gaudi (1998) and first carried out by Hwang et al. (2013).

2.8 Modelling

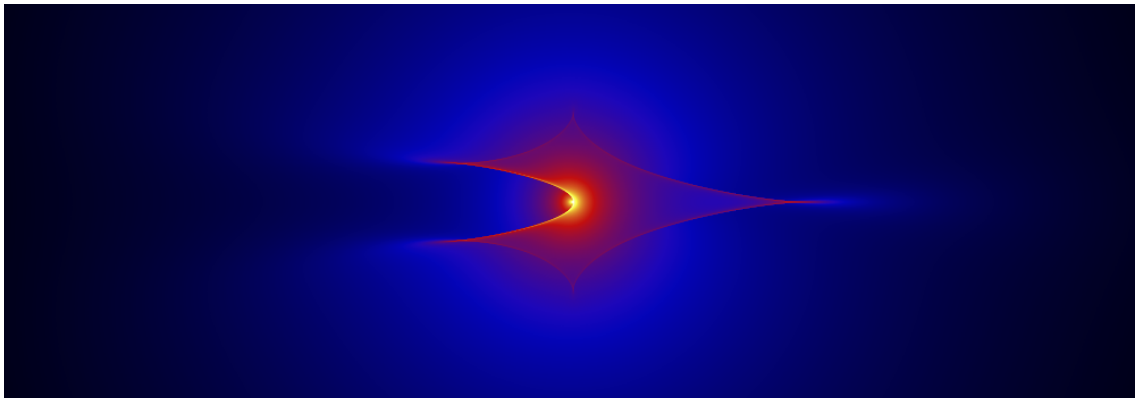
Different approaches have been tried out to deal with the fact that the microlensing magnification cannot be analytically calculated for multiple lens systems. One is the inverse ray-shooting method, where light rays are traced back from the observer to the source plane, summing up the deflection by individual masses in the lens plane. After deflection, all light rays are collected in pixels of the source plane. Since this is equivalent to tracing rays from the background source to the observer plane, the calculated magnification pattern then shows the magnification a pixel-sized source would experience at the respective pixel position in the source plane. A one-dimensional cut through a magnification map that has been convolved with a source profile represents a light curve model. The source model can have an arbitrary shape; here we use a flat-disc model, parametrised by a radius ρ .

This method was first deployed for microlensing purposes by Schneider & Weiß (1986) and Kayser, Refsdal & Stabell (1986), and later refined by Wambsganss (1990, 1999) to accommodate for a large number of lenses. It was first applied to planetary microlensing in Wambsganss (1997) and various implementations exist (Bennett & Rhie, 1996; Rattenbury et al., 2002; Dong et al., 2006; Hundertmark, Hessman & Dreizler, 2008), the latest being a parallelisation running on graphic processing units by Thompson et al. (2010).

The other method is contouring along the source images (Schramm & Kayser, 1987), in effect applying Green's theorem to find the image magnification by integrating along its contours. This method has also been further developed (Dominik, 1995; Gould & Gaucherel, 1997; Dominik, 1998; Dong et al., 2006; Dominik, 2007; Bozza, 2010b). This is a method with potentially very fast computing, although this can break down in high-magnification events, when the image contour becomes comparable in size to the image itself. Also, taking limb-darkening into account requires the calculation of many (~ 10) annuli.



(a) Close binary case. Depicted here is an angular separation of $d = 0.70\theta_E$.



(b) Intermediate binary case. $d = 1.00\theta_E$.



(c) Wide binary case. $d = 1.30\theta_E$.

Figure 2.5: Magnifications maps for three different angular separations of the two lenses. The long side has a length of one Einstein radius. The mass ratio is the same for all three illustrations, $q = 3 \times 10^{-3}$, and corresponds to a Jupiter-Sun mass ratio. The main lens is at the point of highest magnification in all three maps, while the secondary lens is always positioned to the *right* of the main lens at the indicated separation. The topology of the caustics changes and can be categorised into *close*, *intermediate* and *wide*.

3 | Exoplanetary microlensing

After centuries of speculation about the existence of worlds apart from our own and many failed attempts to secure evidence for them (Marcy & Butler, 2000), the recent decades have finally brought robust detections of extrasolar planets of which hundreds and thousands¹ have been confirmed to date. There are many excellent introductions to the fast-evolving field of exoplanetary research; Perryman (2011) covers the techniques as well as the breakthrough discoveries, from the first planetary system discovered around a pulsar (Wolszczan & Frail, 1992), the first planet around a main-sequence star, detected via radial-velocity measurements, (Mayor & Queloz, 1995) and the first transit detection of an extrasolar planet (Henry et al., 2000; Charbonneau et al., 2000), up to a preview of the state-of-the-art space programmes, the transit monitoring Kepler/NASA² which helped to almost double the then-known number of exoplanets over its (original mission) lifetime 2009–2013 and Gaia/ESO³, launched December 2013, which is designed for astrometry, but should have considerable impact on extrasolar planet research not only with its astrometric planet detections but also with time-series searches such as microlensing.

Exoplanetary microlensing was first put forth when Liebes (1964) mentioned that extrasolar planets around lensing host stars would perturb the microlensing event light curve of the stellar lens, but the idea could not be put into practice at the time.

Paczynski (1986) pointed out the possibility of gravitational lensing due to masses as small as $10^{-11} M_{\odot}$ in the halo of the Milky Way with background source stars in the nearby

¹exoplanet.eu

²nasa.gov/kepler

³sci.esa.int/gaia

galaxies⁴; this minimum mass estimate is limited by the requirement of having an angular source size which is smaller than the Einstein ring to achieve a significant magnification (assuming solar-size source stars in the paper). If found, those masses would provide an explanation of the dark matter in the halo. The idea was eventually picked up and several searches for microlensing events were called into life in the early 1990s. Alcock et al. (1993) and Aubourg et al. (1993) reported discoveries towards the Large Magellanic Cloud. Udalski et al. (1993) found events towards the Galactic bulge. As a general study of lensing behaviour Schneider & Weiß (1986) had investigated the case of binary point mass lenses. Paczyński (1991) provided details of lensing by Galactic bulge stars. On this foundation, Mao & Paczyński (1991) proposed to look for lensing signatures of binary stars and also extrasolar planets.

The search for massive compact halo object as potential dark matter, was not very fruitful (see, e.g., Afonso et al., 2003). Microlensing experiments carried out towards the Galactic bulge had originally been intended as test experiments for the halo surveys, but Mao & Paczyński (1991) estimated that roughly 10% of the lensing events should show the signature of a binary companion. It was realised, that through constantly monitoring a very large number of stars one would surely detect binary systems and possibly planets. Gould & Loeb (1992) qualitatively estimated the fraction of light curves that would show signs of companions of Jupiter or Saturn mass. Bennett & Rhie (1996) found that Earth-mass planets are in principle detectable. Wambsganss (1997) provided a detailed study of possible planetary light curve perturbations with different mass-ratio and angular-separation settings, concluding with the identification of the so-called “lensing zone” between angular star-planet separations of 0.6 to 1.6 θ_E that favours detections, because the planetary anomalies will settle on the slope of the Paczyński curve – on top of the ongoing primary lens magnification.

Steady monitoring of the Galactic bulge was realised by different groups, since 1992. As of 2009, OGLE (The Optical Gravitational Lens Experiment, see Udalski et al. (1992)) and MOA (Microlensing Observations in Astronomy, see Muraki et al. (1999)) are active survey

⁴A similar suggestion was made even earlier in a PhD thesis by Petrou (1981).

collaborations that complement each other by operating wide-field telescopes in Chile and New Zealand, respectively. Every season these groups detect microlensing events in their hundreds. In 2004, they jointly discovered a planet of 1.5 Jupiter masses with an orbit of ~ 3 AU, which made history as the first microlensing detected planet (Bond et al., 2004).

Already in 1995, a cooperative follow-up strategy had been realised by the GMAN (Pratt et al., 1995) and PLANET networks (Albrow et al., 1998; Dominik et al., 2002). The idea behind it was, and still is, to find a compromise between the field-of-view, the sampling rate, the limiting magnitude and the resolution of the targets. The survey groups OGLE and MOA monitor and publish all (detected) microlensing events. To maximise the gain, the follow-up community only reacts to events that promise to be interesting – because it is evolving towards a very high magnification or because it already shows deviations from the Paczyński curve. Several groups are active in the field of follow-up observations,⁵ although the distinction between survey and follow-up is less clear cut than in the past, as the survey telescopes become increasingly fast and the follow-up networks include more telescopes, freeing more resources for monitoring observations. The common goal is to get dense time resolution on interesting light curve features to be able to constrain a planetary model (or a binary star model, or a source star atmosphere model etc.) for that light curve. Crucial to the success of these operations is the continuous exchange of live data during the observing season⁶ that enables fitting of preliminary models and thereby tentative predictions about the development of the light curve, to decide about the priority of observing the given event. This approach has led to further planet discoveries.

Dominik (2010, Table 1) lists 26 planets reported in the microlensing literature up until 31 December 2009, with stronger or weaker evidence for each individual case. Since then further planet discoveries have been published (Miyake et al., 2011; Muraki et al., 2011; Batista et al., 2011; Yee et al., 2012; Kains et al., 2013; Poleski et al., 2014), with some detections probing the “brown dwarf desert” (Bozza et al., 2012; Street et al., 2013) – a

⁵Currently, these follow-up groups are PLANET (planet.iap.fr), MicroFUN (www.astronomy.ohio-state.edu/~microfun), RoboNet-II/LCOGT (robonet.lcogt.net) and MiNDSTEp (www.mindstep-science.org).

⁶The Galactic microlensing season lasts roughly from April to September, the time of year when the Galactic bulge is well visible from the southern hemisphere, at least for part of the night.

term that Marcy & Butler (2000) coined to describe the paucity of binary companions with masses in the brown-dwarf range ($13\text{--}80 M_{\text{Jupiter}}$). Even the detection of extrasolar moons seems to be within reach (Bennett et al., 2014; Liebig & Wambsganss, 2010). Gaudi (2010) and Dominik (2010) provide a good summary of the field of exoplanetary microlensing.

Part II

Galactic bulge microlensing events as observed from the Rosetta spacecraft in 2008

For 20 years now, microlensing observations have provided us with a wealth of information about the stellar and planetary content of our Galaxy, which is inaccessible via other current methods. Ground-based observations have brought us far and the lensing theory is ever-better understood, but it is the nature of the simplest conceivable single-source, single-lens lensing event to still pose a challenge as the physical parameters of the lens are heavily convolved in the common observables.

Dual-site microlensing observations with a significant baseline (comparable to the projected Einstein radius) provide one more independent observable beyond the common observables of a transient single-source, single-lens event: the microlens parallax π_E .

Combining this with either a measurement of the Einstein radius θ_E or of the relative lens-source proper motion μ_{LS} , it is possible to obtain a mass and a distance measurement for an object at a distance of the order of kiloparsecs – without requiring prior assumptions about the type of the lensing body. Measurements like these are necessary for unbiased Galactic population estimates, which in turn are fundamental for planet abundance statistics.

Before this background, an enterprising idea was realised in 2008: to “borrow” one of the cameras of the Rosetta spacecraft (Chapter 4) to monitor the Galactic bulge in order to collect stereoscopic data on Earth-observed microlensing events.

Sahu et al. (2001) were the first to observe a microlensing light curve from space as part of an M22-monitoring HST campaign. Other space-based (follow-up) light curves of individual microlensing targets have been published by Dong et al. (2007) and Muraki et al. (2011), but our work represents the first (and, to our knowledge, only) space survey of the Galactic bulge microlensing fields and the only one with a substantial baseline of $\mathcal{O}(\text{AU})$. Recently, Gould and Yee have explored the microlens-parallax measuring potential of space telescopes closer to Earth in a string of publications (Gould & Yee, 2012; Gould, 2013; Gould & Horne, 2013; Yee, 2013; Gould & Yee, 2014).

The photometric analysis (Chapter 5) proved challenging, as we are dealing with crowded-field data taken with a close-imaging camera (rather than a space telescope). We interpret the detected microlensing light curves with a view to the microlens parallax,

the theoretical context of which is given in Chapter 6. The end result of the study, presented in Chapter 7, relies on ground light curves published by OGLE (Udalski, 2003) for the detection of microlens parallax effects between ground and space observations.

Clarification The work in Part II will be published as Liebig et al. (2014b) (in preparation). As is the nature of this kind of research, the work relies heavily on previous collaborative efforts. I joined the team in 2012 to analyse the Rosetta microlensing data, all prior planning and all observational work were done without any input from me. Throughout the analysis, I was advised by Colin Snodgrass in particular.

4 | Rosetta spacecraft and mission

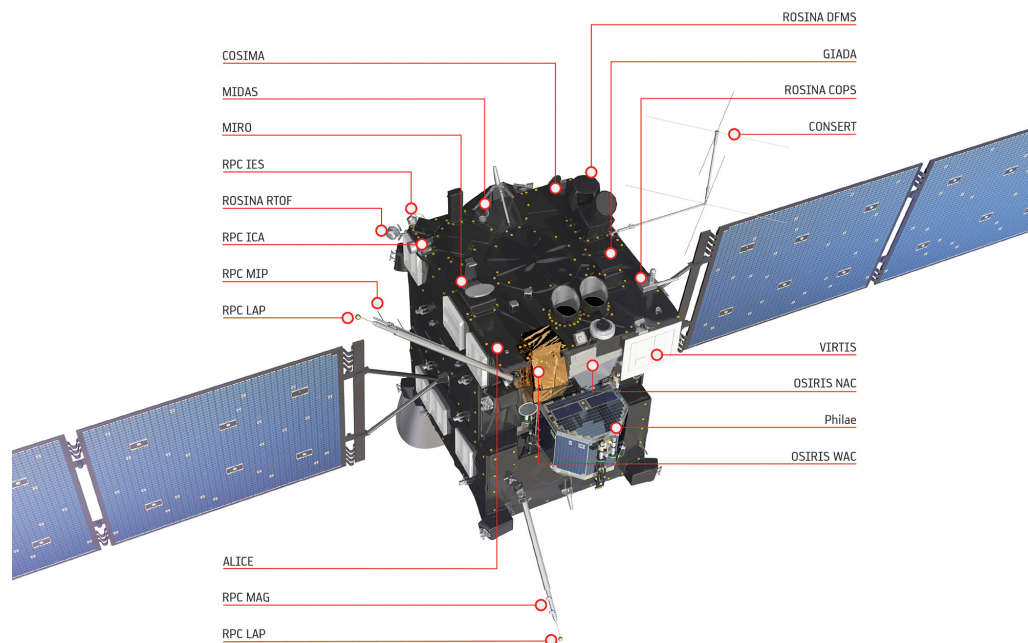


Figure 4.1: Rosetta and its instruments. This study works on data taken by the OSIRIS NAC, where OSIRIS stands for Optical, Spectroscopic, and Infrared Remote Imaging System Camera. OSIRIS is a dual camera imaging system consisting of a narrow-angle (NAC) and a wide-angle camera (WAC) and operating in the visible, near infrared and near ultraviolet wavelength range. Copyright: ESA/ATG medialab

“Rosetta” is one of the cornerstone missions of the European Space Agency. The spacecraft has been launched on 2 March 2004 on a mission to study the comet 67P/Churyumov-Gerasimenko. During its scheduled flight time of 10 years so far, it has completed four fly-by manoeuvres around Earth and Mars and has had two close encounters with asteroids 2867 Šteins and 21 Lutetia.

Rosetta spent the last 3 years in deep-space hibernation and successfully woke itself

up on 20 January 2014 to begin the last leg of its journey. The spacecraft is now being propelled towards 67P/CG, in May 2014 it will begin a braking manoeuvre to rendezvous with the comet at a relative speed of 2 m/s in August 2014 and, from then on, it will continuously monitor the comet on its voyage around the Sun. Rosetta has 11 on-board instruments, see Figure 4.1, among them OSIRIS (Optical, Spectroscopic, and Infrared Remote Imaging System) dual camera imaging system consisting of a narrow-angle (NAC, $(2^\circ)^2$) and a wide-angle camera (WAC, $(12^\circ)^2$) and operating in the visible, near infrared and near ultraviolet wavelength range.

Rosetta also carries the “Philae” lander unit with another 14 instruments, which will be deployed in November 2014 to land on the comet’s surface and examine the chemical and physical composition of the comet.

The Rosetta microlensing campaign was realised just after the 2867 Šteins flyby in September 2008 and made use of the OSIRIS Narrow-Angle Camera, originally designed to image asteroids from close range, as shown in Figure 4.2.

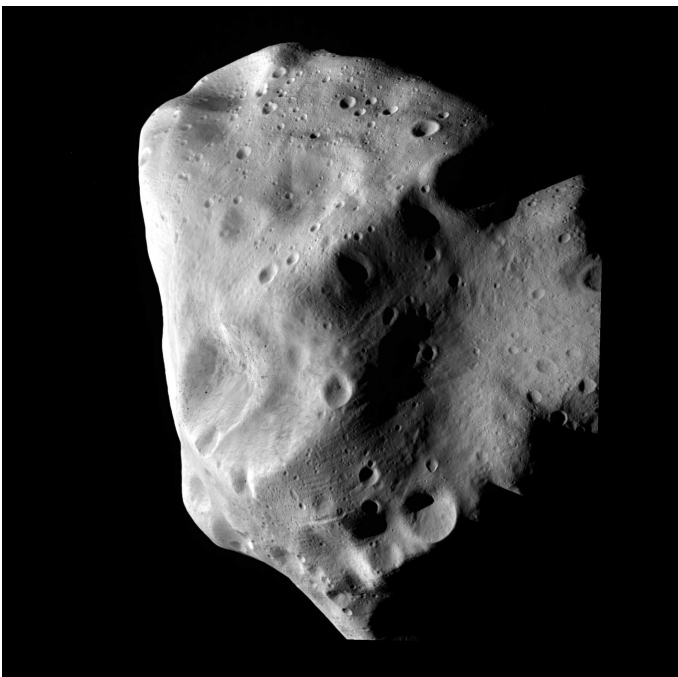


Figure 4.2: 21 Lutetia. The asteroid measures about 100 km across and orbits the sun with a semi-major axis of ~ 2.4 AU. The image was taken with the OSIRIS Narrow-Angle Camera at closest approach (~ 3200 km). The surface resolution in this image is approximately 60 meters per pixel.

Copyright: ESA 2010 MPS for OSIRIS Team MPS/-UPD/LAM/IAA/RSSD/-INTA/UPM/DASP/IDA

5 | Photometric analysis of the Rosetta microlensing data

5.1 Observations

The OSIRIS Narrow-Angle Camera (OSINAC from hereon) observed the Galactic bulge, in the region $[-5^\circ < b < -3^\circ, -5^\circ < l < 11^\circ]$ in Galactic coordinates, on seven epochs between 7 September and 4 October 2008. On each occasion, eight frames of $(2^\circ)^2$ were taken. The OSINAC was designed to image a comet from close range and is not a space telescope. The pixel scale is 3.9 arcseconds. The diameter of the camera entrance pupil is 89.4 mm. The “orange” filter was used, as this is the broadband filter with the greatest sensitivity on-board. For the central wavelength (649.4 nm) of the orange filter, the (purely theoretical) diffraction limit is 1.82 arcseconds. The uniform exposure time used was 300 seconds. For all technical specifications of the camera, see Keller et al. (2007a). The data were reduced using the OSIRIS standard pipeline, the procedure is detailed in e.g. Keller et al. (2007b).

After observations had been concluded, 20 events of interest were identified among the total of 655 candidate microlensing events announced by the OGLE Early-Warning System¹ (Udalski et al., 1994) in the 2008 microlensing season. The criteria applied were that the candidate event must lie within the OSINAC-covered field, must not last significantly longer than our observation span ($t_E < 60$ days) and should have peaked reasonably close to the observing window ($7 \text{ Sep} - t_E < t_0 < (5 \text{ Oct} + t_E)$).

For 12 events out of these 20, the team obtained complementary ground observations in

¹ogle.astrouw.edu.pl/ogle3/ews/2008/ews.html

June 2009 using the Wide Field Imager (WFI) instrument mounted on the MPG/ESO 2.2m-telescope, La Silla, Chile (Baade et al., 1999). The filters Rc/162-844 and MB-646/27-856² were chosen to match the OSINAC orange filter as closely as possible, the passbands are compared in Figure 5.1. Exposure times were 30 to 45 seconds. The WFI data were reduced

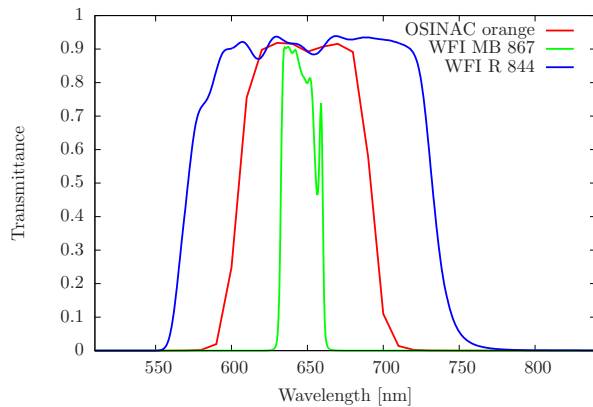


Figure 5.1: Passbands of the OSINAC orange filter and the two WFI filters used for follow-up observations. Only observations with the WFI R 844 filter were used in the analysis.

using a version of the Cambridge Astronomical Survey (CASU) pipeline (Irwin & Lewis, 2001) that has been adapted to work with the MPG/ESO WFI instrument. The following analysis is based on the Rc filter images as they were of an overall cleaner quality, while the MB data have only been used for sanity checks. Four of these 12 events had to be excluded from the final analysis, because, back at baseline, they were too faint to be identified on the WFI frames.

In the end, we have analysed the OSINAC data of eight event candidates, which are listed in Table 5.1.

²www.eso.org/lasilla/instruments/wfi/inst/filters/

Event name	RA(J2000.0)	Dec(J2000.0)
OGLE-2008-BLG-092	17:47:29.42	-34:43:35.6
OGLE-2008-BLG-374	17:54:56.33	-32:50:32.4
OGLE-2008-BLG-517	18:04:16.53	-28:50:22.2
OGLE-2008-BLG-571	18:01:18.75	-30:17:03.2
OGLE-2008-BLG-574	17:56:04.00	-32:05:01.0
OGLE-2008-BLG-582	18:10:24.03	-26:09:05.0
OGLE-2008-BLG-601	18:07:46.78	-26:20:15.0
OGLE-2008-BLG-605	18:07:41.50	-27:25:17.9

Table 5.1: Candidate events for the analysis.

5.2 Analysis

The OSINAC frame resolution is not sufficient for a direct identification of the microlensing targets. This problem is aggravated by the high source density of the observed fields, Figure 5.2 illustrates this problem.

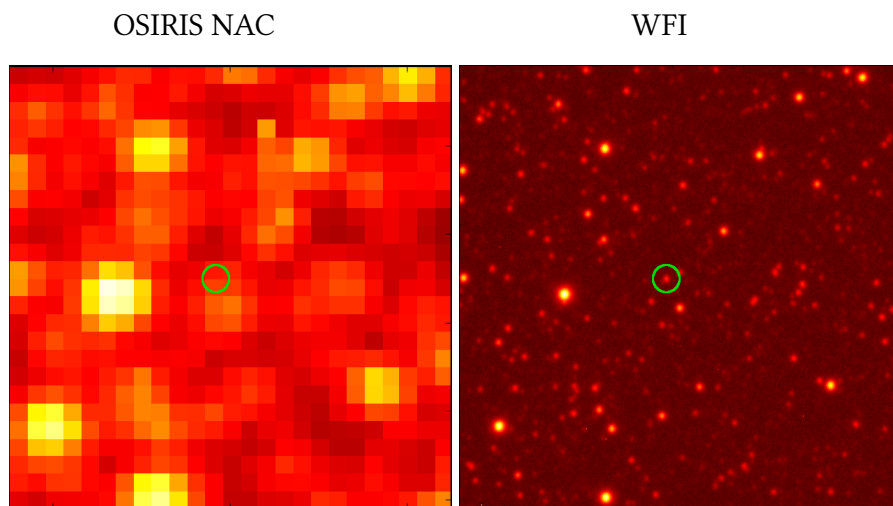


Figure 5.2: Juxtaposition of two observed frames, showing the same $(97.5 \text{ arcsec})^2$ field centred on the target OB08601, which is marked with the green circle. On the left, a OSIRIS Narrow-Angle Camera sub-frame as observed from the Rosetta spacecraft on 7 September 2008; on the right, a Wide-Field-Imager sub-frame, observed with the 2.2m telescope at ESO La Silla, Chile, on 18 June 2009.

Most current observations of Galactic microlensing events rely on a difference image

analysis for the photometric reduction (Alcock et al., 1999), which is well suited for the detection of difference flux in crowded fields. Originally, we expected to achieve good results with a direct image subtraction, because space-based observations are free from atmospheric perturbations. Unfortunately, image subtraction is not a viable option here, because the point-spread functions not only change considerably between epochs due to the spacecraft drift, but are severely undersampled at the same time. Additionally, there are simply not enough un-crowded stars on the OSINAC frames to calculate the convolution kernels.

The first challenge was calibrating the astrometry. The OSINAC FITS frames were fitted with initial World Coordinate System (WCS) information using the `astrometry.net` code (Lang et al., 2010) and index files based on the USNO-B1.0 catalogue (Monet et al., 2003), but, due to the aberrations of the optical system, deviations from the true positions of the order of 10 arcseconds occur on the wide-field frames. We cut down the original images to 0.125 degree fields, centred on the OGLE candidate events, and repeated the astrometric calibration. The post-calibration astrometric accuracy of the OSINAC subframes is comparable to the pixel size, i.e. 3.9 arcseconds.

Facing the adverse combination of a low resolution detector and a high stellar density, as well as a significant pollution with cosmic ray hits, we chose a compromise aperture size of $(3 \text{ px})^2$, where the aperture is placed so that the OGLE target coordinates for the microlensing event are contained in the central pixel.

The background will generally dominate over the source flux. To separate out the microlensed flux F from the total aperture flux F_{aper} , we have to subtract the blend flux F_{blend} . Since we observed from space, far beyond Earth's atmosphere, the sky background is negligible. By visual inspection, we identify and sort out data corrupted by cosmic ray hits. Afterwards, we consider all non-microlensed flux collected by the aperture as coming directly from the background stars near the target. These we hoped to identify from existing ground-based catalogues, but this idea proved to be unfeasible: While the OGLE photometric catalogue in V and I (Szymański et al., 2011) is cut off too early at the brighter end (complete for roughly $13.5 \lesssim I \lesssim 19 \text{ mag}$) and is not a good filter match

for the OSINAC orange filter, the APASS³ catalogue is not deep enough for our purposes (complete for roughly 10 mag to 17 mag in several filters, of which Sloan r' is the best match) and is even more shallow in crowded fields.

Therefore, it was decided to make use of higher-resolution ground observations of the microlensing events at baseline. In June 2009, when all chosen events of interest were safely back to baseline, the complementary observations of 12 events were obtained using WFI.

Using SExtractor (Bertin & Arnouts, 1996), we retrieve a catalogue of WFI sources for the field of interest around each target, i.e. a data set of sky position and (un-calibrated) flux $\{RA, Dec, F^{WFI}\}_{star}$ for each source on the frame. The equatorial coordinates RA and Dec are converted into the coordinate system of the OSINAC pixels, $\{X, Y, F^{WFI}\}_{star}$, to facilitate the creation of a synthetic OSINAC (baseline) frame. For creating the synthetic OSINAC frame, we need to photometrically and astrometrically match the WFI catalogue to the original OSINAC frame, which includes convolving the catalogue stars with the correct point spread function (PSF). The OSINAC PSF is best described by a Moffat (1969) function,

$$PSF(x, y; \alpha, \beta) = \frac{\beta - 1}{\pi\alpha^2} \left(1 + \left(\frac{x^2 + y^2}{\alpha^2} \right) \right)^{-\beta}. \quad (5.1)$$

The PSF is severely undersampled in the OSINAC frames with a FWHM of the order of 1 pixel. The flux density for a given source is described by

$$f^{WFI}(x, y) = F^{WFI} \times PSF(x, y; \alpha, \beta). \quad (5.2)$$

So we have five parameters to fit: linear shifts δx and δy , the Moffat PSF parameters α and β and, lastly, a WFI-to-OSINAC flux conversion factor $k = F/F^{WFI}$. The first four parameters must be adjusted for each frame, because the stellar PSFs change position and shape between epochs. The latter parameter, k , on the other hand, should be constant for a given filter choice (we checked that there was no sensitivity change in the OSINAC CCD

³www.aavso.org/apass

over the course of observations). While fitting it, we risk overcompensating for the target flux variabilities that we want to detect. The fit is also influenced by cosmic ray hits on the subframe, which are obvious in some cases, but can be imperceptible in others. For these reasons, we ran the optimisation below on a number of frames with *five* free parameters until we reached a good match for each frame and then fixed the flux conversion factor at the mean value, $k = 0.1875$, leaving only *four* free parameters for regular pipeline runs.

We then limit ourselves to a 25×25 pixel OSINAC sub-frame, where the PSF can be assumed stable and the optical aberrations are negligible, and use the SciPy (Jones et al., 2001–) `optimize.fmin` implementation of a downhill simplex algorithm to minimise

$$\sum_{\text{all pixels}} \left(\frac{F_{\text{pixel}}^{\text{SYN}} - F_{\text{pixel}}}{\sqrt{F_{\text{pixel}}}} \right)^2 \quad (5.3)$$

with the synthetic, WFI-based pixel flux

$$F_{\text{pixel}}^{\text{SYN}} = \sum_{\text{all stars}} \int_{\substack{\text{OSINAC} \\ \text{pixel area}}} f_{\text{star}}^{\text{WFI}} \times k, \quad (5.4)$$

where the stellar flux density is translated by δx , δy and the PSF shape modified by α and β :

$$f_{\text{star}}^{\text{WFI}}(x - X_{\text{star}} + \delta x, y - Y_{\text{star}} + \delta y; \alpha, \beta). \quad (5.5)$$

Parameters δx , δy , α , β , are optimised globally over the sub-frame, i.e. a sky area of $(97.5 \text{ arcsec})^2$, via Equation (5.3), where typically $0 < |\delta x| \sim |\delta y| < 0.5$ and $\alpha \sim 1.0$, $\beta \sim 1.5$. We can now work on the synthetic frame $F_{\text{pixel}}^{\text{SYN}}$ (Figure 5.3, centre) and we are interested in the synthetic baseline flux.

The *total* synthetic aperture flux is then the sum of the pixel flux of our chosen 9 pixels

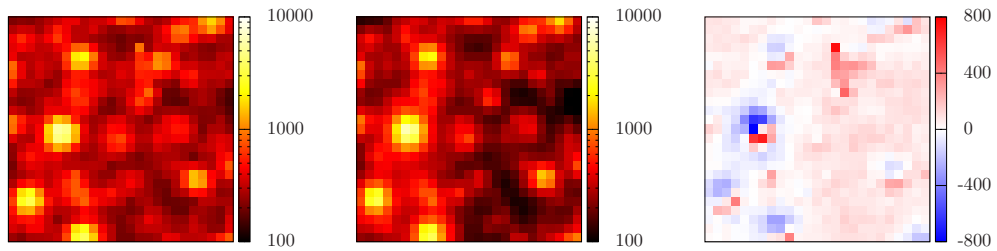


Figure 5.3: Comparison of the OSINAC frame (left) from Figure 5.2 with its synthetic reproduction from the WFI frame (centre). On the right is the difference image. A cosmic ray from the original image stands out in the top-right quarter and the brighter targets on the lower left of the frame can be traced by their stronger residuals.

in the aperture,

$$F_{\text{aper}}^{\text{SYN}} = \sum_{\text{pixel in aperture}} F_{\text{pixel}}^{\text{SYN}}(\alpha, \beta, \delta x, \delta y). \quad (5.6)$$

The *target* synthetic aperture flux, i.e. the synthetic baseline flux, is derived analogously to Equation (5.4) by identifying the target star in the WFI catalogue through astrometry (closest star to OGLE event coordinates) and visual inspection of the finding chart in doubtful cases:

$$F_{\text{target}}^{\text{SYN}} = \int_{\text{aperture}} f_{\text{target}}^{\text{WFI}}(\alpha, \beta, \delta x, \delta y) \times k. \quad (5.7)$$

Now, we infer the OSINAC blend flux from the WFI frame by modelling the aperture blend flux as

$$F_{\text{blend}}^{\text{SYN}} = F_{\text{aper}}^{\text{SYN}} - F_{\text{target}}^{\text{SYN}}. \quad (5.8)$$

The OSINAC data points, F , are then determined, after running the above analysis *for each frame individually*, as

$$F = F_{\text{aper}} - F_{\text{blend}}^{\text{SYN}}, \quad (5.9)$$

where F_{aper} is the raw OSINAC flux and $F_{\text{blend}}^{\text{SYN}}$ the synthetically constructed blend flux. F is the net target flux with any remaining time variability expected to be microlensing (but cf. limitations in Section 5.3). The reported uncertainties are the propagated Poisson errors of the raw OSINAC flux and the synthetic blend flux. The Rosetta microlensing light curves are discussed in Section 7.

For testing the reliability of the method, we have extracted light curves for a selection of comparison stars around target OB08601, Figure 5.4 shows the results.

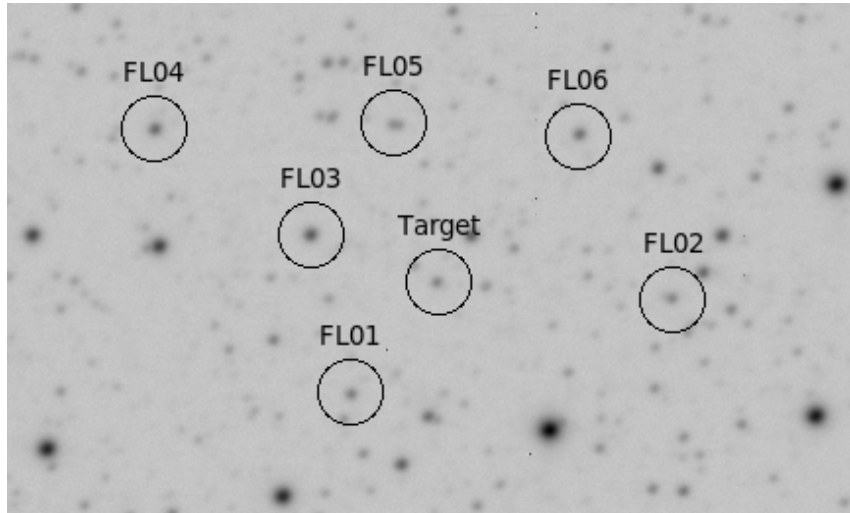
5.3 Limitations of the photometric analysis

There might still be additional blending due to either the limited resolution of the WFI frames or the limited deblending abilities of SExtractor. Typically, a bright lens star could be the source of such unresolved blend flux. We address this while fitting the Paczyński curve, see Section 7.2, by making use of the blend parameter as determined by the OGLE fit solution to the ground-observed microlensing light curve.

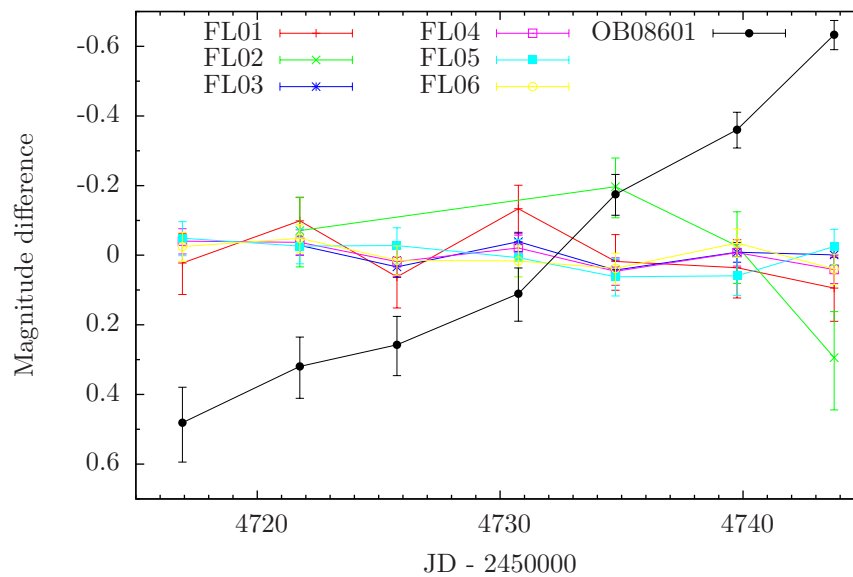
Our tool of choice, SExtractor, was not primarily designed for use on crowded stellar fields, but for the automatic classification of galaxies. We adapted the input parameters (circular apertures, low deblending threshold), optimising the stellar identification to a certain extent, but bear in mind that we use and value this tool for its ready usability and high throughput rather than expecting completely flawless star catalogue results. We have carefully checked the correct SExtractor identification of the target stars themselves and argue that for the blend flux determination it is fairly irrelevant whether two close neighbours are identified as one or two stars given the difference of scale for the WFI and OSINAC point spread functions.

Of course, ground observations are affected by changing seeing conditions and a high sky background, therefore the source identification can hardly be perfect and we miss out on stars fainter than the WFI magnitude limit⁴. Given the respective areas of the OSINAC and WFI detectors, $0.09^2/2.20^2 = 0.0017$, the flux of stars too faint to be identified on the

⁴About 21 R-mag ($S/N \geq 20$) in good conditions, for $t_{\text{exp}} = 60$ seconds, based on the ESO exposure time calculator: www.eso.org/observing/etc/



(a) Selected comparison stars around target OB08601, picked to match the baseline brightness of the target. FL05 is probably two unresolved sources.



(b) Corresponding light curves, displayed relative to their respective average magnitude. The data points are connected by lines to guide the eye. The uncertainties are modelled as Poisson noise. The variation in the target clearly stands out. FL02 had three obvious cosmic ray hits, those epochs have been eliminated from the light curve.

Figure 5.4: Test of the photometric method.

WFI frames by SExtractor should be completely negligible in the OSINAC frame.

6 | Microlens parallax

We recall from Section 2.5, Equation (2.16), that a microlensing light curve is observed as

$$F(t) = A(t)F_S + F_{\text{blend}} = (A(t) + g)F_S,$$

where $A(t)$ is the single-lens microlensing magnification, Equation (2.15).

The light curve $F(t)$ yields only one fit parameter, t_E , which contains all available information on the “optics” of the lensing set up, i.e. the mass M , the distance D_L , the source distance D_S and the relative proper motion μ_{LS} (Dominik, 2006):

$$t_E = \frac{1}{\mu_{LS}} \sqrt{\frac{4G}{c^2} M \left(\frac{1}{D_L} - \frac{1}{D_S} \right)}. \quad (6.1)$$

The Rosetta microlensing campaign enabled us to add one more independent observable to determine the physical properties of the lens system, the microlens parallax π_E .

Refsdal (1966) was the first to point out the potential of observing Galactic gravitational microlensing events from Earth and a distant spacecraft at (roughly) the same time. Due to parallactic viewing, the same background source star and foreground lens will, in general, result in two light curves with different impact parameters and different peak times for the two observatories (see Figure 6.1). If there is a relative motion between Earth and the spacecraft, this can additionally lead to a difference in t_E . These differences provide constraints on both the mass and the distance of the microlensing body, which can otherwise only be assessed through stellar models and statistical arguments.

The term “*microlens parallax*” only came into use some time later (see, for example,

Gould (2000) where it is defined it as $\pi_E := \frac{\text{AU}}{r_E}$, one Astronomical Unit over the physical lens-plane Einstein ring radius projected back from the source onto the observer plane). The quantity is intuitively understood as the relative parallax of lens and source star, $\pi_{LS} = \frac{\text{AU}}{D_L} - \frac{\text{AU}}{D_S}$, normalised to the Einstein angle θ_E :

$$\pi_E = \frac{\pi_{LS}}{\theta_E}. \quad (6.2)$$

$$(6.3)$$

As we will see, π_E can be expressed in terms of the observables Δt_0 and Δu_0 . This derivation is partly following Gould (1994b), with modernised notation.

We pick a coordinate system in the lens plane with right-handed basis vectors (\mathbf{e}_\parallel , \mathbf{e}_\perp) in units of (dimensionless) Einstein angles. The former, \mathbf{e}_\parallel , is parallel to the source-lens relative proper motion, $\boldsymbol{\mu}_{LS} = \boldsymbol{\mu}_L - \boldsymbol{\mu}_S$. The latter, \mathbf{e}_\perp , is parallel to the impact axis, $\mathbf{e}_\perp \parallel \mathbf{u}_0$, which in the case of uniform rectilinear relative motion is always orthogonal to the relative proper motion. We place the origin of the coordinate system at the lens position. We use this definition of the coordinate system independently of the observer position; see Figure 6.1 for an overview.

Now, we consider that the transient microlensing magnification in a given point-source, point-lens scenario depends only on the angular separation of source and lens $|\mathbf{u}(t)|$. With the chosen coordinate system, $\mathbf{u}(t)$ is identical to the source position as well as the angular lens-source separation in units of Einstein radii. At a time t , for an Earth-based observer, the source appears to be at position

$$\mathbf{u}^\oplus(t) = \frac{t - t_0^\oplus}{t_E} \times \mathbf{e}_\parallel + \mathbf{u}_0^\oplus \times \mathbf{e}_\perp, \quad (6.4)$$

while at the same time, an observer based on the Rosetta spacecraft would see

$$\mathbf{u}^R(t) = \frac{t - t_0^R}{t_E} \times \mathbf{e}_\parallel + \mathbf{u}_0^R \times \mathbf{e}_\perp. \quad (6.5)$$

This means we have an apparent source displacement of

$$\Delta \mathbf{u}(t) = \mathbf{u}^\oplus(t) - \mathbf{u}^R(t) \quad (6.6)$$

$$= -\frac{\Delta t_0}{t_E} \times \mathbf{e}_\parallel + \Delta \mathbf{u}_0 \times \mathbf{e}_\perp, \quad (6.7)$$

where the last line is no longer time-dependent, but assumes uniform rectilinear relative motion throughout; Equation 6.7 is also illustrated in Figure 6.1.

On the other hand, we can derive the source displacement from the known spacecraft position. We project the vector pointing from Earth to the spacecraft onto the observer plane as $\boldsymbol{\rho}$ and assume it to be static throughout the observations. When we scale it to the lens plane and normalise it to Einstein angles, we again have the difference in apparent source positions:

$$\Delta \mathbf{u} = \frac{D_S - D_L}{D_S} \boldsymbol{\rho} \frac{1}{D_L \theta_E} \quad (6.8)$$

$$= \frac{\pi_{LS}}{AU \theta_E} \boldsymbol{\rho} \quad (6.9)$$

$$= \frac{\pi_E}{AU} \boldsymbol{\rho}. \quad (6.10)$$

Thus we can rewrite the angular lens-source separation on the plane of sky as observed from Rosetta by adjusting Equation (6.4) to reflect the difference in perspective,

$$\mathbf{u}^R(t) = \mathbf{u}^\oplus(t) + \Delta \mathbf{u} \quad (6.11)$$

$$= \frac{t - t_0^\oplus}{t_E} \times \mathbf{e}_\parallel + \mathbf{u}_0^\oplus \times \mathbf{e}_\perp + \frac{\pi_E}{1AU} \boldsymbol{\rho}. \quad (6.12)$$

By equating the magnitudes of Equations (6.7) and (6.10), we can solve for π_E ,

$$\pi_E = \frac{AU}{|\boldsymbol{\rho}|} \sqrt{\left(\frac{\Delta t_0}{t_E}\right)^2 + \Delta u_0^2}. \quad (6.13)$$

The Einstein time t_E depends on the (comparatively) static quantities: lens mass, lens distance, source distance and transverse velocity of the source. If there is no significant

change of the relative positions of Earth and spacecraft during the course of observations, we can assume that $t_E^\oplus \sim t_E^R$ is equal for both ground and space observations.

The peak time difference $\Delta t_0 = |t_0^\oplus - t_0^R|$ would only be zero, if the projected source trajectory would coincidentally be orthogonal to the Earth-spacecraft axis. Similarly, $\Delta u_0 = u_0^\oplus - u_0^R$ will generally be unequal to zero, although by how much depends on the geometry of the gravitational lensing system. Δu_0 is degenerate in two ways:

- One degeneracy can be gleaned from Figure 6.1: $|\Delta u_0| = |u_0^\oplus| \mp |u_0^R|$ depends on whether the source trajectories are observed on the same side (*cis* \rightarrow $-$) or opposite sides (*trans* \rightarrow $+$) of the lens.
- Secondly, the sign of Δu_0 : we use a right-handed coordinate system ($\mathbf{e}_\parallel, \mathbf{e}_\perp$), as indicated in Figure 6.1, which means that an impact parameter is positive, when the source passes the lens in a clockwise sense.

This fourfold degeneracy carries over to the angle between the orientation of the source trajectory and the apparent source displacement $\tan \varphi = \Delta u_0 / \Delta t_0$. As Refsdal (1966) noted, it could be resolved with additional remote observers.

Having determined π_E , we directly have $\tilde{r}_E = AU/\pi_E$, the radius of the projected Einstein radius in the observer plane, which in turn yields the relative lens-source transverse velocity $\tilde{v} = \tilde{r}_E/t_E$, see Bouteux & Gould (1996) for typical \tilde{v} .

For the complete determination of the actual physical parameters of the lensing body, at least one more observable is needed. Either θ_E or μ_{LS} can fulfil this need. While θ_E is routinely measured for planetary or binary events, when the source passes over or near a caustic (as in the first successful mass measurement in microlensing (An et al., 2002)), it is close to impossible to determine in single-lens events – with the notable exception of high-magnification events that can display chromatic extended-source effects (cf. Section 2.7). There is however potential here for measuring the relative proper motion of source and lens μ_{LS} . High-resolution, multi-band follow-up observations could – in some cases – reveal the lens and distinguish it from the source star. As a rough guide, $D_L = 4$ kpc, $v_L = 200$ km/s equal a $\mu_{LS} \sim 10$ mas/year, but it can be substantially higher for

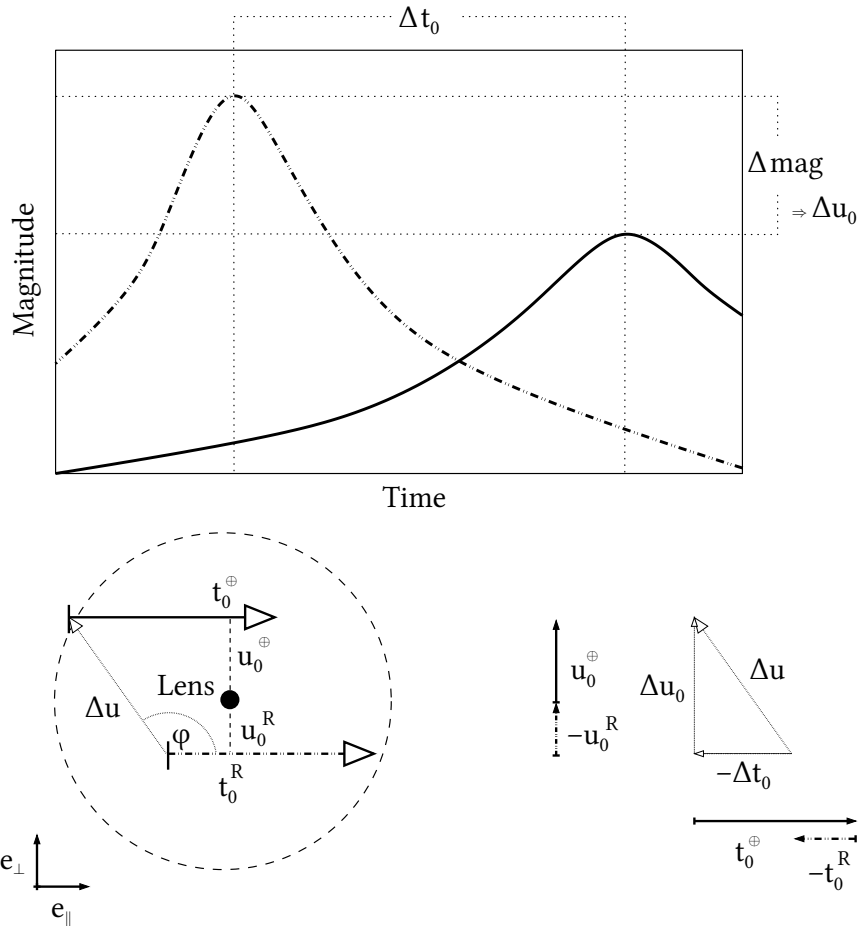


Figure 6.1: Sketch of the microlens parallax effect. *Top:* Two light curves of the same source, observed from two observatories, one on Earth, one on the Rosetta spacecraft. Assuming for illustrative purposes and without loss of generality that the two observations start and end simultaneously, with the source observed on the respective trajectories, the peak times t_0 will generally be unequal as will be the impact parameters u_0 .

Bottom left: Relative to a lens and its (theoretical) Einstein ring on the plane of sky, the sketch illustrates the source trajectory as observed from Earth ($\cdots\rightarrow$) and as observed from Rosetta (\longrightarrow). e_\perp and e_\parallel indicate our choice of coordinate system; the origin is always at the lens position. The source displacement vector $\Delta\mathbf{u}$ points from the spacecraft-observed source position to the Earth-observed source position at any given time. Its orientation is the orientation of the Earth-spacecraft separation projected onto the observer plane.

Bottom right: The vectorial relation of $\Delta\mathbf{u}$ with the measured u_0 and t_0 .

lens stars closer to us. Five years have passed since the Rosetta microlensing mission and any lens-displacement close to one arcsecond or more should be measurable from ground (with far higher potential in space observations, cf. Alcock et al. (2001)), if the lens is bright enough to be detectable. Given μ_{LS} , we know the lens mass,

$$M = \frac{\mu_{\text{LS}} t_{\text{E}}}{\pi_{\text{E}}} \frac{\text{AU} c^2}{4G}. \quad (6.14)$$

It is straightforward to get a reasonable estimate of the source star distance D_{S} after obtaining multi-band observations to determine the stellar type of the source. The lens distance D_{L} then follows from Equation (6.1).

7 | Results

7.1 Rosetta microlensing events

Out of the 8 candidates for which we have good-quality WFI baseline observations,

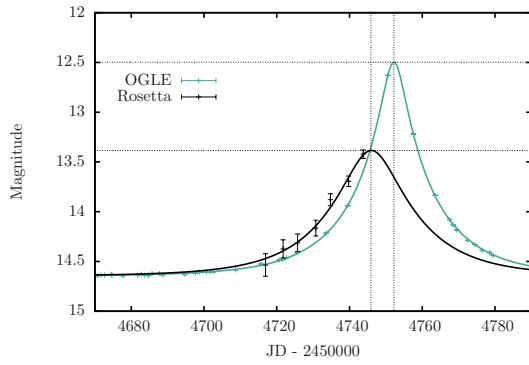
- two have flat OSINAC light curves within uncertainties,
- two show microlensing-like variability, see Figure 7.1(a) and 7.1(b), and
- four show variability that we cannot unambiguously diagnose, but we take the liberty to interpret two of them *as if* they were microlensing light curves, their light curves are shown in Figure 7.1(c) and 7.1(d).

It is unfortunate that the better-quality light curves do not cover the peak of the microlensing event, which would have significantly improved the constraints on t_0^R and u_0^R .

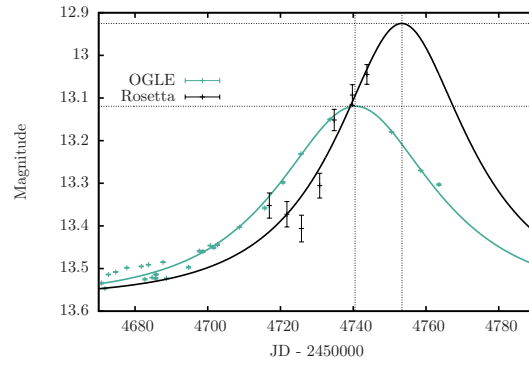
We propose acquiring more ground-based baseline observations to facilitate the analysis of another 8 candidates from the Rosetta microlensing campaign.

7.2 Paczyński fit

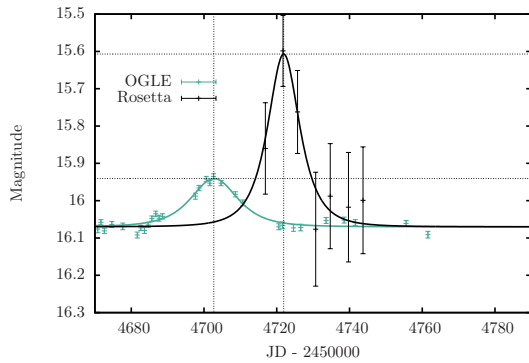
A regular Paczyński fit would determine five free parameters $\{t_0, t_E, u_o, F_S, g\}$, see Equation (2.16). Since we have only seven data points of poor photometric quality, this would mean a heavy over-parameterisation of the data, but we have additional information on the microlensing events that we can use to restrict the number of free parameters.



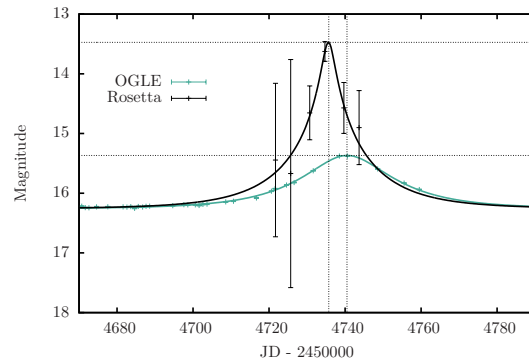
(a) OB08601. Our data points are very well described by a Paczyński curve, but unfortunately peak and baseline coverage are lacking.



(b) OB08582. With no peak or baseline data points and considerable scatter, the best-fit light curve can only be indicative.



(c) OB08571. The data hardly constrain the model, but taking the three above-baseline data points at face value, the Einstein time is an obvious match to the ground observations.



(d) OB08574. The data hardly constrain the model. The peak data point at epoch #5 could be a cosmic ray hit, but does not, in fact, change the result of a Paczyński fit to the remaining 6 data points.

Figure 7.1: Microlensing event plots comparing our OSINAC/Rosetta results (in black) with (provisional) OGLE data and model fits (in turquoise). The OSINAC light curves are magnitude-shifted to match the OGLE-reported I-magnitude baseline. For the determination of Δu_0 only the relative peak magnitudes are relevant. Δt_0 is the difference of peak epochs. The results are summarised in Tables 7.2 and 7.3.

Event	t_0 [JD]	u_0	I_0	t_E [days]	g^O
OB08571	2454702.792 ± 0.300	1.531 ± 0.018	16.070 ± 0.000	5.951 ± 0.281	0.0
OB08574	2454740.547 ± 0.072	0.476 ± 0.002	16.261 ± 0.000	21.279 ± 0.116	0.0
OB08582	2454740.607 ± 0.042	0.614 ± 0.014	14.12 ± 0.039	34.750 ± 0.462	0.658 ± 0.061
OB08601	2454752.219 ± 0.007	0.139 ± 0.000	14.65 ± 0.000	22.435 ± 0.024	0.0

Table 7.1: OGLE event parameters as published in the EWS on <http://ogle.astrouw.edu.pl/ogle3/ews/2008/ews.html>. Uncertainties of ‘0.000’ are an indicator of convergence problems in the PSPL fit, among the possible reasons for this are light curves that are asymmetric due to the Earth-orbital motion.

Event	χ^2	d.o.f.	t_0 [JD]	u_0	F_S (e^- in aperture)
OB08571	1.1	3	$2454721.9 \pm 5.9 \times 10^{31}$	0.80 ± 0.16	2213.2 ± 135.7
OB08574	0.82	3	$2454735.6 \pm 1.9 \times 10^{21}$	0.08 ± 0.04	140.9 ± 33.3
OB08582	17.28	3	2454753.3 ± 5.9	0.46 ± 0.04	4433.8 ± 208.9
OB08601	2.82	3	2454746.0 ± 1.8	0.32 ± 0.02	2312.7 ± 155.1

Table 7.2: Paczyński curve fit results from the Rosetta light curves (Section 7.2). t_E is not fitted, but taken from the OGLE results. The fits to events OB08571 and OB08574 cannot be constrained in t_0 .

The data points resulting from our analysis (Section 5.2) are mostly deblended, but as pointed out in Section 5.3, some stellar blend flux may still be present. Rather than working with the blanket assumption $g = 0$, we note that the OGLE data have a comparable resolution to our WFI frames and use $g = g^{\text{OGLE}}$ as a fixed parameter to account for unresolved blend flux. Table 7.1 shows preliminary OGLE results¹ of the Paczyński fit for the ground-observed microlensing light curves of the targets relevant to us. We still cannot accurately reproduce the true blending however, because the OGLE blend factor is based on a fit to an I-band light curve, whereas the potential WFI blend is in R-band and the relative brightnesses of blend star(s) and target can be different for the two bands.

We further assume that t_E is equal to the ground-obtained value t_E^{OGLE} , cf. discussion in Chapter 6.

This leaves us with three free fit parameters in Equation 2.16, $\{t_0, u_0, F_S\}$. We minimise χ^2 , with the OGLE u_0 and t_0 and an arbitrary $F_S = 100.0$ as the initial parameter set. The

¹As made available in the EWS on ogle.astrouw.edu.pl/ogle3/ews/2008/ews.html. We point out that the EWS photometry is preliminary and not a final result of the OGLE collaboration.

uncertainties are then estimated for each parameter p individually. We vary p manually and minimise χ^2 for each value of p by letting all other parameters vary freely. We continue doing this until we find a value for p that solves $\chi^2 - \chi_{\text{opt}}^2 = \text{d. o. f.}$ (with SciPy’s `optimize.newton`), meaning we have found the highest value of p on the hypersurface $\chi^2 = \chi_{\text{opt}}^2 + \text{d. o. f.}$. The uncertainty of p is then $\sigma_p = p - p_{\text{opt}}$.

Table 7.2 shows our fit results. With the given data, we cannot meaningfully fit any more complex models. The $\chi^2 < \text{d.o.f.}$ results in Table 7.2 show that even the three-parameter Paczyński fit is over-parametrised.

7.3 Microlens parallax measurement

We determine the microlens parallax value according to Equation (6.13) by combining the OGLE EWS results (Table 7.1) with our own Paczyński fit to the Rosetta-observed light curves (Table 7.2). For each event, there are the two degenerate results of the *cis* and *trans* case, equal to interpreting Δu_0 as either the difference or the sum of the impact parameters.

We use the OGLE results, because the OGLE collaboration provides public access to a consistent and (fairly) complete data set of the 2008 microlensing season. While most of our the events of interest have also been (ground-)observed by other survey or follow-up teams, the uncertainties in our microlens parallax determination are dominated, by orders of magnitudes, by the large photometric uncertainties of the OSINAC data. There would be no scientific gain in using additional ground-based data taken during the microlensing event. Our microlens parallax measurements are presented in Table 7.3.

To give feel for the numerical values, we can “exercise” through a typical case: assuming the source star at $D_S = 8 \text{ kpc}$ and the lens at $D_L = 4 \text{ kpc}$, we know the relative lens-source parallax to be $\pi_{LS} = 0.125 \text{ mas}$. Further assuming a lens mass of $M = 0.3 M_{\odot}$, the angular Einstein radius follows as $\theta_E \sim 0.55 \text{ mas}$ and $\pi_E = \pi_{LS}/\theta_E$ is then ~ 0.23 . Using $\rho = 1.6 \text{ AU}$, we have $\pi_E \rho/\text{AU} = \sqrt{(\Delta t_0/t_E)^2 + \Delta u_0^2} \sim 0.36$. Spinning this further, we can assume an equal contribution from the time difference and the impact parameter axis, and find that realistic values are, for example, $\Delta t_0/t_E \sim 7.68 \text{ days}/30 \text{ days}$ and $\Delta u_0 \sim 0.25$,

Event	<i>cis</i>			<i>trans</i>		
	π_E	\tilde{r}_E [AU]	\tilde{v} [km/s]	π_E	\tilde{r}_E [AU]	\tilde{v} [km/s]
OB08571	$1.5 \pm 1.1 \times 10^{32}$	$0.68 \pm \infty$	$198.3 \pm \infty$	$4.7 \pm 1.1 \times 10^{32}$	$0.21 \pm \infty$	$62.2 \pm \infty$
OB08574	$0.06 \pm 2.5 \times 10^{19}$	$17.33 \pm \infty$	$1410.4 \pm \infty$	$0.08 \pm 3.3 \times 10^{19}$	$12.51 \pm \infty$	$1018.3 \pm \infty$
OB08582	0.04 ± 0.05	28.4 ± 87.2	1415.9 ± 4346.2	0.25 ± 0.12	4.1 ± 4.0	202.2 ± 198.5
OB08601	0.03 ± 0.02	31.1 ± 68.8	2398.6 ± 5306.7	0.08 ± 0.03	12.4 ± 7.2	960.0 ± 555.8

Table 7.3: Microlens parallax results from the comparison of the Paczyński curves fitted to the Rosetta light curves with the OGLE parameters. Both *cis* and *trans* results are shown for each event. In addition to the microlens parallax π_E , we list the projected Einstein radius \tilde{r}_E and relative lens-source transverse velocity \tilde{v} .

which, we remember, can be the difference or the sum of u_0^R and u_0^\oplus .

7.4 Physical properties

Table 7.4 gives the physical parameters for each of the lenses that are *indicated* by the microlens parallax results, cf. Chapter 6. Due to the low data quality, these values are very little constrained for OB08601 and OB08582 and completely unconstrained for OB08571 and OB08574.

There is a rule of thumb for estimating the lens mass (Snodgrass, Horne & Tsapras (2004), Equation 16), which assumes that t_E scales with M (also see Tsapras et al. (2003); Dominik (2006)),

$$M = 0.3M_\odot \left(\frac{t_E}{35 \text{ days}} \right)^2. \quad (7.1)$$

We use it to infer “statistical” or “ t_E -based” masses for our set of microlensing events.

For each event, we present the *cis* and *trans* result, marked c or t. Without observing either μ_{LS} or θ_E , we do not have the means of distinguishing between the degenerate *cis* and *trans* configuration. However, a probabilistic argument can be made: If $|u_0^R|$ and $|u_0^\oplus|$ are comparable in value and, say, larger than 0.1, meaning neither observatory “sees” a high-magnification event, the *cis* configuration is more likely than having the (projected) lens (path) cross directly over the centre of the Earth-spacecraft baseline ρ . As soon as a

Assumption:	$D_S = 8 \text{ kpc}$ $M = 0.3 M_\odot$		$D_S = 8 \text{ kpc}$ $D_L = D_S/2$	“ t_E - based” M_L	
	D_L [kpc]	μ_{LS} [mas/year]	$M [M_\odot]$		
OB08571	c	0.2	220.0	0.007	0.009
	t	0.02	701.9	0.0007	
OB08574	c	7.5	2.4	4.6	0.11
	t	7.1	3.4	2.4	
OB08582	c	7.8 ± 0.9	0.9 ± 1.3	12.4 ± 40.7	0.30
	t	3.7 ± 2.5	6.3 ± 3.1	0.25 ± 0.74	
OB08601	c	7.8 ± 0.3	1.3 ± 0.9	14.3 ± 138.1	0.12
	t	7.1 ± 0.63	3.2 ± 1.2	2.3 ± 3.5	

Table 7.4: Physical properties of the lens system as they can be tentatively derived under the stated assumptions from the OSINAC light curves, in comparison to Earth-observed light curves. The values are purely indicative and the uncertainties, when not shown are *very large or ∞ !*

high-magnification event is observed from either observatory, there is absolutely no way of telling *cis* and *trans* results apart – although this can actually be used to advantage as comparing a high-magnification, low- u_0 light curve with a (remote-observed) high- u_0 curve means that the relative difference between the *cis* and *trans* parallax results will be small (Gould & Yee, 2013).

As Equations (6.14) and (6.1) or Table 7.4 show, the *trans* case (i.e. the larger of the two choices of $|\Delta u_0|$) induces a smaller lens mass and distance and higher relative proper motion compared to *cis*. Interestingly, the “ t_E -based” mass estimates in Table 7.4 “support” the *trans* case except for OB08571, where the *cis* mass is closer

8 | Conclusion and future prospects

We present results of the first space-based survey of Galactic bulge microlensing events, conducted by the OSIRIS/Rosetta team in 2008 at a low cost for the Galactic microlensing community. The position of the Rosetta spacecraft relative to Earth enabled us to detect and quantify significant parallactic offset of the detected microlensing events with respect to the corresponding Earth-observed light curves.

Because we used an imaging camera, rather than a space telescope, we are dealing with a large, undersampled point-spread function in the crowded bulge fields. We partly compensate for this by making use of higher-resolution, ground-observed frames to compute the very significant blend flux in our data. Still, the achievable photometric quality as well as the temporal resolution of our light curves is limited. So much so that not all detected variabilities can be unambiguously diagnosed. Naturally, this leads to large uncertainties in our subsequent determination of the microlens parallaxes and the indicated physical properties of the lenses.

Nonetheless, we were able to constrain the lens-mass, proper-motion relation for two microlenses. We propose follow-up observations of these targets to measure the lens-source relative proper motion, which can be combined with this microlens parallax study to determine the lens masses and distances in absolute terms, independent of any Galactic or stellar model. We have also proposed additional higher-resolution ground-based observations to enable us to analyse the remaining 8 candidate events. This proposal has already been included in the ongoing MiNDSTeP campaign at the Danish 1.54m telescope, La Silla, Chile, and we expect the complete data set in early summer 2014.

Part III

Morphological classes of binary microlensing light curves

This work is a study of the shapes of binary lens microlensing light curves, a morphology of light curves. The fundamental idea is to develop a classification scheme that can be directly applied to observed light curves and that allows for a narrowing of the modelling parameter space, while still guaranteeing completeness. We want to gain a good understanding of the range of possible light curves and how the identified morphological classes relate to subspaces of the modelling parameter space and to the model optimisation surface¹. We start with a review of work by previous authors and give a motivation for our undertaking. To be able to go into some depth with this study, we focus on the equal-mass binary lens, whose properties we review in Chapter 9. Chapter 10 introduces our morphology classification scheme, which is based on the four fundamental peak types that occur in microlensing, and a new notation for caustic features, which we developed along the way and which we hope others might find useful as a general language for discussing source trajectories. In Chapter 11, we discuss the practicalities, such as the light curve simulation, the peak counting and the identification of iso-maxima regions with light curve morphologies. In Chapter 12, we summarise and discuss the current results of this study and in Chapter 13 its future potential, while the bulk of the content is shown in tabular and graphical form in the appendix Chapter 14.

Clarification The work in Part III is planned for publication as Liebig et al. (2014a) (in preparation). Most of the ideas presented here have been developed and refined in close discussion with my co-authors. While the original suggestion to take a closer look at “the zoo of binary-lens light curve morphologies” was my supervisor Martin Dominik’s, it was Valerio Bozza who pointed me into the direction of “peak-number plots”. Last but not least, Giuseppe D’Ago joined in and, in particular, helped to expand the classification across different lens separations.

Previous work. It is not uncommon for modellers to explore specific morphological traits of light curves to narrow down the parameter space to be searched as has been done

¹I.e. what we will call the “ χ^2 landscape”, where “ χ^2 ” is used as an undifferentiated place holder for any goodness-of-fit estimator.

by authors such as Dominik & Hirshfeld (1996); Di Stefano & Perna (1997); Albrow et al. (1999); Dominik (1999a); Han & Gaudi (2008), but literature that systematically covers the whole range of possible morphologies is more scarce.

Mao & Di Stefano (1995) discussed a new method for modelling binary microlensing events: the positions and amplitudes of binary light curve extrema are compared to those stored in a pre-compiled (unblended, point-source) light curve library to find promising candidate events, which in turn provide initial parameter sets for a more conventional fitting procedure. This approach works well for multi-peak events, where the source trajectory passes over or close to the binary caustics. In principle, the method can uncover all degenerate solutions to an observed curve, but it is unclear whether the finite number of library entries are correctly located to access all “valleys” of the χ^2 landscape (in the words of the authors: “some intuitive understanding of caustics and trajectories is still useful”).

Di Stefano & Perna (1997) developed the library approach further by describing any binary-lens light curve by the set of coefficients of Chebyshev basis polynomials. They note that the Chebyshev expansion will never exactly match the microlensing light curve, because there will be extra extrema and inflection points, but an arbitrarily precise agreement can be achieved (limited by computational power) by further expansion. In this way, a model search can be refined until the photometric precision of the data points is matched. They find model parameter solutions to *smooth* and *caustic-crossing* light curves by comparing the rough characteristics of the light curve (positions of extrema and inflection points and the magnification values at these points) with a pre-computed light curve library and then searching the nearby environment in the physical parameter space with an increased sampling density until they find a match (or multiple matches) that satisfies the desired precision. In principle, this method is quite good at finding degenerate solutions and higher-order or even non-microlensing parameters can easily be integrated, but again it remains unclear whether all relevant parameter-space regions have corresponding entries in the library. The optimistic assertion that the “morphological features change in a way that is gradual and consistent as the physical parameters are changed” (Di Stefano & Perna, 1997) is most likely true for smooth light curves, but for caustic-crossing

light curves, we know that very small changes in the source trajectory can have dramatic implications for the number of extrema and their relative positions.

Night, Di Stefano & Schwamb (2008) make a broad distinction between *smooth* light curves and *caustic-crossing* light curves, but the classification is not based on the light curve itself, but on the source trajectory and its closeness to the caustics, i.e. the known simulation parameters, not the observable data. They come to the conclusion that the ratio of smoothly-perturbed to caustic-crossing binary-lens light curves is rather low in survey detections, which can partly be explained by the fact that caustic-crossing peaks stand out unambiguously, whereas smooth perturbations often can have a range of competing explanations (such as binary sources, parallax effects, . . .).

Motivation. The modelling of observed multiple-lens microlensing light curves requires extensive computation of the magnification curves. Much effort has been invested into speeding up the modelling process, by improving the parametrisation (Albrow et al., 1999; An et al., 2002; Cassan, 2008; Bennett, 2010; Bennett et al., 2012; Penny, 2013), by employing neural networks to map light curve features to model light curves (Vermaak, 2007) and by using the aforementioned light-curve libraries (Mao & Di Stefano, 1995; Di Stefano & Perna, 1997). Of course this development happened alongside of substantial advances in the code implementation of existing algorithms.

This work is particularly motivated by Bozza et al. (2012), where a detailed morphological assessment is used for the modelling of OGLE-2008-BLG-510 and furthermore the groundwork is laid for a real-time binary event modelling code (further based on Bozza (2001) and Bozza (2010b)). The code relies on a reliable choice of starting conditions (“seeds”) from where a search for *local* χ^2 minima is carried out. The choice of seeds is based on the morphology of the binary caustics, with the assumption that binary-lens light curves sampled from a given region of the parameter space lie on a smooth slope of the χ^2 landscape *as long as the morphology of the light curves does not change*. The *morphology* is understood, in this case, as a given peak sequence of caustic crossings and grazings, with any newly created or destroyed peak leading to a change in morphology.

Essentially, this work is starting out on a path very similar to Mao & Di Stefano (1995) and Di Stefano & Perna (1997): we also focus on categorising the extrema of a given light curve. By studying peak-number plots, we can separate groupings of light curves in the binary-lens parameter space. We are not concerned with directly establishing light curve models, but we want to ensure that we classify all possible light curves. We then want to improve our understanding of the relations between the parameter space and the light curves as well as the relations between the parameter space and the χ^2 landscape. The variety of microlensing light curves can seem overwhelming, but the trained eye recognises familiar patterns and translates them back to the parameter space. In fact, the shape of a microlensing light curve does follow certain rules, not any arbitrary curve can be interpreted as a microlensing light curve. Specifically, the limited topologies of the binary lens magnification maps allow only for a limited range of light curve morphologies.

9 | Microlensing of the equal-mass binary lens

In the simplest possible description of transient binary-lens magnification, we need the three parameters describing a lowest-order point-lens light curve: u_0 , the closest angular impact of the source to the centre of mass; t_E , the Einstein radius crossing time, and t_0 , the time of closest approach of the source to the centre of mass of the lens system, which is typically used to fix the epoch of observations, but is irrelevant for the light curve shape. Beyond the single lens parameters, we need the binary mass ratio q , the angular separation of the binary components s (normalised to Einstein angles θ_E), the angular source star radius ρ , also in units of θ_E , and the angle α between the binary axis and the direction of source motion, see also Figure 9.1. We assume uniform, rectilinear relative proper motion between source and lens for the simulations and ignore higher-order effects. An observed light curve also depends on the source flux F_S and the blend flux F_B , but for the purposes of this study we limit ourselves to theoretical light curves that can be scaled to any arbitrary F_S and have no blend flux.

Our parametrisation is equivalent to the convention detailed in Skowron et al. (2011, Appendix A), except that we regard the source rather than the lens system as moving, resulting in a difference of $\alpha_0^{\text{here}} = \alpha_0^{\text{Skowron}} - \pi$. A change by π just means the source is travelling in the opposite direction on the same trajectory which does not affect the morphology of the light curve, in other words it is a time reversal of the light curve. More on the parameter space symmetries in Section 11.2.

Schneider & Weiß (1986) have shown that there are exactly three distinct caustic

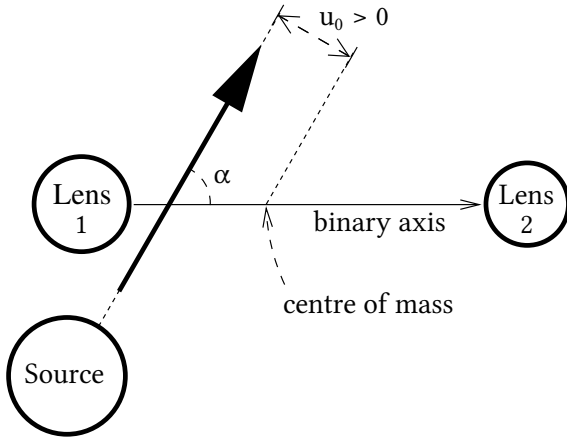


Figure 9.1: Our definition of u_0 and α . The impact parameter u_0 is positive, when source and lens (centre of mass) pass each other on the right-hand side as projected on the plane of sky. α is the angle between the binary axis (pointing from primary to secondary mass) and the source trajectory.

topologies for the case of an equal-mass binary lens. Erdl & Schneider (1993) confirmed this to be true for arbitrary mass ratios. They also noted the transition points in the binary lens separation where the caustic topology changes depending on the lens mass ratio q (also cf. Dominik (1999b)). A caustic enters the *close-separation* topology domain when $s < s_c$,

$$m_1 m_2 = \frac{1}{s_c^8} \left(\frac{1 - s_c^4}{3} \right)^3 \quad (9.1)$$

and will show the *wide-separation* topology when $s_w < s$,

$$s_w^2 = \left(\sqrt[3]{m_1} + \sqrt[3]{m_2} \right)^3, \quad (9.2)$$

where $m_1 = m_2/q$ is the primary mass of the binary lens system and m_2 the secondary mass. The five caustic examples in Figure 9.2 include the two transitioning cases. There is a clear evolution from one case to another, showing smooth beak-to-beak metamorphoses¹ (and exclusively those) with a changing angular separation s . For two co-planar point-mass lenses with no external shear (i.e. free from tidal perturbations) and no smooth background mass, the caustic lines are never nested or self-intersecting. In this study and the common Galactic lensing applications, caustic lines are always concave, although convex caustic lines are the norm for an extended lens mass (and point masses surrounded

¹As described in catastrophe theory, for further reading see Schneider, Ehlers & Falco (1992) and Petters, Levine & Wambsganss (2001).

by a smooth mass distribution, cf. Witt & Petters (1993)).

An isolated pair of lenses close to each other (i.e. $s < \sqrt{2}/2$ for $q = 1$) result in three caustics, see Figure 9.2(a): one diamond shaped at the centre of mass, and two small, triangular, secondary caustics set off from the binary axis. For extreme (planetary) mass ratios, the central caustic will assume an arrow shape, pointing towards the secondary mass and virtually indistinguishable from the central caustic of the wide case with a $s^{[1]} \leftrightarrow (s^{[1]})^{-1}$ ambiguity² (Dominik, 1999b), while the two secondary caustics will move further and further away from the small-mass companion and diminish in relative strength.

If the angular separation of the two lenses is of the order of one Einstein radius, there will be only one central, relatively large, six-cusped caustic, see Figure 9.2(c). For the equal-mass binary lens “of the order of” means the exact range $\sqrt{2}/2 < s < 2$, if the caustic lines are not “blurred” by an extended source.

If the two lenses are far from each other ($s > 2$), two diamond shaped caustics close to the true position of the lenses result. These will transform into arrow shapes pointing towards the common centre of mass, if the lenses are closer to each other as in Figure 9.2(e). If the secondary is less massive, instead of an arrow head, its caustic will retain an extended diamond shape, and its position will move closer to the primary lens ($\sim s - 1/s$ from the primary). Under these circumstances this caustic is called the secondary or planetary caustic.

As an aside, introducing a third lens can lead to exceedingly more complicated caustic structures. Daněk & Heyrovský (2011) have set out to explore the full range of triple-lens caustic topologies. Just one very specific example, the case of three masses positioned at the tips of an equilateral triangle with two equal masses at $(1 - \mu)/2$ and a third mass at μ , boasts 10 different caustic topologies. Many of those can be found in other triple-lens scenarios, but the list of ten is nowhere close to covering the whole range possible.

For a detailed discussion of the practical application of caustics, especially in view of very different lens masses, consult Gaudi (2010). The mathematical treatment of caustics, through singularity theory of differentiable maps, is detailed in Petters, Levine & Wambs-

²Where $s^{[1]}$ is the lens separation measured in units of the Einstein angle of the *primary mass*, not the total mass.

ganss (2001).

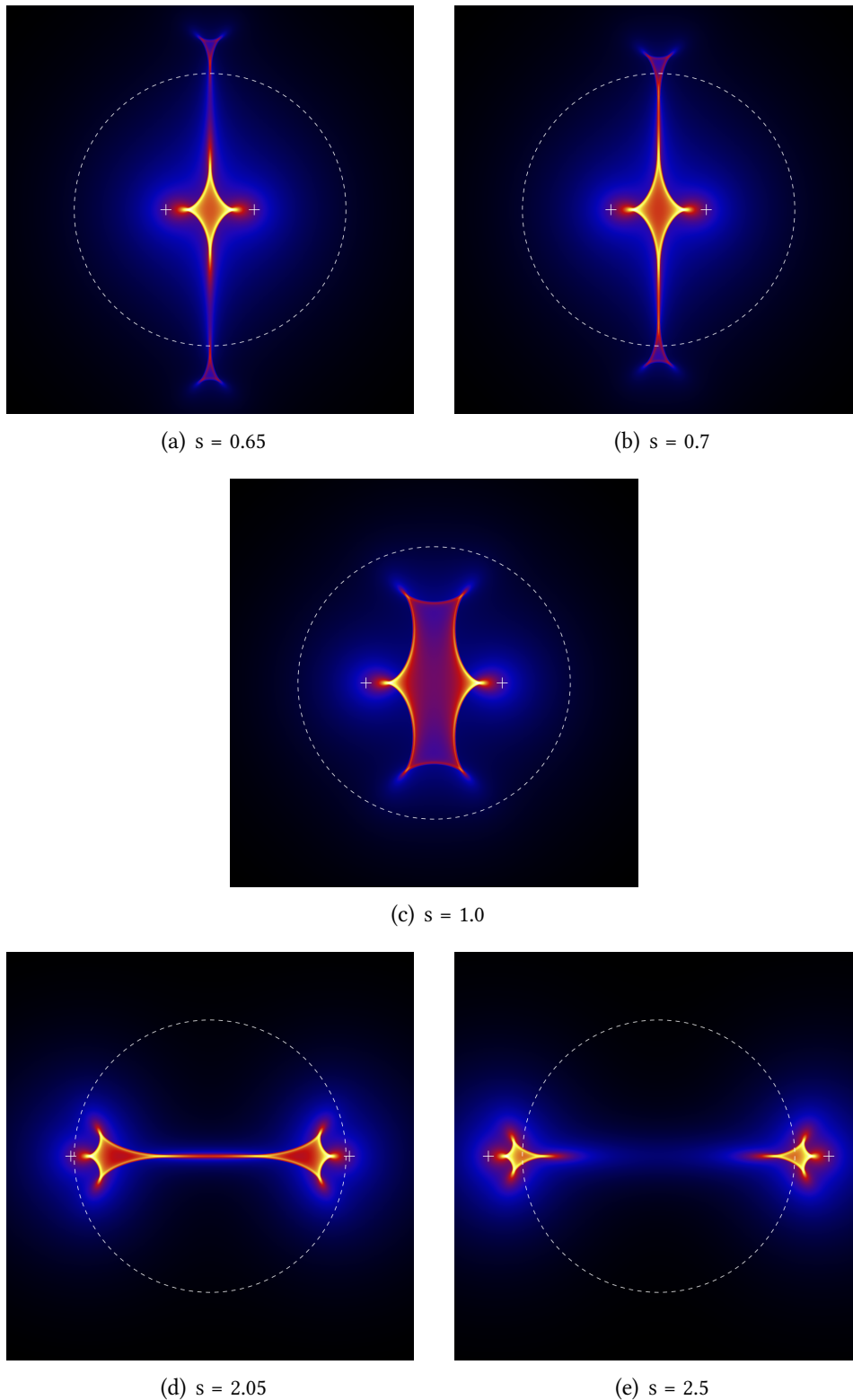


Figure 9.2: Magnification maps showing the three different caustic topologies *close*, *intermediate* and *wide* and the transition cases for an extended source ($\rho = 0.01$). The lens positions are marked with white plus signs, the Einstein radius with the white, dashed circle. All five maps have a side length of $3.0 \theta_E$

10 | Classification scheme

10.1 The four peak types in microlensing

We desire to find a classification of binary microlensing events that is based solely on observable features of light curves. We start out on the simple basis that any microlensing light curve can be described as a sequence of peaks. We propose that a class of light curves can be summarised by their common sequence of peak types. We recognise that any microlensing light-curve peak is created by one of four basic mechanisms. We discuss the four peak types in detail below, but in short summary they are:

1. a cusp grazing (\bar{C}),
2. a caustic fold entry (F-) or exit (-F),
3. a cusp entry (C-) or exit (-C), or
4. a fold grazing ($-\bar{F}$).

Now, in detail: 1. the *cusp grazing*, \bar{C} : The peak that arises when the source passes outside the caustic but over a cusp, or close enough to one of the cusps to pass over the lobe of increased magnification, is a “cusp grazing”. For a theoretical point source, a cusp is the point where two fold lines meet; an extended source blurs the fold lines and the location of the cusp point is less well defined. We unambiguously call a light curve “cusp-grazing”, if the source trajectory is outside the caustic pre and post-peak and only a single peak results. The Paczyński curve can be understood as a grazing of the point caustic (or “cusp”) of the single lens. The name *Paczyński curve* should be reserved for single lens light curves only, but in the limits where a binary lens resembles a single lens, when the source does not

pass close to the caustics or when the caustics are very small relative to the solid angle of the source, a single-peaked light curve will result. We do not register any morphological difference to the cusp grazing in the narrow sense – an existing difference that we disregard are discontinuities (or “kinks”) in the light curve, which occur, for example, when the extended source trajectory cuts perpendicular to the cusp direction and on the inside of the theoretical cusp position, cf. Figure 10.1.

The second and third type of peak occur in a caustic crossing: If a source passes over a caustic, which is extended compared to the angular source size, one peak will arise when the caustic is entered and another when the source exits again from the caustic.

2. the *fold entry/exit*, F-/-F: When the source enters on a caustic fold, this creates a very distinctly shaped curve (cf. Schneider, Ehlers & Falco (1992); Gaudi & Petters (2002)), with a steep, almost vertical rise followed by a more parabolic fall, which does not descend as low as the caustic-exterior magnification. The morphology is mirrored in the fold exit. A pair of fold entry and exit peaks give rise to the familiar *double caustic crossing* signature.

3. the *cusp entry/exit*, C-/-C: If the caustic is entered or exited along a cusp, the peak will have a more symmetric shape, because the lobe outside the caustic and the close proximity of the fold lines on the inside of the caustic attenuate the gradient of the passage on both sides. The fact that the magnification in the caustic interior is increased can help to distinguish it from a cusp-grazing¹.

4. the “interior fold approach” or *fold grazing*, \bar{F} -: This type of peak occurs inside the caustic, while the source trajectory passes close to a caustic fold. Due to the concavity of the caustic lines, the fold-grazing peak will only be observed if it is an *interior* approach. A special case is the peak that occurs when two or more caustic lines are close enough or strong enough to raise the magnification of an extended area between them, giving rise to a peak that cannot be directly attributed to one single fold.

These “building blocks” of microlensing light curves can be sequenced, subject to a few rules²:

¹Mao, Witt & An (2013) have recently shown that this is not necessarily the case for a multi-planar lens distribution.

²Considering here only fully covered events.

- a caustic entry must be followed by a caustic exit³
- a caustic exit cannot occur, if the caustic has not been entered before
- a fold grazing can only take place inside a caustic⁴
- a cusp grazing can only take place outside a caustic⁵

All microlensing light curves (in the parameter space considered in this study) adhere to these rules, but just conforming to these rules does not guarantee a microlensing light curve.

To see an example of a light curve classification “at work”, consider the light curve Figure 12.2 h, where we see a (symmetric) cusp entry (C-) paired with an (asymmetric) fold exit (-F) and a post-caustic grazing of the cusp lobe (\bar{C}),

$$\underbrace{C-F}_{\substack{\text{caustic} \\ \text{traversal}}} \underbrace{\bar{C}}_{\substack{\text{cusp} \\ \text{lobe}}}.$$

Figure 12.3 c gives a nice example with a clear-cut fold entry (F-), followed by a second peak still inside the caustic, which can only be an inner fold approach ($-\bar{F}$ -), a fold exit (-F) and followed by a final cusp lobe grazing (\bar{C}), so we classify it as

$$\underbrace{F-\bar{F}-F}_{\substack{\text{caustic} \\ \text{traversal}}} \underbrace{\bar{C}}_{\substack{\text{cusp} \\ \text{lobe}}}.$$

We realise that unambiguously establishing the nature of a given peak is often not possible without knowing the source trajectory, but it is generally straightforward to at least exclude one or more of the four mechanisms.

An extended source blurs the finer details of the caustic lines and “delays” the peak of a caustic entry. To avoid any confusion in nomenclature, we classify strictly on the basis of light curve features. As an example, Figure 10.1 shows three different cusp-grazing

³For $n > 3$ lenses the number of entries and exits may be unequal as caustic lines can be intersecting and nesting. For $n = 2$, one caustic entry must be followed by one caustic exit, before another caustic entry can occur.

⁴True for coplanar lenses.

⁵True for $n = 2$ lenses.

light curves in comparison with a fold-crossing one. We consider in this illustration a set of parallel source trajectories that are orthogonal to the pointing direction of the cusp. We unequivocally classify the peaks in the single-peaked light curves as \bar{C} , whereas the double-peaked light curve gives us a pair of fold crossings F-F. It follows that the peak

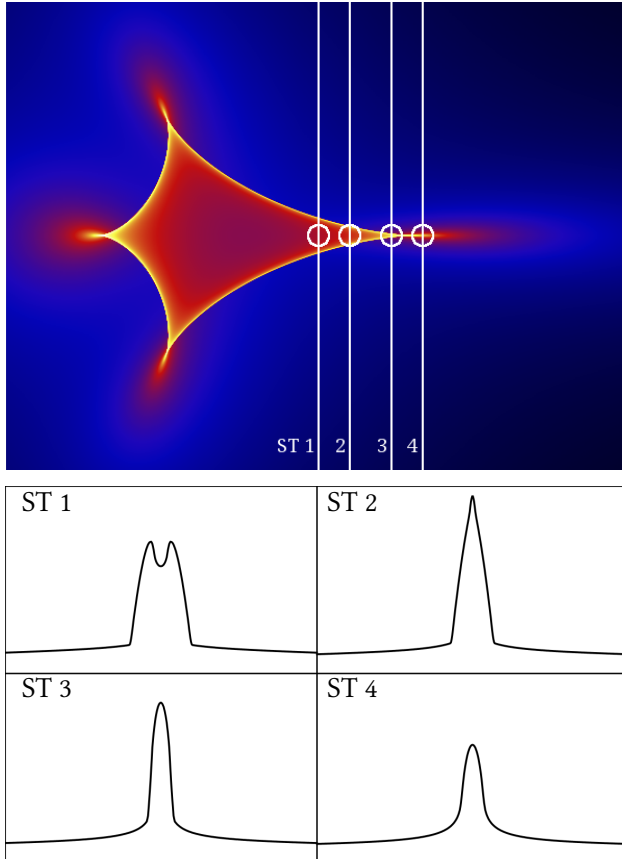


Figure 10.1: Comparison of *cusp-grazing* and *fold-crossing* source trajectories. The angular source size is indicated by the light circles. From left to right, the light curve morphology evolves from a double fold crossing (F-F) to a cusp grazing (\bar{C}). Where exactly this transition occurs depends on the angular source size.

classification does not just depend on the source trajectory relative to the lens positions, but equally on the angular source size relative to the caustic size. I.e. a given source trajectory (e.g. ST 2 in Figure 10.1) can yield an F-F morphology for a smaller source and a \bar{C} morphology for a larger source, whereas for a given source size ST 1 can result in an F-F pair, but ST 2 will only show a single peak and be classified as \bar{C} .

Another example is Figure 10.2, in which a fold-grazing source trajectory $C\bar{F}C$, across a caustic that is close to the limits of the intermediate-to-wide transition, morphs into a cusp exit/entry pair with an increased source size (C-C C-C).

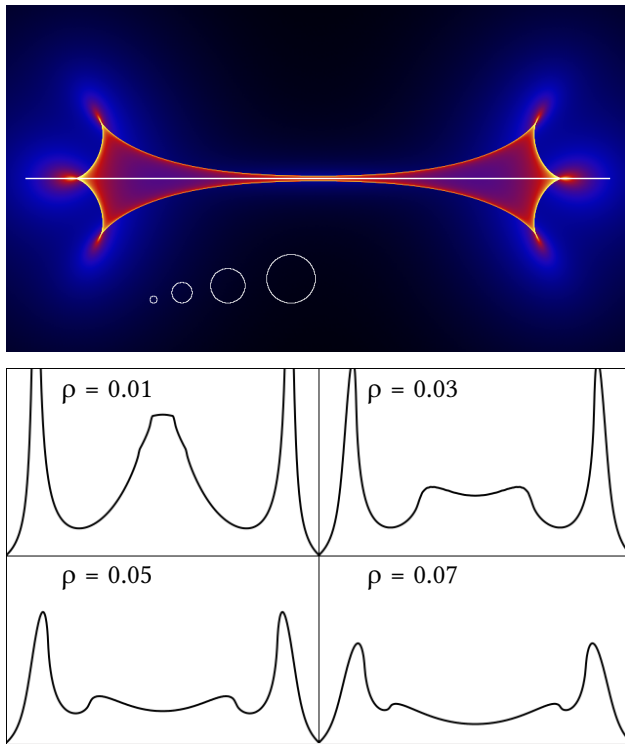


Figure 10.2: Classification in the case of a beak-to-beak metamorphosis. The magnification curves result from the same source trajectory, but with different source sizes (as indicated by the white circles). The smallest source produces an unambiguous *fold-grazing*, as the central peak occurs inside the caustic (C- \bar{F} -C). Interestingly, the larger sources create a central *pair* of peaks instead, thus leading us to classify the light curves as C-C C-C. This might seem counterintuitive, before one considers the convoluted magnification pattern, where it becomes clear that a larger source shifts the position of the beak-to-beak fold merger – thereby causing the caustic topology change to occur at a smaller separation compared to the smaller source.

For our classification, we ignore the absolute and relative strengths of the light curve peaks, but we base the scheme on the observable number of peaks and identifiable peak types. While no observed light curve is ever fully determined (due to the discrete nature of photometric data taking), it is possible to make an educated guess about the *minimum* number of peaks. Gaps in the coverage can hide a peak, but they cannot reduce the number of detected peaks. Data noise and systematics can potentially create a false peak, but this can be dealt with by setting a suitable threshold.

10.2 Notation for binary-lens caustic features

In this chapter, we deviate from the “observability principle” in the sense that a caustic feature (corresponding to a peak) of an observed light curve will generally only be identified after the conclusion of the modelling. Nonetheless, we found the notation scheme presented here to be useful when identifying classes and discussing related light curve types. It also serves as a quick notation for potential models (or rather model classes) for

observed light curves.

All peaks of a binary-lens light curve can be traced back to features of the caustic of the lens system. We have developed a “shorthand” notation for these features, sketched in Figures 10.3, 10.4 and 10.5 and listed in Table 10.1. In this study, we use and depict this shorthand only for the equal-mass binary lens, but we point out its universal applicability to any binary mass ratio.

We denote folds of a caustic with a lower-case letter and cusps with an upper-case letter. As discussed in Section 10.1, peaks arise either when the source trajectory crosses a fold or a cusp (in the projection on the plane of sky) or when the source trajectory passes sufficiently close to a fold (caustic-interior) or a cusp (caustic-exterior).

The caustics of a multiple lens system are lines of strong magnification where the flux of a theoretical point source is infinitely magnified, but it is important to note that the strength of magnification varies considerably between one point on a fold line and another, as well as from one cusp to the next. In the equal-mass binary case, regardless of the specific topology, the points of maximum magnification are the two “A”-cusps on the binary axis, followed by those parts of the “a”-folds closest to the axis.

The four off-axis cusps (“B”) in the intermediate case, cf. Figure 10.4, can be traced across different separations. When the two lenses are moved closer together, the a-folds will eventually merge and split the single caustic line into three separate caustics. The newly created cusps are denoted by “C”. A similar metamorphosis takes place, when the two lenses are set further apart, except that in this case the “b”-folds will merge to form the new “D”-cusps.

All cusps are strongly magnifying compared to their immediate surroundings, but it is always the cusps closest to the binary axis that are the strongest in comparison. After the A-cusps come the C_{tp} or C_{bp} -cusps in the close topology case and the D-cusps in the wide-separation case.

In the close topology, the closer the two lenses are positioned, the further the two triangular, secondary caustics will move out from the axis and they will continually decrease in size and strength, whereas the central caustic only decreases in size but gains in strength,

until at $\lim_{s \rightarrow 0}$ the binary lens becomes indistinguishable from a single lens.

Conversely, in the wide topology, the two arrow-shaped caustics become more and more symmetric towards a diamond shape and decrease in size, until for $\lim_{s \rightarrow \infty}$ the B-cusps point perpendicular to the axis and the D-cusps become more equal in strength to the A-cusps. Ultimately the two caustics converge to two points, at which stage two independent single lenses will be observed rather than one binary system.

The binary axis is taken to point from the heavier (primary) lens to the smaller-mass (secondary) lens, if there is a mass inequality. All peaks arising from features closer to or facing the primary lens are furnished with an index “₁”, whereas those nearer the secondary lens are indexed “₂”. For example, A_2 will be weaker than A_1 , for unequal lens masses. Every set of exactly two point lenses with no external shear⁶ is symmetric in the binary axis. We also want to distinguish the symmetric caustic features, which are mirrored across the binary axis. Quite arbitrarily, we denote them with “_t” or top, if they are on the left-hand side of the binary axis (looking from primary to secondary) and “_b” or bottom, if they lie on the right-hand side. Figures 10.3, 10.4 and 10.5 better illustrate the “logic” behind this choice.

Notation	Meaning
a, b	fold
A, B, C, D	cusps
[a...; [A...	caustic entry (via fold; via cusp)
...a]; ...A]	caustic exit (via fold; via cusp)
[...a...]	fold grazing (always inside (or <i>on</i>) caustic for binary case)
...A...]	caustic grazing (always outside (or <i>on</i>) caustic for binary case)
₁	nearer binary mass 1
₂	nearer binary mass 2
_t	“above” binary axis
_b	“below” binary axis
_p	primary caustic (in close-separation case)
_s	secondary caustic (in close-separation case)

Table 10.1: Caustic feature notation. The sketches in Figures 10.3, 10.4 and 10.5 provide a better overview.

⁶or only shear that is exactly parallel or orthogonal to the binary axis

Considering the special case of an equal-mass binary, we have a second symmetry axis through the centre of mass, i.e. through the midpoint between the two lenses and perpendicular to the binary axis. This does not affect the choice of notation. The chosen caustic feature notation scheme covers *all* scenarios with two point lenses, including mass ratios very different from unity. The notation scheme is summarised in Table 10.1.

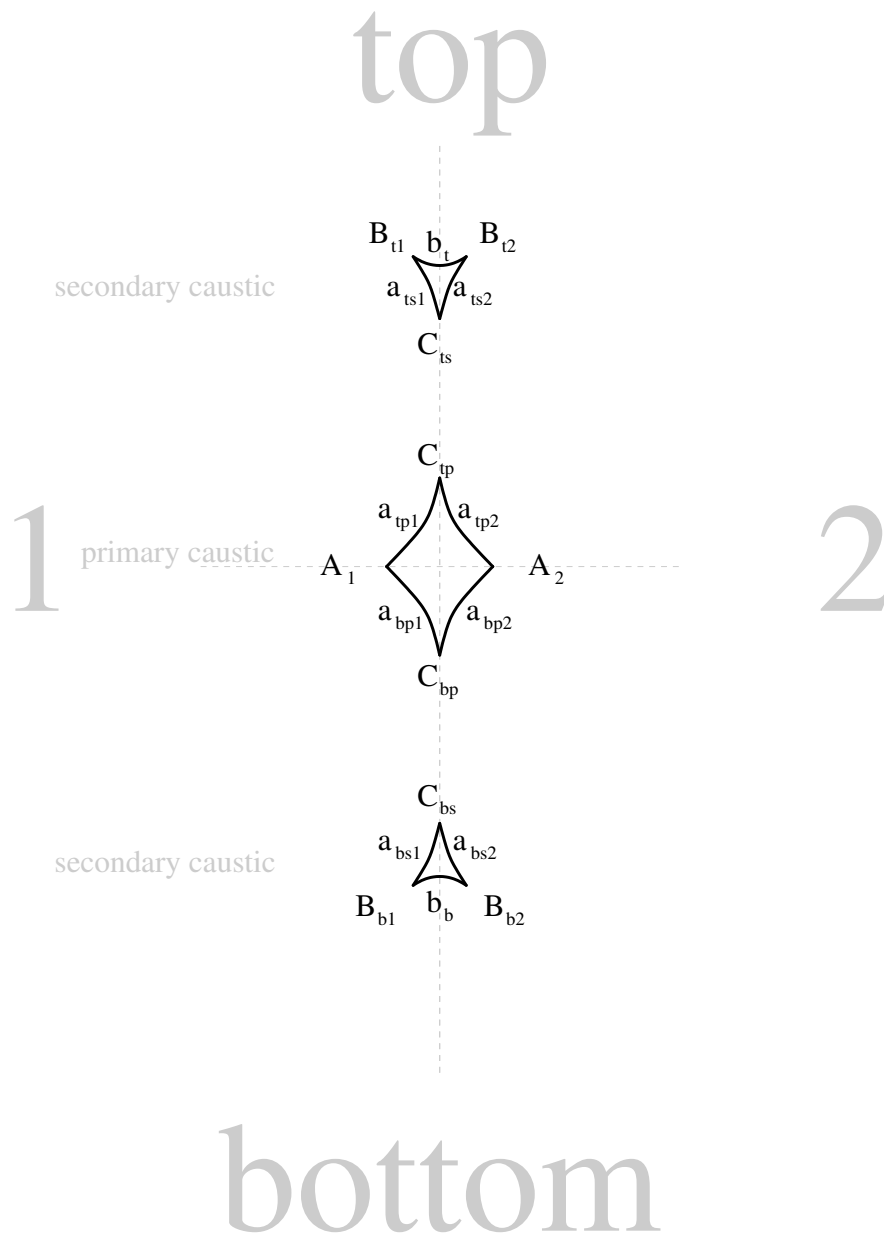


Figure 10.3: Caustic features of the close-separation binary lens.

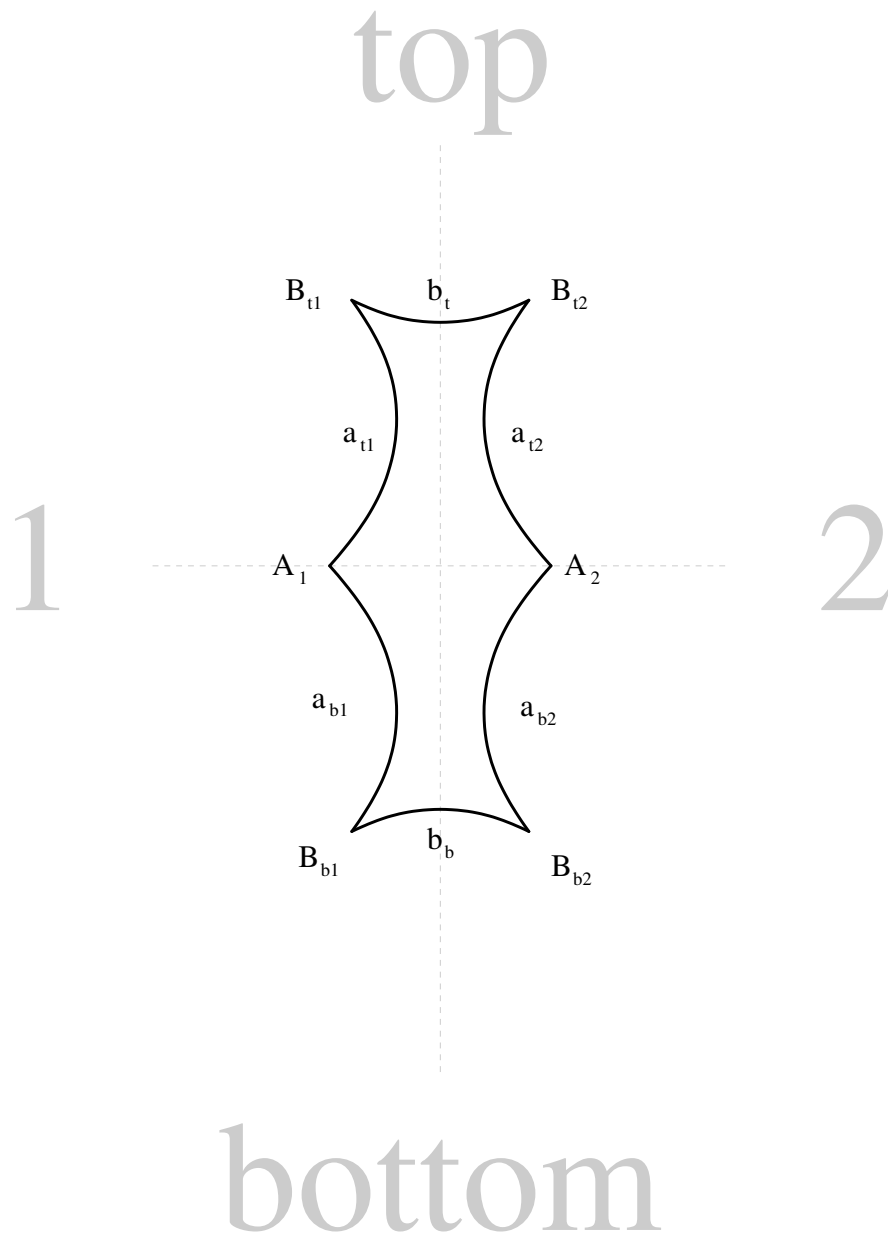


Figure 10.4: Caustic features of the intermediate-separation binary lens.

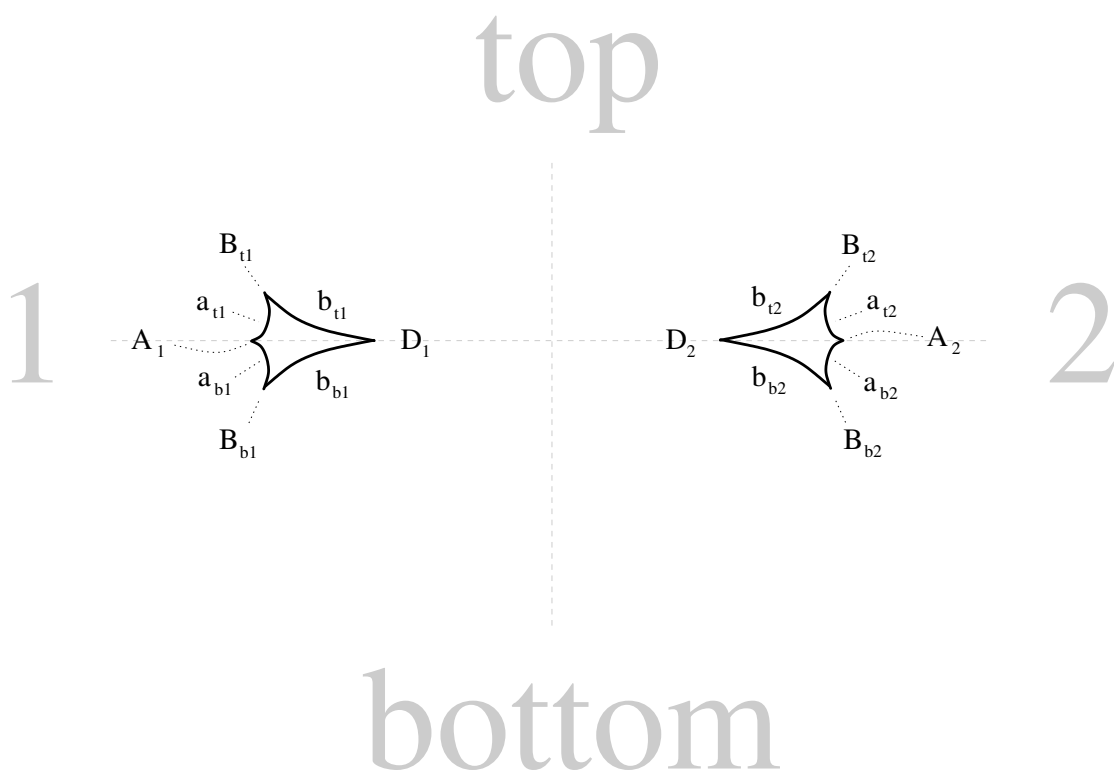


Figure 10.5: Caustic features of the wide-separation binary lens.

11 | Methodology

In order to achieve a complete classification of binary lens light curve morphologies, we process simulated light curves. We then consider light curves grouped in the parameter space by their number of maxima. The parameter space we want to cover is the equal-mass lens ($q = 1$), the separation s across all topologies and the source trajectory parameters $0 \leq \alpha < 2\pi$ and u_0 as far as new morphologies can be expected to occur. We use an extended source with angular radius $0.01 \theta_E$. For each light curve we record the number of peaks and visualise the results in peak-number plots (over α and u_0). The resulting iso-maxima regions are examined with regard to the contained light curve morphologies. Broadly speaking, an iso-maxima region, covering a “bundle” of neighbouring source trajectories, corresponds to a specific sequence of caustic features. One step up in the classification hierarchy, different iso-peak regions are collected in morphology classes (as introduced in Chapter 10).

11.1 Light curve simulation and processing

In our examination of the equal-mass binary lens case, we simulate microlensing light curves for all (relevant) volumes of the s , α , u_0 parameter space. We simulate the light curves with inverse ray shooting, using a software library written in 2010 by Marnach¹. Assuming static lenses, this means we can compute magnification maps for every (q, s) set, fold them with the source star profile with a radius ρ and then extract a large number of light curves differing in α and u_0 at virtually no computational cost. During the peak

¹Published at <https://github.com/smarnach/luckyensing>.

counting, numerical noise can create artificial peaks and troughs, especially for source trajectories that run at a small angle to fold lines. To avoid these, we require a minimal difference between the maximum and the minima on either side of 5% of the nearest local minimum value, before a trough-peak-trough occurrence is counted as a peak. Because of this threshold, sometimes true peaks will be disregarded in the maxima counting algorithm. But this is unlikely to make us miss a whole iso-maxima region, as generally the region boundary (where the formerly disregarded peak becomes significant) will only be slightly shifted in the u_0, α -plane.

An hypothetical point source is often useful in theoretical studies of the behaviour of gravitational lenses, but because we want to examine the range of real, observable light curve morphologies, we use an extended source size of $10^{-2} \theta_E$ for our simulations. The source size does influence the shape of a light curve, as discussed in Chapter 10. A pair of fold crossings can be merged into a single peak, a whole caustic can be crossed and appear as a single peak, but as long as the solid angle of the source area is small relative to the caustic extent, the absolute size will not change the number of distinct morphologies that can be studied. For the studied mass ratio $q = 1$, we can afford to use a moderately large source that reduces the numerical noise in our samples. Meaningful studies of planetary mass ratios $q \lesssim 10^{-3}$, require a smaller source size. We point out that not all of the peak types of Section 10.1 can be simulated with a point source: the cusp crossing can only occur, if the point source enters the caustic *exactly* over the infinitesimal cusp point. The probability for this occurrence is therefore zero.

11.2 Iso-maxima regions

Per examined separation, we plot the number of local maxima per light curve over α, u_0 of its source trajectory, see Figure 11.1.

Beyond the trivial periodicity of α with period 2π , there are several symmetries in the

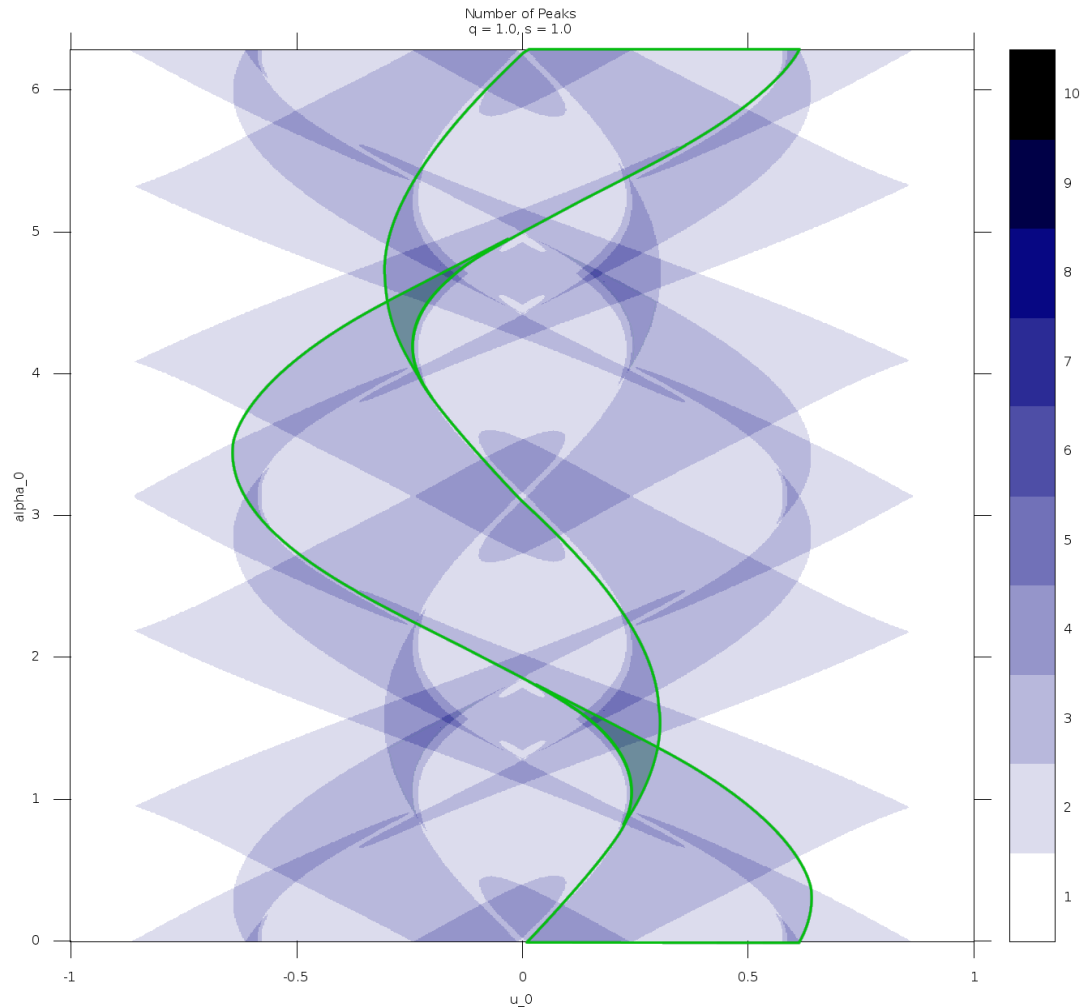


Figure 11.1: Extended plot of the iso-maxima regions to illustrate existing symmetries and the seamless continuation of iso-maxima regions beyond the first quadrant.

Also shown is a caustic feature region: the green outline frames the area where the a_{t1} fold gives rise to a light curve peak, more specifically the top and bottom regions contain the fold entry $[a_{t1} \dots]$ whereas the middle region contains the fold exit $[\dots a_{t1}]$. The green shade marks areas where the a_{t1} fold is crossed twice (requiring $[\dots a_{t1}] [a_{t1} \dots]$ to be part of the light curve). Moving to a slightly smaller u_0 from the shaded area, the light curves will display the fold grazing $[\dots a_{t1} \dots]$.

two-dimensional (u_0, α) space. Generally, for a binary lens,

$$(u_0, \alpha) \Leftrightarrow (-u_0, -\alpha) \quad (11.1)$$

is an exact degeneracy, which is caused by the intrinsic symmetry of the binary lens across the binary axis. Skowron et al. (2009, Appendix A) argues that models for static binaries should be expressed in the range $u \geq 0$ and $0 \leq \alpha < 2\pi$, with the exception of cases that display parallax effect where the apparent source position can appear on both sides of the lens. We generally subscribe to this view, nonetheless it is instructive to, at least once, visualise the “full” parameter space as in Figure 11.1. Since we are interested in the morphology only,

$$(u_0, \alpha) \Leftrightarrow (-u_0, \alpha + \pi), \quad (11.2)$$

gives the symmetry of a time reversal (where the sign of u_0 has to change according to the convention, because the source now passes the lens on the other side). We can also combine the two,

$$(u_0, \alpha) \Leftrightarrow (u_0, \pi - \alpha). \quad (11.3)$$

For the special case of the equal-mass binary, we also have a perfect degeneracy

$$u_0 \Leftrightarrow -u_0, \quad (11.4)$$

i.e. the plot is axis-symmetric in u_0 .

Thanks to these symmetries, we can restrict ourselves to the first quadrant, $0 < u_0$, $0 < \alpha < \pi/2$. In the resulting plots, e.g. Figure 14.4, we can identify and isolate regions of a uniform peak number, so-called *iso-maxima regions*.

We note that whenever one moves from one iso-maxima region to a neighbouring one, the morphology of the light curve peaks changes – naturally, because the border will be overstepped whenever a peak is created or destroyed. In a given quadrant, there are no

two iso-maxima regions with the same number of peaks that contain the same sequence of caustic features.

We also note that it is possible, but rare, to find different morphologies within one iso-peak region, for example when a fold-crossing peak morphs into a cusp crossing with a changing α . Where these occur, we have given two labels to the connected region, an example of this are regions II b-1 and II b-2 in Table 14.5.

We label the iso-maxima regions with a roman numeral, for the number of light-curve peaks counted in that region, followed by a lowercase letter, the alphabetical assignation of which is arbitrarily starting in the origin of the α , u_0 plot. We base our designation on the separation $s = 1.0$, but the same region will have the same label across all separations². There are cases where the caustic feature identification changes with separation just in name. For example, when the a_{t*} folds, with a decreasing lens separation, first merge and then split apart in a beak-to-beak transformation, the remnant folds, a_{ts*} and a_{tp*} , can still cause an F-F class light curve; an $[a_{t1}a_{t2}]$ double fold crossing in the intermediate case is essentially identical to the $[a_{tp1}a_{tp2}]$ and the $[a_{ts1}a_{ts2}]$ in the close-separation case. We choose to reflect these relations with a superscript. For our example, the region II b splits in into two separate regions II b^{cp} (“close separation, primary caustic”) and II b^{cs} (“close separation, secondary caustic”), with the I b region in between where the two a_t folds have merged into a single C-type peak. The superscript ^w is similarly employed for the wide separation case.

We then map the caustic features to the broader peak typology, thereby reducing the complexity of the light curve description and enabling us to collate different regions in more general morphology classes.

²Currently, different regions can have the same name, if have been newly labelled in both, the close and wide topology.

12 | Results

We have computed peak-number plots for a range of mass ratios and separations, as presented in Figure 12.1. An intriguing picture emerges as we see how different iso-maxima regions stretch across the four-dimensional q - s - u_0 - α space. A decreasing mass ratio q renders the plots increasingly asymmetric. While the plots in column $s = 1$ show a fairly even distribution of multi-peak regions in the higher mass ratios, we can see that the areas of “high activity”, i.e. with high peak counts and small iso-maxima regions, correspond to the caustic axes in the closer ($u_0 \sim 0$, $\alpha \sim \pi/2$) and wider ($u_0 \sim 0$, $\alpha \sim 0$) separation cases.

Focussing on the equal-mass binary lens, we analysed peak-number plots spanning all caustic topologies and the two transitioning cases (cf. Figure 9.2): close ($s = 0.65$), close-to-intermediate ($s = 0.7$), intermediate ($s = 0.85, 1.0, 1.5$), intermediate-to-wide ($s = 2.05$) and wide ($s = 2.5$). As discussed in Section 11.1, we were motivated to use an extended source with an angular radius, $\rho = 0.01$ (in units of Einstein angles) and work with a peak threshold of 5% above the nearest minima. The detailed iso-maxima region results are printed in the appendix Chapter 14; we provide a summary and an overview here.

Within the peak-number plots, we know the light curve composition in each (substantial) iso-maxima region, i.e. we know which sequence of caustic features produces the observable peaks of all light curves in that region. We note that it is mostly a bijective mapping, with only very few regions containing more than one kind of caustic feature sequences. In no case, do two unconnected regions share the same caustic feature sequence.

The light curves (and iso-maxima regions) are collected in morphology classes, where each peak is morphologically classified as one of the following: cusp-grazing, cusp-crossing, fold-crossing or fold-grazing. A substantial subset of morphology classes can be found in

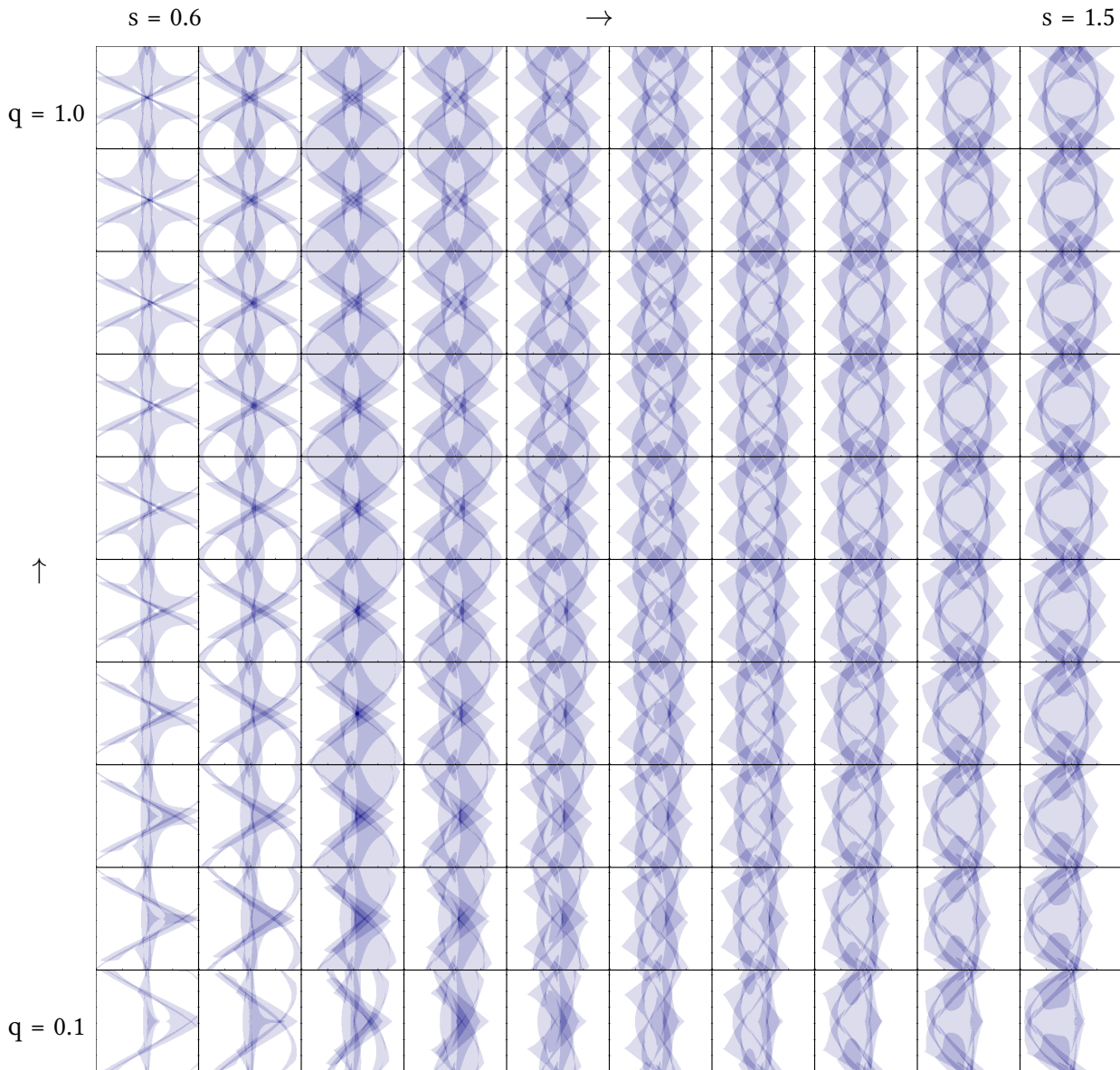


Figure 12.1: Overview over the iso-maxima regions for a nested $[s, q]$, $[u_0, \alpha]$ grid. The larger grid covers the range $0.6 \leq s \leq 1.5$, $0.1 \leq q \leq 1.0$ in steps of 0.1. In each of the 100 subplots, the colour-coded peak-count per source trajectory is plotted over the range $-1.0 \leq u_0 \leq 1.0$, $0.0 \leq \alpha \leq \pi/2$. *White* means the light curve has a single peak, *black* means ten peaks (there are only a handful of nine-peak and ten-peak light curves). The first row corresponds to ten different separations of the equal-mass binary lens.

all examined separation settings. Other classes only appear when a higher or lower separation leads to multi-caustic topologies, whereas the specific example of a double fold grazing is necessarily limited to the intermediate caustic cases¹.

Table 12.1 provides an overview over the complete classification. Sample light curves for each morphology class can be studied in Figures 12.2 to 12.6.

¹Although it will reappear in the arrow-shaped primary caustic of extreme mass ratios.

12.1 Classes overview

Table 12.1: Summary of morphology classes. Sample light curves in Figures 12.2 to 12.6.

	Morphology Class	s = 0.65	s = 0.7	s = 0.85	s = 1.0	s = 1.5	s = 2.05	s = 2.5
I	\bar{C}	✓	✓	✓	✓	✓	✓	✓
II	F-F	✓	✓	✓	✓	✓	✓	✓
	$\bar{C}\bar{C}$	✓	✓	✓	✓	✓	✓	✓
	C-C	✓	✓	✓	✓	✓		
	C-F	✓	✓			✓	✓	
III	\bar{C} F-F	✓	✓	✓	✓	✓	✓	✓
	F- \bar{F} -F	✓	✓	✓	✓	✓	✓	✓
	C-F \bar{C}	✓	✓	✓	✓	✓	✓	✓
	$\bar{C}\bar{C}\bar{C}$	✓	✓	✓	✓	✓	✓	✓
	C- \bar{F} -F					✓		
IV	\bar{C} F-F \bar{C}	✓	✓	✓	✓	✓	✓	✓
	F-F F-F	✓	✓	✓	✓	✓	✓	✓
	F- \bar{F} -F \bar{C}	✓	✓	✓	✓	✓	✓	
	F- \bar{F} - \bar{F} -F			✓	✓			
	C-F F-F					✓	✓	
	F-F $\bar{C}\bar{C}$	✓	✓				✓	✓
	C-C C-C						✓	✓
V	\bar{C} F-F F-F	✓	✓	✓	✓	✓	✓	✓
	F-F F- \bar{F} -F			✓	✓			
	\bar{C} F- \bar{F} -F \bar{C}					✓	✓	
	F-F \bar{C} F-F	✓	✓				✓	✓
	\bar{C} F-F $\bar{C}\bar{C}$	✓	✓					✓
	\bar{C} F-C F-F	✓	✓					✓
	\bar{C} F-F C-F	✓						
	C-C F-F \bar{C}						✓	
	C-F F-F \bar{C}						✓	
C-F \bar{C} F-F							✓	
VI	F-F F-F F-F		✓	✓	✓			
	\bar{C} F-F F-F \bar{C}					✓	✓	✓
	\bar{C} F-F \bar{C} F-F	✓					✓	✓
	C-F \bar{C} F-F \bar{C}						✓	✓
	C-C \bar{C} F-F \bar{C}							✓
	\bar{C} F-C F-F \bar{C}							✓
	F-F F-C F-F		✓					
	\bar{C} F-F \bar{C} C-F	✓						
VII	\bar{C} F-F \bar{C} \bar{C} F-F	✓						
	\bar{C} F-F \bar{C} F-F \bar{C}						✓	✓
	\bar{C} F-C \bar{C} F-F \bar{C}							✓
	C-F $\bar{C}\bar{C}$ F-F \bar{C}							✓
VIII	\bar{C} F-F \bar{C} \bar{C} F-F \bar{C}							✓

Figure 12.2: Morphology class sample light curves. Plotted is the magnification on a logarithmic scale in the uniform range from 1 to 50. The small plot shows the corresponding caustic topology and the source trajectory. Caustics computed with Caustic Finder by Schmidt, published 2008 at causticfinder.sourceforge.net.

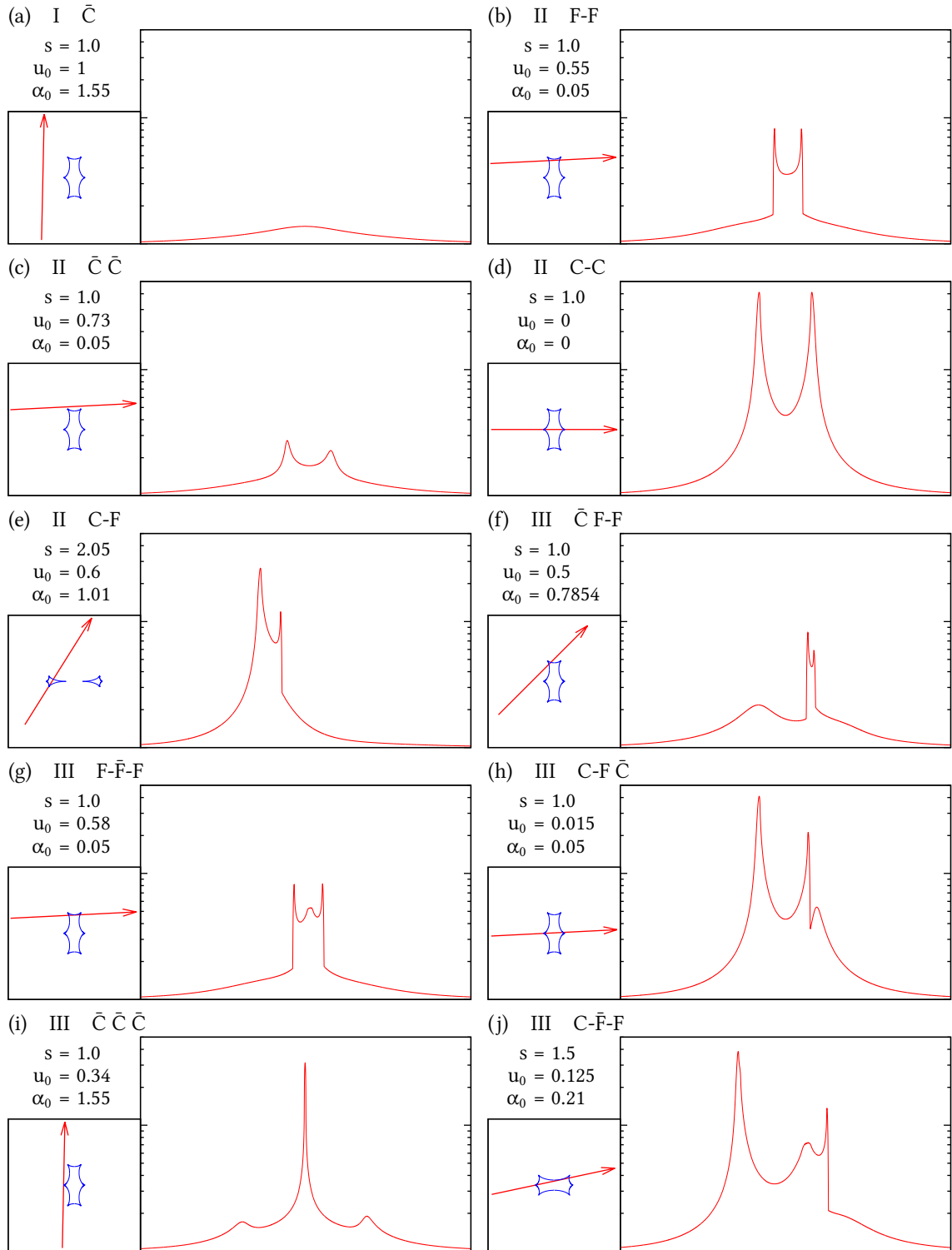


Figure 12.3: Morphology class sample light curves. (Continued.)

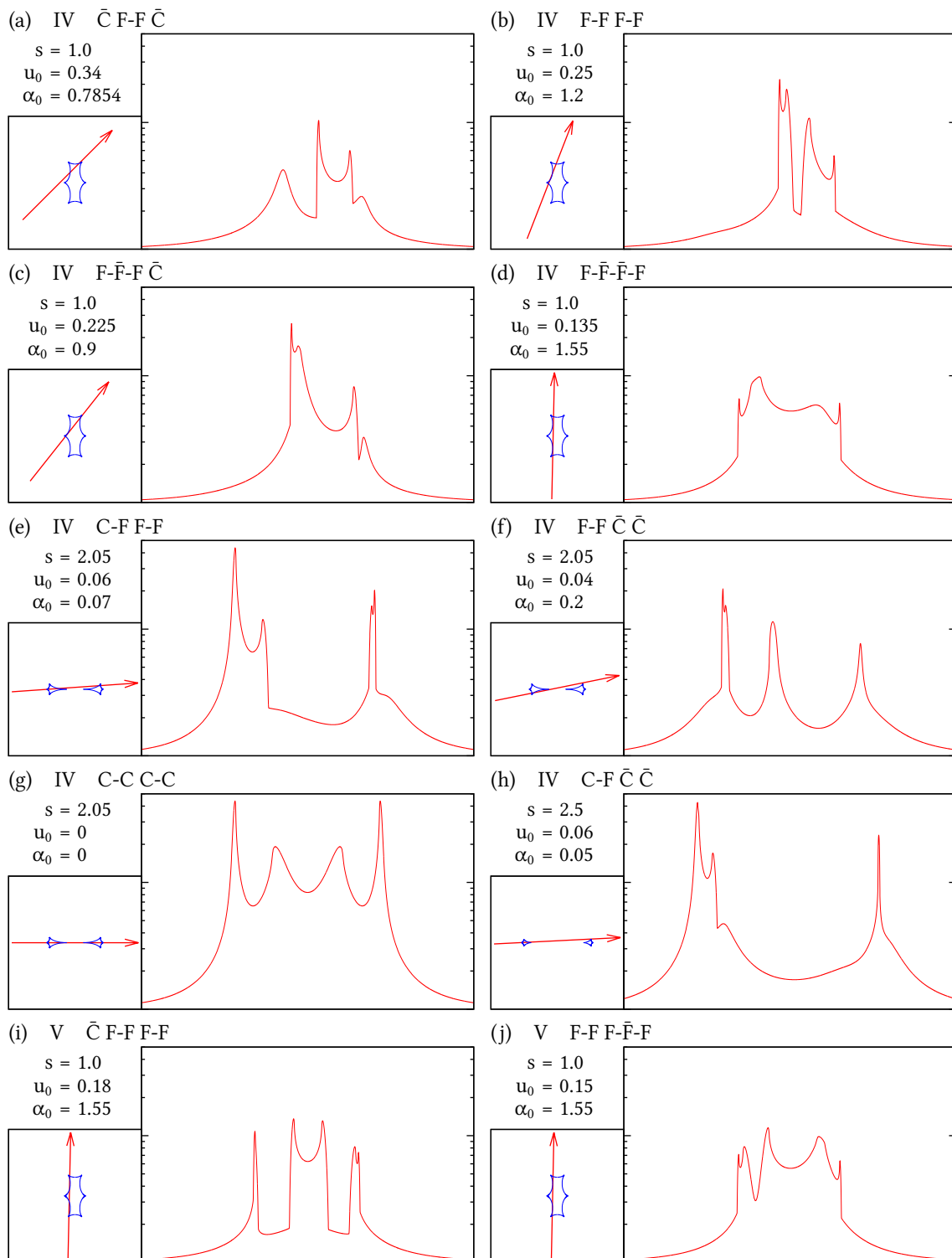


Figure 12.4: Morphology class sample light curves. (Continued.)

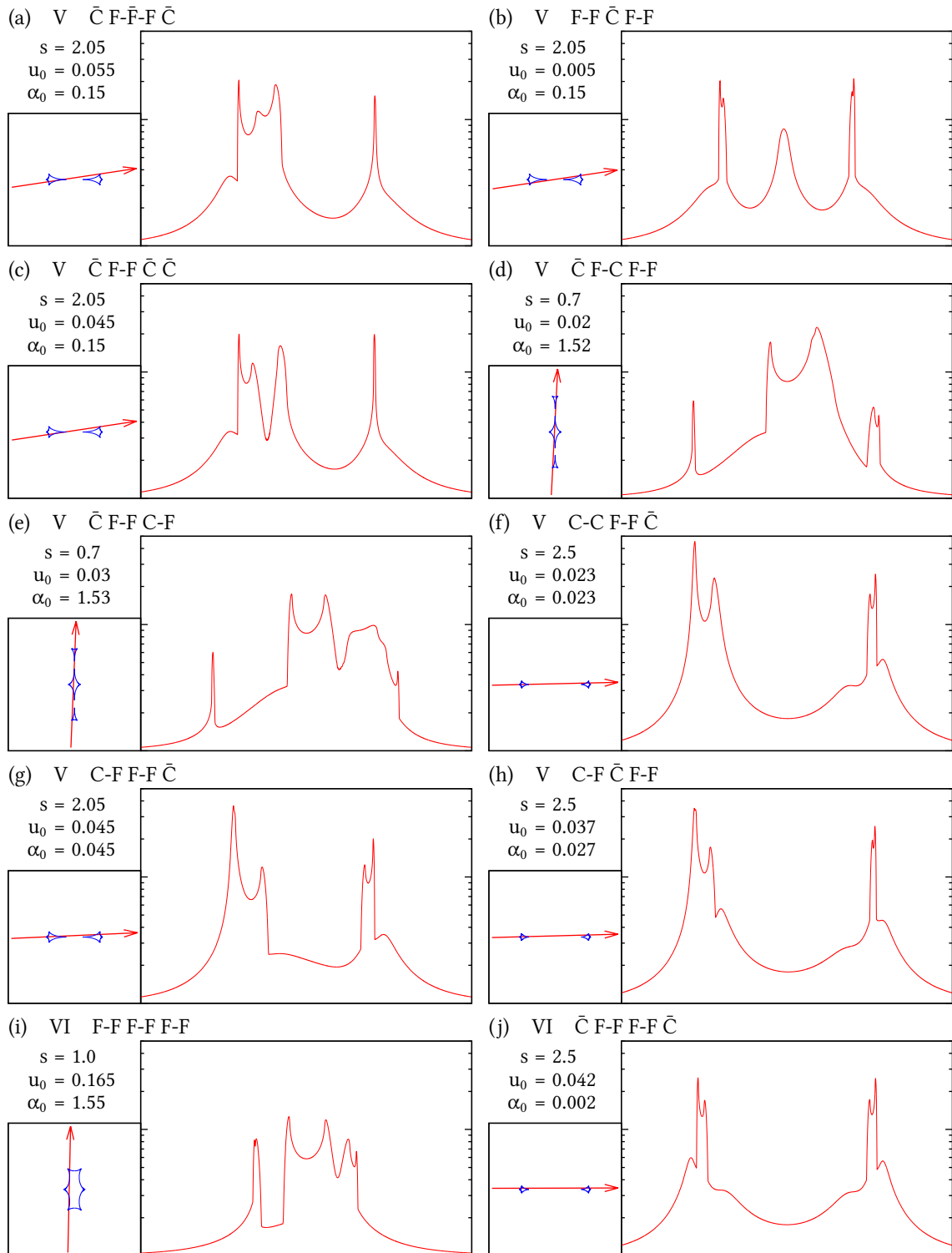


Figure 12.5: Morphology class sample light curves. (Continued.)

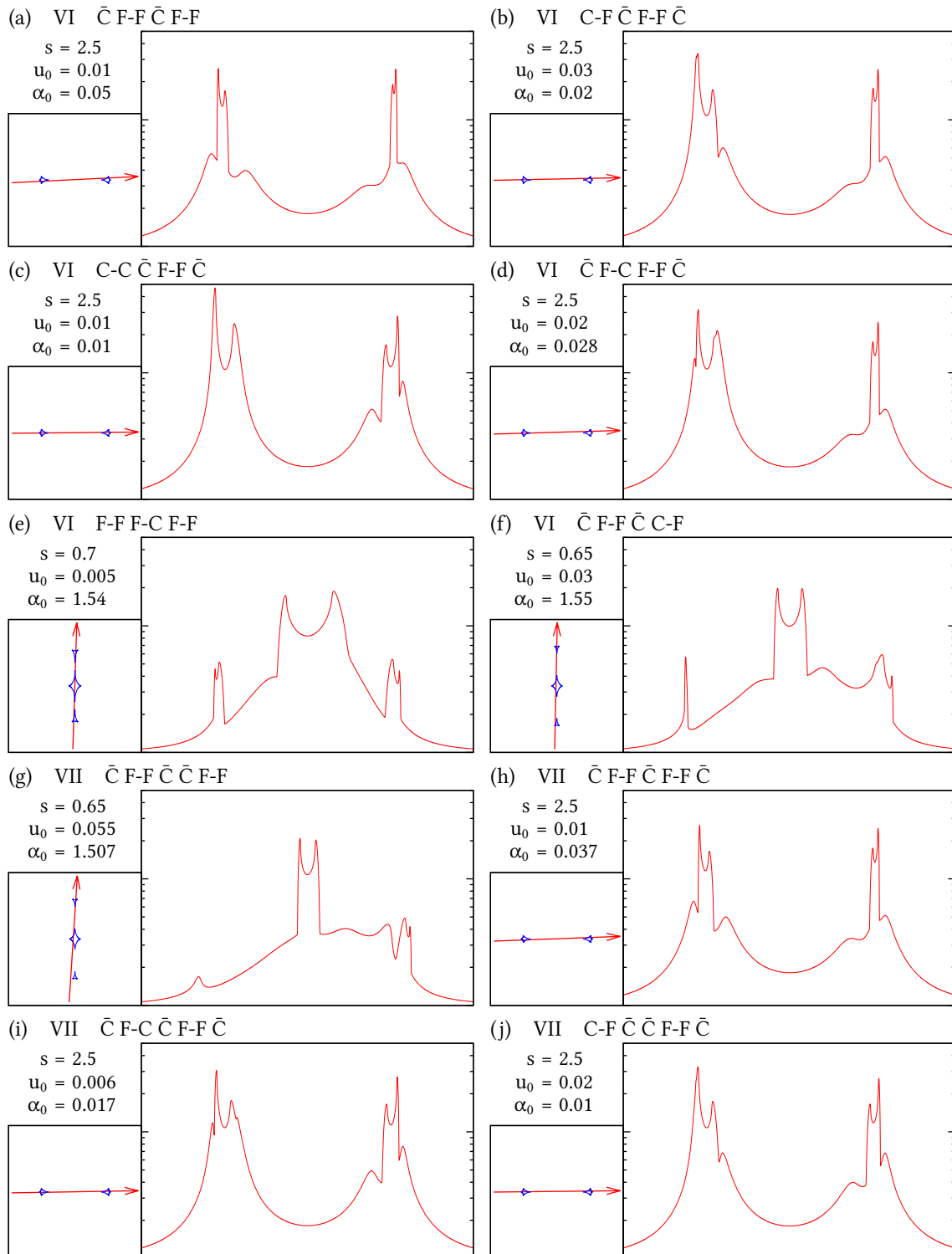
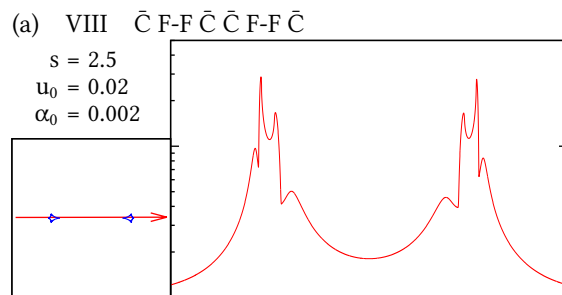


Figure 12.6: Morphology class sample light curves. (Continued.)

12.2 Further considerations

Source size Two peaks will generally merge into one, if their angular separation is smaller than the angular source diameter (disregarding limb-darkening effects). In our simulations the source has a diameter of $2 \times 10^{-2} \theta_E$, i.e. peaks within $2 \times 10^{-2} t_E$ of each other would be missed. We work with the (unproven) assumption that a larger source size can only lead to a smaller number of identified morphologies. We demonstrate this for $q = 1.0$, $s = 1.0$ in Figure 12.7.



Figure 12.7: Comparison of peak-number plots resulting from different source sizes (from left to right: $\rho = 0.005, 0.01, 0.02$), scale and ranges as in Figure 14.4: x -axis: $0 \leq u_0 \leq 1.0$, y -axis: $0.0 \leq \alpha \leq \pi/2$, *white* means the light curve has a single peak, *dark blue* means six peaks. The change in iso-maxima regions is subtle, but noticeable. The smallest source not only leads to more iso-maxima regions, but also to more numerical artefacts.

D’Ago already has complementary classification results for the equal-mass binary with a smaller source ($\rho = 0.002$), which show additional morphological classes, especially in the non-intermediate topology regimes, and contain light curves with higher peak counts (up to ten peaks for close separations, in the F-F \bar{C} \bar{C} F-F \bar{C} \bar{C} F-F class).

We also refer to our motivation for an extended source in Section 11.1.

Error margin While we aim for completeness, due to the numerical nature of our study we have to ignore very small sub-regions of the studied parameter space and therefore might have missed out on a particular light curve morphology. Within this space we have examined all iso-maxima regions larger than 10 by 10 pixel, i.e. $10^2 \times 1/(u_0\text{-sampling}) \times$

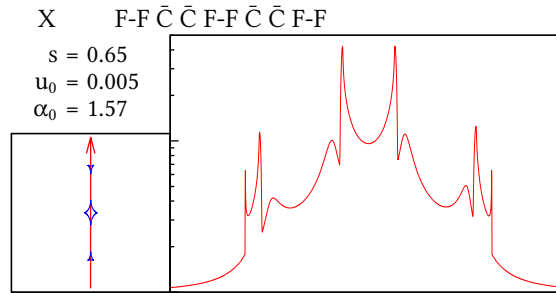


Figure 12.8: Example for a ten-peaked, binary-lens light curve (angular source radius: $\rho = 0.002$). The magnification is plotted in the range from 1 to 50 in a logarithmic scale. The small plot shows the corresponding caustic topology and the source trajectory. Caustics computed with Caustic Finder by Schmidt, published 2008 at `causticfinder.sourceforge.net`.

$\frac{\pi}{2}/(\alpha\text{-sampling})$, meaning that within a given Einstein radius and with our sampling of 800, the probability to observe that particular light curve morphology is smaller than $\lesssim 1/3200$.

χ^2 landscape We consider the relations between the iso-maxima regions and the topography of the optimisation surface in Figures 12.9 and 12.10. Even though the visualisation is restricted to two dimensions (u_0, α), it is still striking to see the large number of local minima that a modeller has to deal with. It remains to be explored whether or not there can be more than one local minimum in a single morphology region. In particular, the study needs to be expanded in q and s . But even at this stage one can draw conclusions from the distribution of iso-maxima regions: where they occur at a high-density, the grid of initial model seeds should be refined to match their density. In Figure 12.10, the plot of the L^2 norm emphasises the prominence of cusp traverses on the optimisation surface.

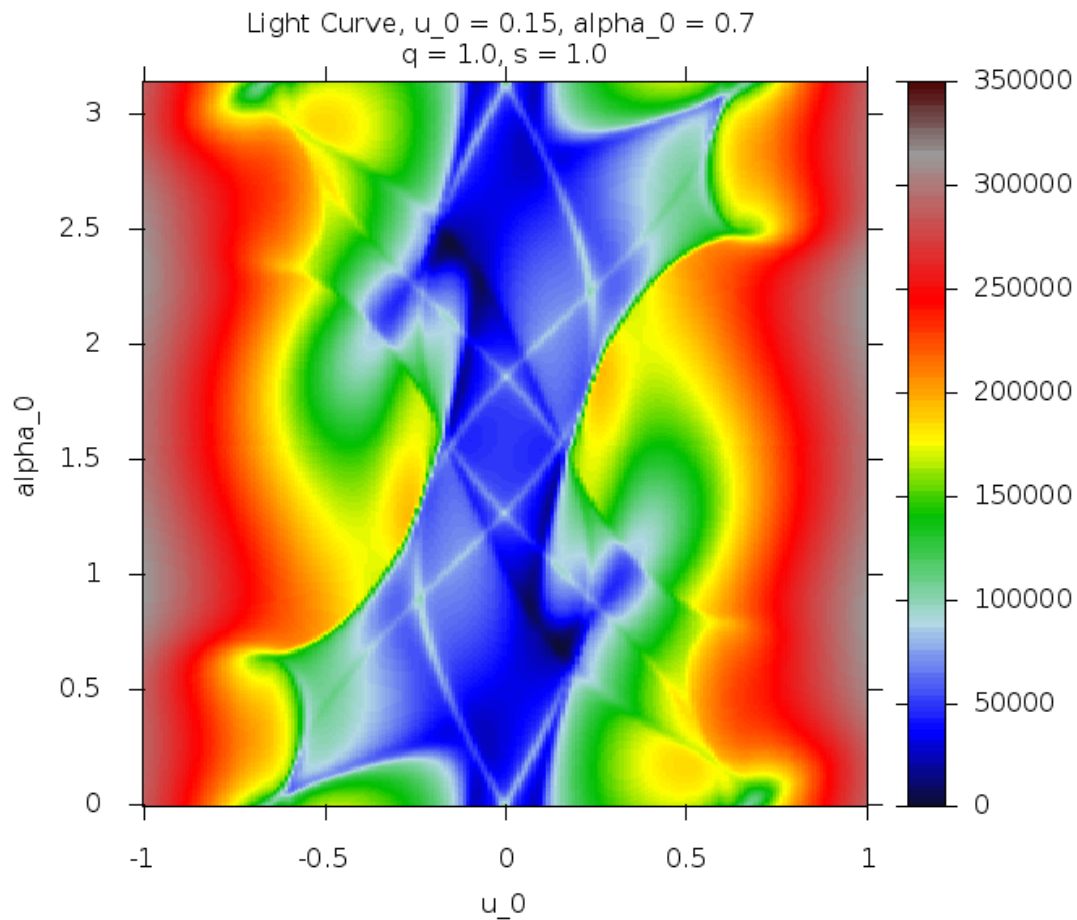


Figure 12.9: Topography of the χ^2 landscape corresponding to Figure 11.1 ($q = 1.0, s = 1.0, u_0, \alpha$). This is an arbitrary example for the χ^2 values from comparing the sample light curve ($q = 1.0, s = 1.0, u_0 = 0.15, \alpha = 0.7$) with each light curve on the plot. Every pixel shows the resulting goodness-of-fit value (only the relative values are of interest here). There is a large number of local minima and one perfect degeneracy due to the equal-lens-masses symmetry, $(u_0, \alpha) \Leftrightarrow (-u_0, \pi - \alpha)$. It remains to be confirmed whether or not there can be more than one local minimum in a single iso-maxima region. Some of the ridges are caused by cusp traverses, as illustrated in Figure 12.10.

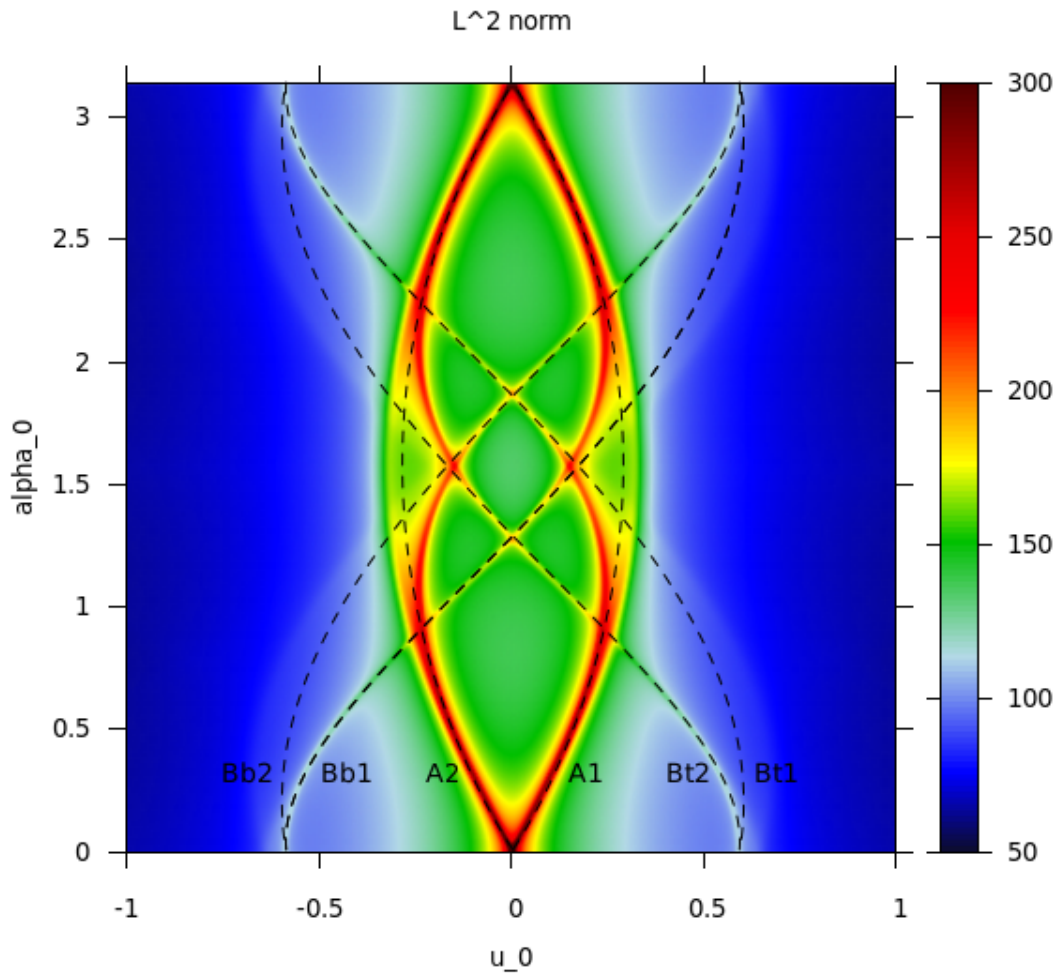


Figure 12.10: Topography of the $(q = 1.0, s = 1.0, u_0, \alpha)$ parameter space. Each pixel shows the L^2 norm of the corresponding light curve (i.e. $\sqrt{\sum \text{data}(i)^2}$). The ridges partly correspond to the cusp-crossing light curves, marked by the dashed lines, which cross one of the six cusps of the intermediate binary caustic ($A_1, A_2, B_{t1}, B_{t2}, B_{b1}, B_{b2}$ as indicated), also cf. Night, Di Stefano & Schwamb (2008, Figure 2). Where the red ridge diverges from the dashed lines, the source trajectories lie very close to the a-folds, i.e. the light curves contain either a fold grazing or fold exit-entry pair on the fold (a_{t1} in the first quadrant).

13 | Conclusion and future prospects

We have compiled an unprecedented catalogue of microlensing light curve morphologies for the equal-mass binary lens. We realised that all peaks in microlensing light curves can be classified in just four categories: cusp-grazing, cusp-crossing, fold-crossing or fold-grazing. In order to achieve this complete classification, we have developed a general notation scheme for the features of binary-lens caustics. Our tool, plots of peak number over u_0 and α , serves to provide insight into the the microlensing parameter space.

To drive this study further, it is essential to improve the workflow from light curve to morphology class. Fortunately, D'Ago has recently recognised the inherent ability of image-contouring microlensing codes to automatically classify a simulated light curve (private communication). Image-contouring code has to keep track of image locations and image boundaries at any given point in the modelling process (cf. Bozza (2001); Dominik (2007)). Whenever the source enters a caustic via a fold, a pair of images is created at the corresponding point of the critical curve. Initially, the two image centres – one inside and one outside of the critical curve – will be enclosed by a common image contour. When the whole extended source has traversed the fold, the images will split. Essentially, by image tracing and contouring we know that a source is straddling a fold, whenever there are two image centres contained in one image boundary. If the source sits on a cusp, there will be three image centres in one connected image boundary (which can be visualised as an image pair destruction and creation happening simultaneously). Combined with the knowledge of whether the source is caustic-interior or exterior, before and after the traversal, we can unambiguously determine the peak type. With this level of automatism, it will be feasible to extend the classification towards planetary mass ratios and smaller source sizes.

Once this has been achieved, the scheme can unfold its full potential and help to refine the initial seeding of modelling codes.

We have only very briefly mentioned the existence of caustic-feature regions as “meta regions” to the iso-maxima regions, i.e. the combination of all iso-maxima regions containing one specific, caustic-related peak. Unfortunately, we have not yet found a good way to extract and preserve the information about these meta regions, but in fact they can provide a more fundamental understanding of the parameter space, since iso-maxima regions are basically just “stacks” of caustic-feature regions. In contrast to iso-maxima regions, caustic-feature regions are smooth structures and, like the caustics they are derived from, they change continuously over the parameter space. If their boundaries could be analytically derived from the caustic lines, an even more elegant solution to the automatic classification could be reached.

14 | Appendix Morphology

All results presented here were computed for the equal-mass binary, $q = 1$, with a flat-disk source, $\rho = 0.01$, and a peak counting threshold of 5%.

14.1 Angular lens separation $s = 0.65$

Figure 14.1: Iso-maxima regions. $s = 0.65$.

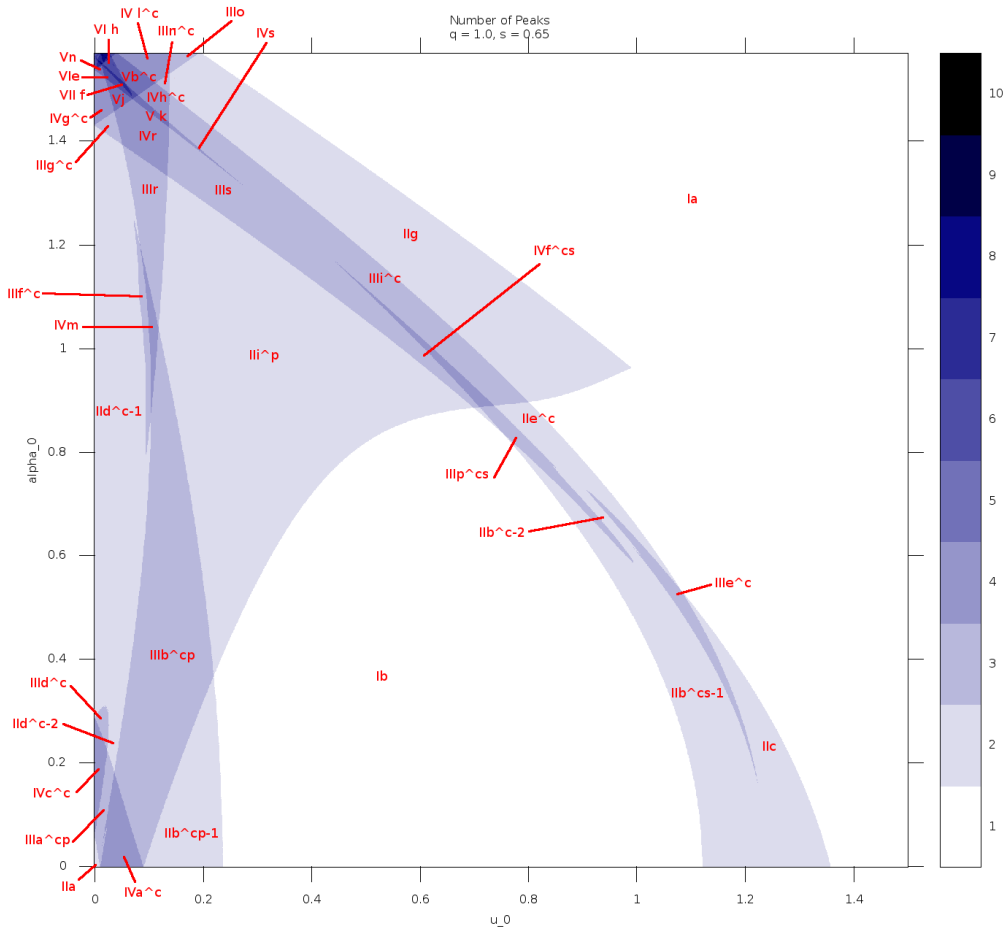


Table 14.1: Caustic feature sequences for iso-maxima plot in Figure 14.1 ($q = 1.0, s = 0.65$).

Iso – maximaregion	Caustic feature sequence	Morphology class
Ia	outside caustics	\bar{C}
Ib	between caustics	\bar{C}
IIa	$[A_1 A_2]$	C-C
IIb ^c – 2	$[a_{ts1} B_{t2}]$	F-C
IIb ^{cp} – 1	$[a_{tp1} a_{tp2}]$	F-F
IIb ^{cs} – 1	$[a_{ts1} a_{ts2}]$	F-F
IIc	$B_{t1} B_{t2}$	$\bar{C} \bar{C}$
IIc ^c – 1	$[a_{bp1} a_{tp2}]$	F-F
IIc ^c – 2	$[A_1 a_{tp2}]$	C-F
IIe ^c	$[a_{ts1} b_t]$	F-F
IIg	$A_1 B_{t1}$	$\bar{C} \bar{C}$
IIi ^p	$A_1 C_{tp}$	$\bar{C} \bar{C}$
IIIa ^{cp}	$[A_1 a_{tp2}] A_2$	C-F \bar{C}
IIIb ^{cp}	$A_1 [a_{tp1} a_{tp2}]$	\bar{C} F-F
IIIc ^c	$A_1 [a_{bp1} a_{tp2}]$	\bar{C} F-F
IIIe ^c	$[a_{ts1} b_t] B_{t2}$	F-F \bar{C}
IIIf ^c	$[a_{bp1} a_{tp1} a_{tp2}]$	F- \bar{F} -F
IIIg ^c	$[a_{bp1} a_{tp2}] B_{t2}$	F-F \bar{C}
IIIi ^c	$A_1 [a_{ts1} b_t]$	\bar{C} F-F
IIIj ^c	$[a_{bp1} a_{tp1}] B_{t1}$	F-F \bar{C}
IIIk	$B_{b1} A_1 B_{t1}$	$\bar{C} \bar{C} \bar{C}$
IIIp ^{cs}	$[a_{ts1} a_{ts2}] B_{t2}$	F-F \bar{C}
IIIr	$[a_{bp1} a_{tp2}] C_{tp}$	F-F \bar{C}
IIIs	$A_1 C_{ts} B_{t2}$	$\bar{C} \bar{C} \bar{C}$
IVa ^c	$A_1 [a_{tp1} a_{tp2}] A_2$	\bar{C} F-F \bar{C}
IVc ^c	$A_1 [a_{bp1} a_{tp2}] A_2$	\bar{C} F-F \bar{C}
IVf ^{cs}	$A_1 [a_{ts1} a_{ts2}] B_{t2}$	\bar{C} F-F \bar{C}
IVg ^c	$B_{b1} [a_{bp1} a_{tp2}] B_{t2}$	\bar{C} F-F \bar{C}
IVh ^c	$[a_{bp1} a_{tp1}] [a_{ts1} b_t]$	F-F F-F
IVl ^c	$B_{b1} [a_{bp1} a_{tp1}] B_{t1}$	\bar{C} F-F \bar{C}
IVm ^c	$[a_{bp1} a_{tp1}] [a_{tp1} a_{tp2}]$	F-F F-F
IVr	$[a_{bp1} a_{tp1}] C_{tp} B_{t2}$	F-F $\bar{C} \bar{C}$
IVs	$A_1 C_{ts} [a_{ts2} b_t]$	$\bar{C} \bar{C}$ F-F
IVt ^c	$A_1 [a_{ts1} a_{ts2} b_t]$	\bar{C} F- \bar{F} -F
Vb ^c	$B_{b1} [a_{bp1} a_{tp1}] [a_{ts1} b_t]$	\bar{C} F-F F-F
Vj	$B_{b1} [a_{bp1} a_{tp1}] C_{tp} B_{t2}$	\bar{C} F-F $\bar{C} \bar{C}$
Vk	$[a_{bp1} a_{tp1}] C_{ts} [a_{ts1} b_t]$	F-F \bar{C} F-F
Vn	$B_{b1} [a_{bp1} C_{tp}] [a_{ts2} b_t]$	\bar{C} F-C F-F
VIe	$B_{b1} [a_{bp1} a_{tp1}] C_{tp} [a_{ts2} b_t]$	\bar{C} F-F \bar{C} F-F

Continued on next page.

Table 14.1: Continued. ($q = 1.0, s = 0.65$)

Iso – maximaregion	Caustic feature sequence	Morphology class
VIh	$B_{b1}[a_{bp1}a_{tp1}]C_{tp}[C_{ts}b_t]$	$\bar{C} F-F \bar{C} C-F$
VIIIf	$B_{b1}[a_{bp1}a_{tp1}]C_{tp}C_{ts}[a_{ts2}b_t]$	$\bar{C} F-F \bar{C} \bar{C} F-F$

Table 14.2: Morphology classification of equal-mass binary lens light curves for separation $s = 0.65$. Asymmetric morphologies and their time reversals are classed together.

Morphology class	Iso – maximaregions
\bar{C}	Ia, b
C-C	IIa
F-F	IIb ^{cp} – 1, b ^{cs} – 1, d ^c – 1, e ^c
$\bar{C} \bar{C}$	IIc, g, i ^p
F-C	IIb ^c – 2, d ^c – 2
C-F \bar{C}	IIIa ^{cp}
$\bar{C} F-F$	IIIb ^{cp} , d ^c , e ^c , g ^c , i ^c , n ^c , p ^{cs} , r
F- \bar{F} -F	IIIf ^c ,
$\bar{C} \bar{C} \bar{C}$	IIIo, s
$\bar{C} F-F \bar{C}$	IVa ^c , c ^c , f ^{cs} , g ^c , l ^c
F-F F-F	IVh ^c , m ^c
F-F $\bar{C} \bar{C}$	IVr, s
F-F F-F \bar{C}	Vb ^c
$\bar{C} F-F \bar{C} \bar{C}$	Vj
$\bar{C} F-C F-F$	Vn
F-F $\bar{C} F-F$	Vk
$\bar{C} F-F \bar{C} F-F$	VIe
$\bar{C} F-F \bar{C} C-F$	VIh
$\bar{C} F-F \bar{C} \bar{C} F-F$	VIIIf

14.2 Angular lens separation $s = 0.7$

Figure 14.2: Iso-maxima regions. $s = 0.7$.

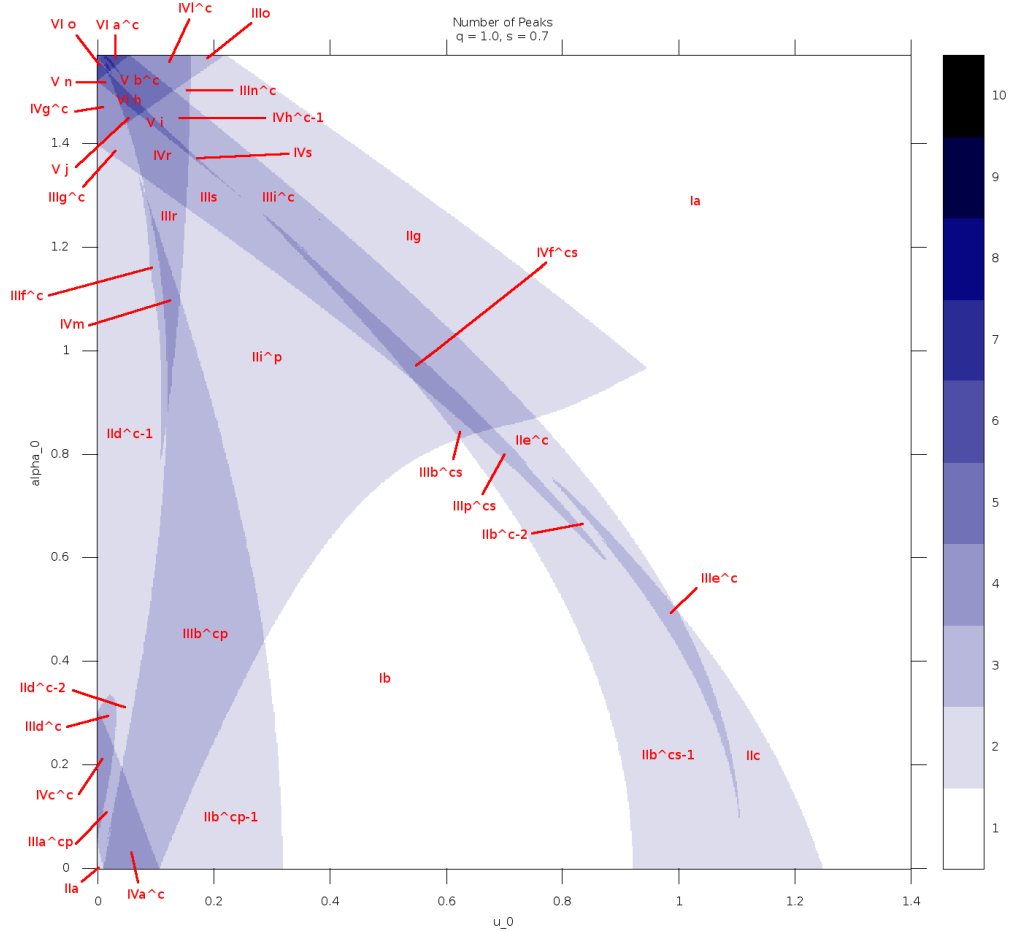


Table 14.3: Caustic feature sequences for iso-maxima plot in Figure 14.2 ($q = 1.0$, $s = 0.7$).

Iso-maxima region	Caustic feature sequence	Morphology class
I a	outside caustics	\bar{C}
I b	between caustics	\bar{C}
II a	$[A_1 A_2]$	C-C
II b ^c - 2	$[a_{ts1} B_{t2}]$	F-C
II b ^{cp} - 1	$[a_{tp1} a_{tp2}]$	F-F
II b ^{cs} - 1	$[a_{ts1} a_{ts2}]$	F-F
II c	$B_{t1} B_{t2}$	$\bar{C} \bar{C}$
II d ^c - 1	$[a_{bp1} a_{tp2}]$	F-F

Continued on next page.

Table 14.3: Continued. ($q = 1.0, s = 0.7$)

Iso-maxima region	Caustic feature sequence	Morphology class
II d ^c - 2	$[A_1 a_{tp2}]$	C-F
II e ^c	$[a_{ts1} b_t]$	F-F
II g	$A_1 B_{t1}$	$\bar{C} \bar{C}$
II i ^p	$A_1 C_{tp}$	$\bar{C} \bar{C}$
III a ^{cp}	$[A_1 a_{tp2}] A_2$	C-F \bar{C}
III b ^{cp}	$A_1 [a_{tp1} a_{tp2}]$	\bar{C} F-F
III b ^{cs}	$A_1 [a_{ts1} a_{ts2}]$	\bar{C} F-F
III d ^c	$A_1 [a_{bp1} a_{tp2}]$	\bar{C} F-F
III e ^c	$[a_{ts1} b_t] B_{t2}$	F-F \bar{C}
III f ^c	$[a_{bp1} a_{tp1} a_{tp2}]$	F- \bar{F} -F
III g ^c	$[a_{bp1} a_{tp2}] B_{t2}$	F-F \bar{C}
III i ^c	$A_1 [a_{ts1} b_t]$	\bar{C} F-F
III n ^c	$[a_{bp1} a_{tp1}] B_{t1}$	F-F \bar{C}
III o	$B_{b1} A_1 B_{t1}$	$\bar{C} \bar{C} \bar{C}$
III p ^{cs}	$[a_{ts1} a_{ts2}] B_{t2}$	F-F \bar{C}
III r	$[a_{bp1} a_{tp2}] C_{tp}$	F-F \bar{C}
III s	$A_1 C_{ts} B_{t2}$	$\bar{C} \bar{C} \bar{C}$
IV a ^c	$A_1 [a_{tp1} a_{tp2}] A_2$	\bar{C} F-F \bar{C}
IV c ^c	$A_1 [a_{bp1} a_{tp2}] A_2$	\bar{C} F-F \bar{C}
IV f ^{cs}	$A_1 [a_{ts1} a_{ts2}] B_{t2}$	\bar{C} F-F \bar{C}
IV g ^c	$B_{b1} [a_{bp1} a_{tp2}] B_{t2}$	\bar{C} F-F \bar{C}
IV h ^c - 1	$[a_{bp1} a_{tp1}] [a_{ts1} b_t]$	F-F F-F
IV l ^c	$B_{b1} [a_{bp1} a_{tp1}] B_{t1}$	\bar{C} F-F \bar{C}
IV m ^c	$[a_{bp1} a_{tp1}] [a_{tp1} a_{tp2}]$	F-F F-F
IV r	$[a_{bp1} a_{tp1}] C_{tp} B_{t2}$	F-F $\bar{C} \bar{C}$
IV s	$A_1 C_{ts} [a_{ts2} b_t]$	$\bar{C} \bar{C}$ F-F
V b ^c	$B_{b1} [a_{bp1} a_{tp1}] [a_{ts1} b_t]$	\bar{C} F-F F-F
V i	$[a_{bp1} a_{tp1}] C_{ts} [a_{ts2} b_t]$	F-F \bar{C} F-F
V j	$B_{b1} [a_{bp1} a_{tp1}] C_{tp} B_{t2}$	\bar{C} F-F $\bar{C} \bar{C}$
V l	$B_{b1} [a_{bp1} a_{tp1}] [C_{ts} b_t]$	\bar{C} F-F C-F
V n	$B_{b1} [a_{bp1} C_{tp}] [a_{ts2} b_t]$	\bar{C} F-C F-F
V w	$[b_b a_{bs1}] [a_{bp1} a_t b_t]$	F-F F- \bar{F} -F
VI a ^c	$[b_b a_{bs1}] [a_{bp1} a_{tp1}] [a_{ts1} b_t]$	F-F F-F F-F
VI h	$B_{b1} [a_{bp1} a_{tp1}] C_{tp} [a_{ts2} b_t]$	\bar{C} F-F \bar{C} C-F
VI o	$[b_b a_{bs1}] [a_{bp1} C_{tp}] [a_{ts2} b_t]$	F-F F-C F-F

Table 14.4: Morphology classification of equal-mass binary lens light curves for separation $s = 0.7$. Asymmetric morphologies and their time reversals are classed together.

Morphology class	Iso-maxima regions
\bar{C}	I a, b
C-C	II a
F-F	II $b^{cp-1}, b^{cs-1}, d^c-1, e^c$
$\bar{C} \bar{C}$	II c, g, i^p
F-C	II b^c-2, d^c-2
C-F \bar{C}	III a^{cp}
\bar{C} F-F	III $b^{cp}, b^{cs}, d^c, e^c, g^c, i^c, n^c, p^{cs}, r$
F- \bar{F} -F	III f^c ,
$\bar{C} \bar{C} \bar{C}$	III o, s
\bar{C} F-F \bar{C}	IV $a^c, c^c, f^{cs}, g^c, l^c$
F-F F-F	IV h^c-1, m^c
F- \bar{F} -F \bar{C}	IV t^c
F-F $\bar{C} \bar{C}$	IV r, s
F-F F-F \bar{C}	V b^c
\bar{C} F-F $\bar{C} \bar{C}$	V j
\bar{C} F-C F-F	V n
F-F \bar{C} F-F	V i
F-F F-F F-F	VI a^c
F-F F-C F-F	VI o
\bar{C} F-F \bar{C} F-F	VI h

14.3 Angular lens separation $s = 0.85$

Figure 14.3: Iso-maxima regions. $s = 0.85$.

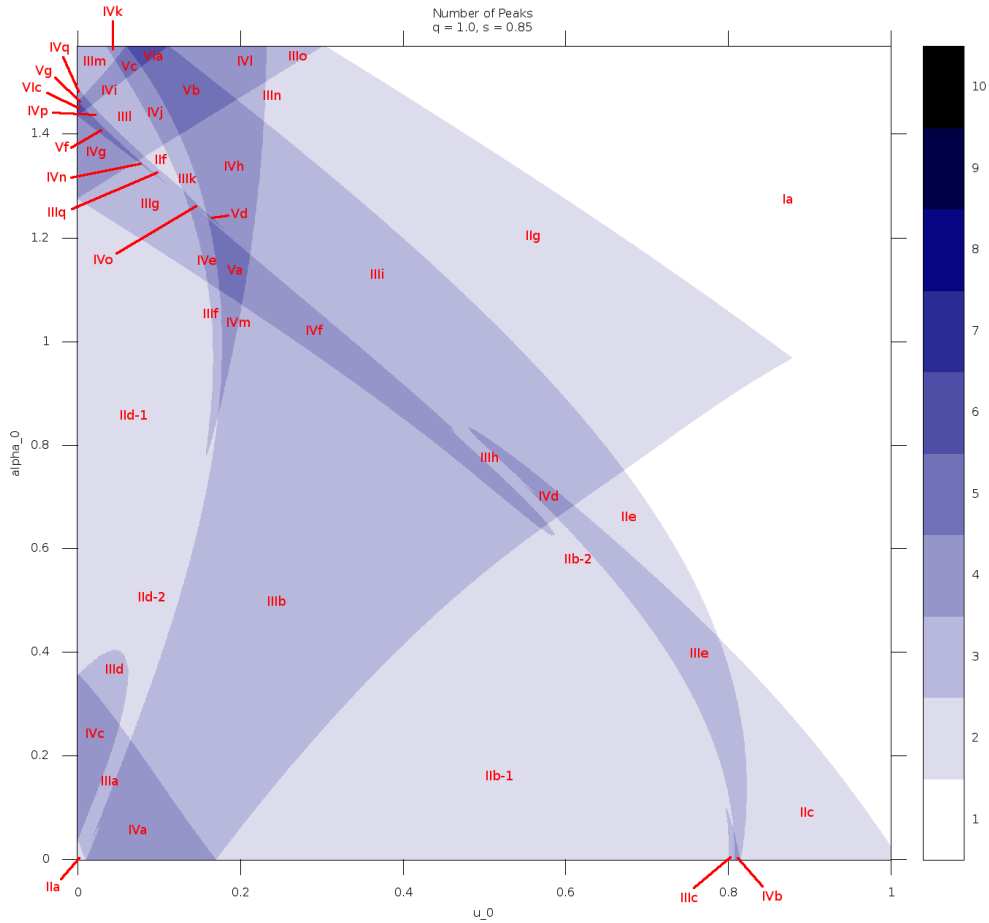


Table 14.5: Caustic feature sequences for iso-maxima plot in Figure 14.3 ($q = 1.0, s = 0.85$).

Iso-maxima region	Caustic feature sequence	Morphology class
Ia	Paczynski peak	\bar{C}
II a	$[A_1A_2]$	C-C
II b-1	$[a_{t1}a_{t2}]$	F-F
II b-2	$[a_{t1}B_{t2}]$	F-C
II c	$B_{t1}B_{t2}$	$\bar{C} \bar{C}$
II d-1	$[a_{b1}a_{t2}]$	F-F
II d-2	$[A_1a_{t2}]$	C-F
II e	$[a_{t1}b_t]$	F-F

Continued on next page.

Table 14.5: Continued. ($q = 1.0, s = 0.85$)

Iso-maxima region	Caustic feature sequence	Morphology class
II f	$[a_{b_1}b_t]$	F-F
II g	$A_1B_{t_1}$	$\bar{C} \bar{C}$
III a	$[A_1a_{t_2}]A_2$	C-F \bar{C}
III b	$A_1[a_{t_1}a_{t_2}]$	\bar{C} F-F
III c	$[a_{t_1}b_t a_{t_2}]$	F- \bar{F} -F
III d	$A_1[a_{b_1}a_{t_2}]$	\bar{C} F-F
III e	$[a_{t_1}b_t]B_{t_2}$	F-F \bar{C}
III f	$[a_{b_1}a_{t_1}a_{t_2}]$	F- \bar{F} -F
III g	$[a_{b_1}a_{t_2}]B_{t_2}$	F-F \bar{C}
III h	$A_1[a_{t_1}B_{t_2}]$	\bar{C} F-C
III i	$A_1[a_{t_1}b_t]$	\bar{C} F-F
III k	$[a_{b_1}a_{t_1}b_t]$	F- \bar{F} -F
III l	$B_{b_1}[a_{b_1}b_t]$	\bar{C} F-F
III m	$[b_b a_{b_1} b_t]$	F- \bar{F} -F
III n	$[a_{b_1}a_{t_1}]B_{t_1}$	F-F \bar{C}
III o	$B_{b_1}A_1B_{t_1}$	$\bar{C} \bar{C} \bar{C}$
III p	$[a_{t_1}a_{t_2}]B_{t_2}$	F-F \bar{C}
III q	$[a_{b_1}a_{t_2}b_t]$	F- \bar{F} -F
IV a	$A_1[a_{t_1}a_{t_2}]A_2$	\bar{C} F-F \bar{C}
IV b	$[a_{t_1}b_t][b_t a_{t_2}]$	F-F F-F
IV c	$A_1[a_{b_1}a_{t_2}]A_2$	\bar{C} F-F \bar{C}
IV d	$A_1[a_{t_1}b_t]B_{t_2}$	\bar{C} F-F \bar{C}
IV e	$[a_{b_1}a_{t_1}a_{t_2}]B_{t_2}$	F- \bar{F} -F \bar{C}
IV f	$A_1[a_{t_1}a_{t_2}]B_{t_2}$	\bar{C} F-F \bar{C}
IV g	$B_{b_1}[a_{b_1}a_{t_2}]B_{t_2}$	\bar{C} F-F \bar{C}
IV h	$[a_{b_1}a_{t_1}][a_{t_1}b_t]$	F-F F-F
IV i	$[b_b a_{b_1}][a_{b_1}b_t]$	F-F F-F
IV j	$B_{b_1}[a_{b_1}a_{t_1}b_t]$	\bar{C} F- \bar{F} -F
IV k	$[b_b a_{b_1}a_{t_1}b_t]$	F- \bar{F} - \bar{F} -F
IV l	$B_{b_1}[a_{b_1}a_{t_1}]B_{t_1}$	\bar{C} F-F \bar{C}
IV m	$[a_{b_1}a_{t_1}][a_{t_1}a_{t_2}]$	F-F F-F
IV n	$[a_{b_1}a_{t_2}][a_{t_2}b_t]$	F-F F-F
IV o	$[a_{b_1}a_{t_1}a_{t_2}b_t]$	F- \bar{F} - \bar{F} -F
IV p	$B_{b_1}[a_{b_1}a_{t_2}b_t]$	\bar{C} F- \bar{F} -F
IV q	$[b_b a_{b_1}a_{t_2}b_t]$	F- \bar{F} - \bar{F} -F
V a	$[a_{b_1}a_{t_1}][a_{t_1}a_{t_2}]B_{t_2}$	F-F F-F \bar{C}
V b	$B_{b_1}[a_{b_1}a_{t_1}][a_{t_1}b_t]$	\bar{C} F-F F-F
V c	$[b_b a_{b_1}][a_{b_1}a_{t_1}b_t]$	F-F F- \bar{F} -F
V d	$[a_{b_1}a_{t_1}][a_{t_1}a_{t_2}b_t]$	F-F F- \bar{F} -F
V f	$B_{b_1}[a_{b_1}a_{t_2}][a_{t_2}b_t]$	\bar{C} F-F F-F

Continued on next page.

Table 14.5: Continued. ($q = 1.0, s = 0.85$)

Iso-maxima region	Caustic feature sequence	Morphology class
V g	$[b_b a_{b1}][a_{b1} a_{t2} b_t]$	F-F F- \bar{F} -F
VI a	$[b_b a_{b1}][a_{b1} a_{t1}][a_{t1} b_t]$	F-F F-F F-F
VI c	$[b_b a_{b1}][a_{b1} a_{t2}][a_{t2} b_t]$	F-F F-F F-F

Table 14.6: Morphology classification of equal-mass binary lens light curves for separation $s = 0.85$. Asymmetric morphologies and their time reversals are classed together.

Morphology class	Iso-maxima regions
\bar{C}	I a
C-C	II a
F-F	II b-1, d-1, e, f
F-C	II b-2, d-2
$\bar{C} \bar{C}$	II c, g
C-F \bar{C}	III a, h
\bar{C} F-F	III b, d, e, g, i, l, n, p
F- \bar{F} -F	III c, f, k, m, q
$\bar{C} \bar{C} \bar{C}$	III o
\bar{C} F-F \bar{C}	IV a, c, d, f, g, l
F-F F-F	IV b, h, i, m, n
F- \bar{F} -F \bar{C}	IV e, j, p
F- \bar{F} - \bar{F} -F	IV k, o, q
F-F F-F \bar{C}	V a, b, f
F-F F- \bar{F} -F	V c, d, g
F-F F-F F-F	VI a, c

14.4 Angular lens separation $s = 1.0$

Figure 14.4: $s = 1.0$. Iso-maxima regions of the first quadrant of the u_0, α parameter space.

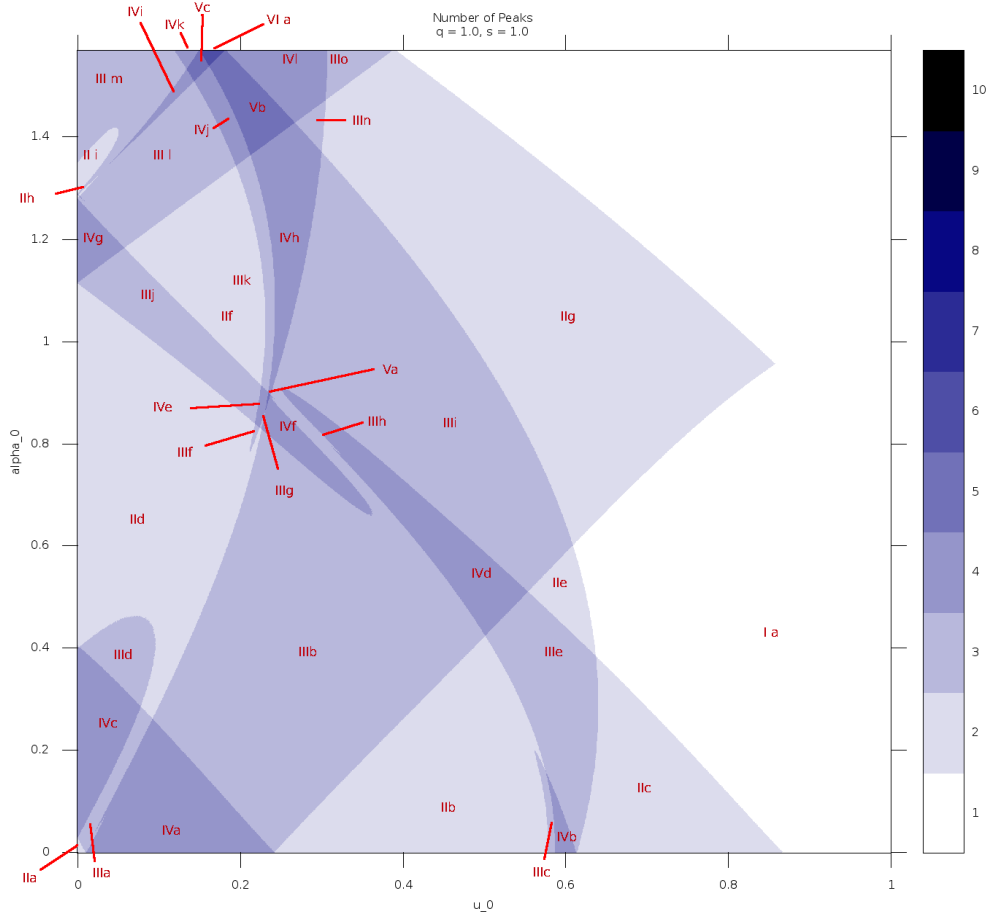


Table 14.7: Caustic feature sequences for iso-maxima plot in Figure 14.4 ($q = 1.0, s = 1.0$). The iso-maxima region labels used here are used throughout the different separation cases, i.e. a region that is labelled here will reappear under the same designation, if it also occurs at a different separation.

Iso-maxima region	Caustic feature sequence	Morphology class
I a	Paczynski peak (or single cusp grazings)	\bar{C}
II a	$[A_1 A_2]$	C-C
II b	$[a_{t1} a_{t2}]$	F-F
II c	$B_{t1} B_{t2}$	C-C
II d	$[a_{b1} a_{t2}]$	F-F

Continued on next page.

Table 14.7: Continued. ($q = 1.0, s = 1.0$)

Iso-maxima region	Caustic feature sequence	Morphology class
II e	$[a_{t1}b_t]$	F-F
II f	$[a_{b1}b_t]$	F-F
II g	A_1B_{t1}	C-C
II h	$[b_b b_t]$	F-F
II i	$[b_b b_t]$	F-F
III a	$[A_1a_{t2}]A_2$	C-F \bar{C}
III b	$A_1[a_{t1}a_{t2}]$	\bar{C} F-F
III c	$[a_{t1}b_t a_{t2}]$	F-F-F
III d	$A_1[a_{b1}a_{t2}]$	\bar{C} F-F
III e	$[a_{t1}b_t]B_{t2}$	F-F \bar{C}
III f	$[a_{b1}a_{t1}a_{t2}]$	F-F-F
III g	$[a_{b1}a_{t2}]B_{t2}$	F-F-C
III h	$A_1[a_{t1}B_{t2}]$	\bar{C} F-C
III i	$A_1[a_{t1}b_t]$	\bar{C} F-F
III j	$[a_{b1}a_{t2}]B_{t2}$	F-F \bar{C}
III k	$[a_{b1}a_{t1}b_t]$	F-F-F
III l	$B_{b1}[a_{b1}b_t]$	\bar{C} F-F
III m	$[b_b a_{b1}b_t]$	F-F-F
III n	$[a_{b1}a_{t1}]B_{t1}$	F-F \bar{C}
III o	$B_{b1}A_1B_1$	\bar{C} \bar{C} \bar{C}
IV a	$A_1[a_{t1}a_{t2}]A_2$	\bar{C} F-F \bar{C}
IV b	$[a_{t1}b_t][b_t a_{t2}]$	F-F F-F
IV c	$A_1[a_{b1}a_{t2}]A_2$	\bar{C} F-F \bar{C}
IV d	$A_1[a_{t1}b_t]B_{t2}$	\bar{C} F-F \bar{C}
IV e	$[a_{b1}a_{t1}a_{t2}]B_{t2}$	F-F-F \bar{C}
IV f	$A_1[a_{t1}a_{t2}]B_{t2}$	\bar{C} F-F \bar{C}
IV g	$B_{b1}[a_{b1}a_{t2}]B_{t2}$	\bar{C} F-F \bar{C}
IV h	$[a_{b1}a_{t1}][a_{t1}b_t]$	F-F F-F
IV i	$[b_b a_{b1}][a_{b1}b_t]$	F-F F-F
IV j	$B_{b1}[a_{b1}a_{t1}b_t]$	\bar{C} F-F-F
IV k	$[b_b a_{b1}a_{t1}b_t]$	F-F-F-F
IV l	$B_{b1}[a_{b1}a_{t1}]B_{t1}$	\bar{C} F-F-F
V a	$[a_{b1}a_{t1}][a_{t1}a_{t2}]B_{t2}$	F-F F-F \bar{C}
V b	$B_{b1}[a_{b1}a_{t1}][a_{t1}b_t]$	\bar{C} F-F F-F
V c	$[b_b a_{b1}][a_{b1}a_{t1}b_t]$	F-F F-F-F
VI a	$[b_b a_{b1}][a_{b1}a_{t1}][a_{t1}b_t]$	F-F F-F F-F

Table 14.8: Morphology classification of equal-mass binary lens light curves in the intermediate separation case ($s = 1.0$). Asymmetric morphologies and their time reversals are classed together.

Morphology class	Iso-maxima regions
\bar{C}	I
F-F $\bar{C}\bar{C}$ C-C	II b, d, e, f, h, i II c, g II a
\bar{C} F-F F- \bar{F} -F C-F \bar{C} $\bar{C}\bar{C}\bar{C}$	III b, d, g, i, j, l, n III c, f, k, m III a, h III o
\bar{C} F-F \bar{C} F-F F-F F- \bar{F} -F \bar{C} F- \bar{F} - \bar{F} -F	IV a, c, d, f, g, l IV b, h, i IV e, j IV k
F-F F-F \bar{C} F-F F- \bar{F} -F	V a, b V c
F-F F-F F-F	VI

14.5 Angular lens separation $s = 1.5$

Figure 14.5: Iso-maxima regions. $s = 1.50$.

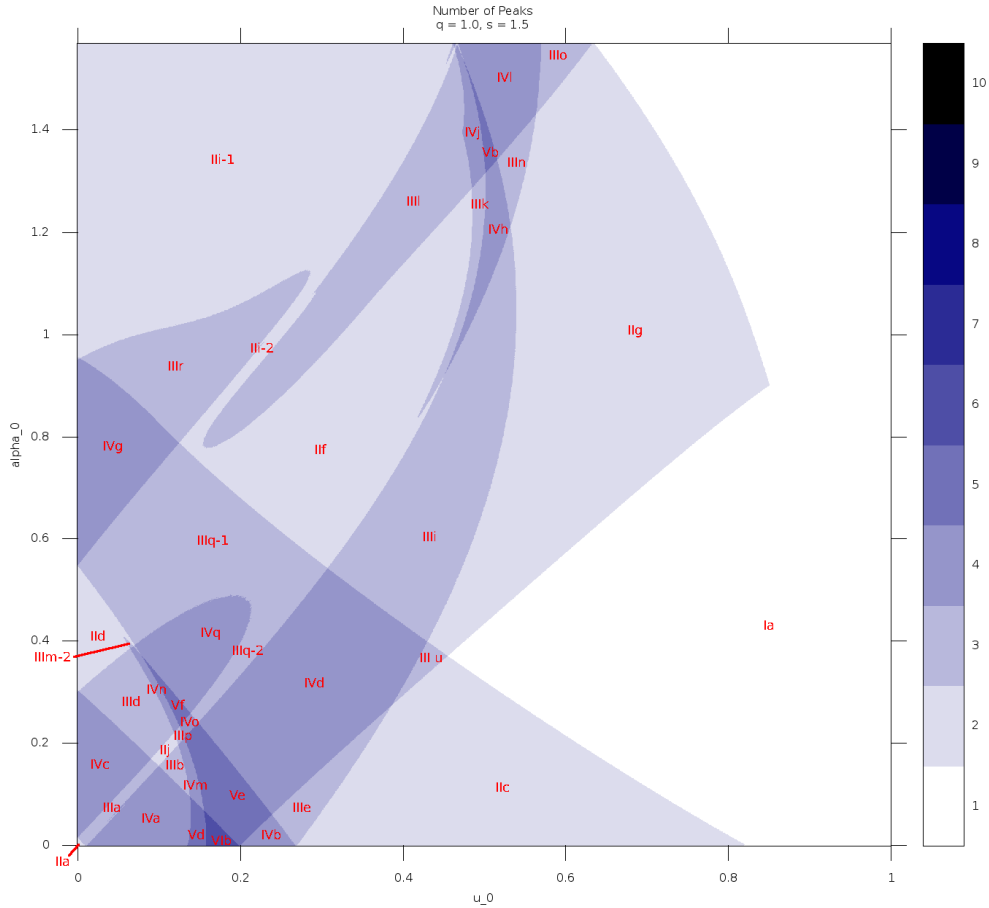


Table 14.9: Caustic feature sequences for iso-maxima plot in Figure 14.5 ($q = 1.0, s = 1.5$).

Iso-maxima region	Caustic feature sequence	Morphology class
I a	Paczynski peak (or cusp grazings)	\bar{C}
II a	$[A_1 A_2]$	C-C
II c	$B_{t1} B_{t2}$	$\bar{C} \bar{C}$
II d-1	$[a_{b1} a_{t2}]$	F-F
II f	$[a_{b1} b_t]$	F-F
II g	$A_1 B_{t1}$	$\bar{C} \bar{C}$
II i-1	$[b_b b_t]$	F-F

Continued on next page.

Table 14.9: Continued. ($q = 1.0, s = 1.5$)

Iso-maxima region	Caustic feature sequence	Morphology class
II i-2	$[B_{b_1}b_t]$	C-F
II j	$[A_1a_{t_2}]$	C-F
III a	$[A_1a_{t_2}]A_2$	C-F \bar{C}
III b	$A_1[a_{t_1}a_{t_2}]$	\bar{C} F-F
III d	$A_1[a_{b_1}a_{t_2}]$	\bar{C} F-F
III e	$[a_{t_1}b_t]B_{t_2}$	\bar{C} F-F
III i	$A_1[a_{t_1}b_t]$	\bar{C} F-F
III k	$[a_{b_1}a_{t_1}b_t]$	F- \bar{F} -F
III l	$B_{b_1}[a_{b_1}b_t]$	\bar{C} F-F
III m	$[b_b a_{b_1} b_t]$	F- \bar{F} -F
III n	$[a_{b_1}a_{t_1}]B_{t_1}$	\bar{C} F-F
III o	$B_{b_1}A_1B_{t_1}$	\bar{C} \bar{C} \bar{C}
III p	$[A_1b_t a_{t_2}]$	C- \bar{F} -F
III q-1	$[a_{b_1}b_t]B_{t_2}$	\bar{C} F-F
III q-2	$[A_1b_t]B_{t_2}$	\bar{C} F-F
III r	$B_{b_1}[b_b b_t]$	\bar{C} F-F
III u	$A_1B_{t_1}B_{t_2}$	\bar{C} \bar{C} \bar{C}
IV a	$A_1[a_{t_1}a_{t_2}]A_2$	\bar{C} F-F \bar{C}
IV b	$[a_{t_1}b_t][b_t a_{t_2}]$	F-F F-F
IV c	$A_1[a_{b_1}a_{t_2}]A_2$	\bar{C} F-F \bar{C}
IV d	$A_1[a_{t_1}b_t]B_{t_2}$	\bar{C} F-F \bar{C}
IV g	$B_{b_1}[b_b b_t]B_{t_2}$	\bar{C} F-F \bar{C}
IV h	$[a_{b_1}a_{t_1}][a_{t_1}b_t]$	F-F F-F
IV j	$B_{b_1}[a_{b_1}a_{t_1}b_t]$	F- \bar{F} -F \bar{C}
IV l	$B_{b_1}[a_{b_1}a_{t_1}]B_{t_1}$	\bar{C} F-F \bar{C}
IV m	$A_1[a_{t_1}b_t a_{t_2}]$	F- \bar{F} -F \bar{C}
IV n	$A_1[a_{b_1}b_t a_{t_2}]$	F- \bar{F} -F \bar{C}
IV o	$[A_1b_t][b_t a_{t_2}]$	C-F F-F
IV q	$A_1[a_{b_1}b_t]B_{t_2}$	\bar{C} F-F \bar{C}
V b	$B_{b_1}[a_{b_1}a_{t_1}][a_{t_1}b_t]$	F-F F-F \bar{C}
V d	$A_1[a_{t_1}b_t a_{t_2}]A_2$	\bar{C} F- \bar{F} -F \bar{C}
V e	$A_1[a_{t_1}b_t][b_t a_{t_2}]$	F-F F-F \bar{C}
V f	$A_1[a_{b_1}b_t][b_t a_{t_2}]$	F-F F-F \bar{C}
VI b	$A_1[a_{t_1}b_t][b_t a_{t_2}]A_2$	\bar{C} F-F F-F \bar{C}

Table 14.10: Morphology classification of equal-mass binary lens light curves at separation $s = 1.5$. Asymmetric morphologies and their time reversals are classed together.

Morphology class	Iso-maxima regions
\bar{C}	I a
F-F	II d, f, i-1
$\bar{C} \bar{C}$	II c, g
C-C	II a
C-F	II i-2, j
\bar{C} F-F	III b, d, e, i, l, n, q-1, q-2, r
F- \bar{F} -F	III k, m
C-F \bar{C}	III a
$\bar{C} \bar{C} \bar{C}$	III o, u
C- \bar{F} -F	III p
\bar{C} F-F \bar{C}	IV a, c, d, g, l, q
F-F F-F	IV b, h
F- \bar{F} -F \bar{C}	IV j, m, n
C-F F-F	IV o
F-F F-F \bar{C}	V b, e, f
\bar{C} F- \bar{F} -F \bar{C}	V d
\bar{C} F-F F-F \bar{C}	VI b

14.6 Angular lens separation $s = 2.05$

Figure 14.6: Iso-maxima regions. $s = 2.05$.

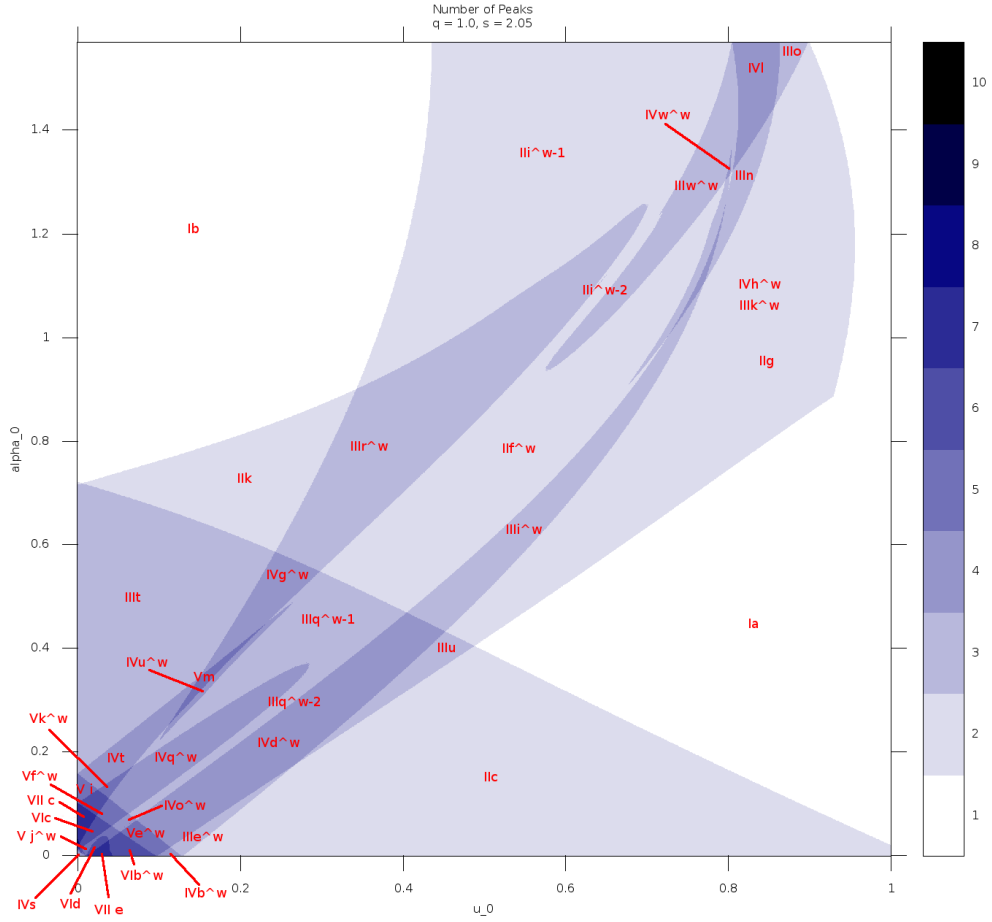


Table 14.11: Caustic feature sequences for iso-maxima plot in Figure 14.6 ($q = 1.0, s = 2.05$).

Iso-maxima region	Caustic feature sequence	Morphology class
I a	outside caustics	\bar{C}
I b	between caustics	\bar{C}
II c	$B_{t1}B_{t2}$	$\bar{C} \bar{C}$
II f ^w	$[a_{b1}b_{t1}]$	F-F
II g	A_1B_{t1}	$\bar{C} \bar{C}$
II i ^w -1	$[b_{b1}b_{t1}]$	F-F
II i ^w -2	$[B_{b1}b_{t1}]$	C-F
II k	$B_{b1}D_1$	$\bar{C} \bar{C}$

Continued on next page.

Table 14.11: Continued. ($q = 1.0, s = 2.05$)

Iso-maxima region	Caustic feature sequence	Morphology class
III e ^w	$[a_{t_1}b_{t_1}]B_{t_2}$	F-F \bar{C}
III i ^w	$A_1[a_{t_1}b_{t_1}]$	\bar{C} F-F
III k ^w	$[a_{b_1}a_{t_1}b_{t_1}]$	F- \bar{F} -F
III n	$[a_{b_1}a_{t_1}]B_{t_1}$	F-F \bar{C}
III o	$B_{b_1}A_1B_{t_1}$	\bar{C} \bar{C} \bar{C}
III q ^w -1	$[a_{b_1}b_{t_1}]B_{t_2}$	F-F \bar{C}
III q ^w -2	$[A_1b_{t_1}]B_{t_2}$	C-F \bar{C}
III r ^w	$B_{b_1}[b_{b_1}b_{t_1}]$	\bar{C} F-F
III t	$B_{b_1}D_1B_{t_2}$	\bar{C} \bar{C} \bar{C}
III u	$A_1B_{t_1}B_{t_2}$	\bar{C} \bar{C} \bar{C}
III w ^w	$A_1[a_{b_1}b_{t_1}]$	\bar{C} F-F
IV b ^w	$[a_{t_1}b_{t_1}][b_{t_2}a_{t_2}]$	F-F F-F
IV d ^w	$A_1[a_{t_1}b_{t_1}]B_{t_2}$	\bar{C} F-F \bar{C}
IV g ^w	$B_{b_1}[b_{b_1}b_{t_1}]B_{t_2}$	\bar{C} F-F \bar{C}
IV h ^w	$[a_{b_1}a_{t_1}][a_{t_1}b_{t_1}]$	F-F F-F
IV l	$B_{b_1}[a_{b_1}a_{t_1}]B_{t_1}$	\bar{C} F-F \bar{C}
IV o ^w	$[A_1b_{t_1}][b_{t_2}a_{t_2}]$	C-F F-F
IV q ^w	$A_1[a_{b_1}b_{t_1}]B_{t_2}$	\bar{C} F-F \bar{C}
IV s	$[A_1D_1][D_2A_2]$	C-C C-C
IV t	$[a_{b_1}b_{b_1}]D_1B_{t_2}$	F-F \bar{C} \bar{C}
IV u ^w	$[a_{b_1}b_{b_1}b_{t_1}]B_{t_2}$	F- \bar{F} -F \bar{C}
IV w ^w	$A_1[a_{b_1}a_{t_1}b_{t_1}]$	\bar{C} F- \bar{F} -F
V e ^w	$A_1[a_{t_1}b_{t_1}][b_{t_2}a_{t_2}]$	\bar{C} F-F F-F
V f ^w	$A_1[a_{b_1}b_{t_1}][b_{t_2}a_{t_2}]$	\bar{C} F-F F-F
V i	$[a_{b_1}b_{b_1}]D[b_{t_2}a_{t_2}]$	F-F \bar{C} F-F
V j ^w	$[A_1b_{t_1}][b_{t_2}a_{t_2}]A_2$	C-F F-F \bar{C}
V k ^w	$A_1[a_{b_1}b_{b_1}b_{t_1}]B_{t_2}$	\bar{C} F- \bar{F} -F \bar{C}
V m	$[a_{b_1}b_{b_1}][b_{b_1}b_{t_1}]D_1$	F-F F-F \bar{C}
VI b ^w	$A_1[a_{t_1}b_{t_1}][b_{t_2}a_{t_2}]A_2$	\bar{C} F-F F-F \bar{C}
VI c	$A_1[a_{b_1}b_{t_1}][b_{t_2}a_{t_2}]A_2$	\bar{C} F-F F-F \bar{C}
VI d	$[A_1b_{t_1}]D_1[b_{t_2}a_{t_2}]A_2$	C-F \bar{C} F-F \bar{C}
VI e	$A_1[a_{b_1}b_{b_1}]D_1[b_{t_2}a_{t_2}]$	\bar{C} F-F \bar{C} F-F
VII c	$A_1[a_{b_1}b_{b_1}]D_1[b_{t_2}a_{t_2}]A_2$	\bar{C} F-F \bar{C} F-F \bar{C}
VII e	$A_1[a_{t_1}b_{t_1}]D_1[b_{t_2}a_{t_2}]A_2$	\bar{C} F-F \bar{C} F-F \bar{C}

Table 14.12: Morphology classification of equal-mass binary lens light curves for the separation $s = 2.05$. Asymmetric morphologies and their time reversals are classed together.

Morphology class	Iso-maxima regions
\bar{C}	I a, b
F-F	II i^w-1, f^w
$\bar{C}\bar{C}$	II c, g, k
C-F	II i^w-2
$\bar{C}F-F$	III $i^w, e^w, n, q^w-1, r^w, w^w$
$F-\bar{F}-F$	III h, j
C-F \bar{C}	III q^w-2
$\bar{C}\bar{C}\bar{C}$	III o, t, u
$\bar{C}F-F\bar{C}$	IV d^w, g^w, l, q^w
F-F F-F	IV b^w, h^w
$F-\bar{F}-F\bar{C}$	IV u^w, w^w
C-F F-F	IV o^w
C-C C-C	IV s
F-F $\bar{C}\bar{C}$	IV t
F-F F-F \bar{C}	V e^w, f^w, m
$\bar{C}F-\bar{F}-F\bar{C}$	V k^w
F-F $\bar{C}F-F$	V i
$\bar{C}F-FF-C$	V j^w
$\bar{C}F-FF-F\bar{C}$	VI b^w, c
C-F $\bar{C}F-F\bar{C}$	VI d
$\bar{C}F-F\bar{C}F-F$	VI e
$\bar{C}F-F\bar{C}F-F\bar{C}$	VII c, e

14.7 Angular lens separation $s = 2.5$

Figure 14.7: Iso-maxima regions. $s = 2.50$.

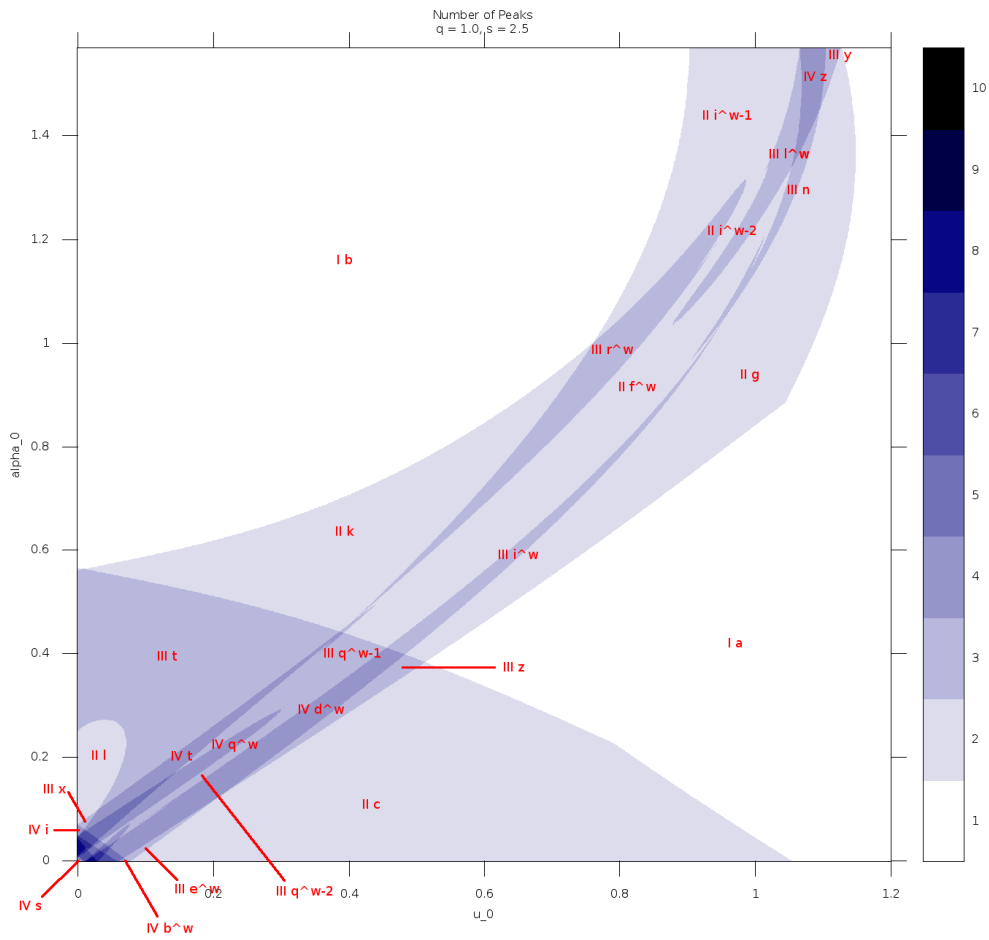


Table 14.13: Caustic feature sequences for iso-maxima plot in Figures 14.7 and 14.8 ($q = 1.0, s = 2.5$).

Iso-maxima region	Caustic feature sequence	Morphology class
I a	outside caustics	\bar{C}
I b	between caustics	\bar{C}
II c	$B_{t1}B_{t2}$	$\bar{C} \bar{C}$
II f ^w	$[a_{b1}b_{t1}]$	F-F
II g	A_1B_{t1}	$\bar{C} \bar{C}$
II i ^w -1	$[b_{b1}b_{t1}]$	F-F

Continued on next page.

Table 14.13: Continued. ($q = 1.0, s = 2.5$)

Iso-maxima region	Caustic feature sequence	Morphology class
II k	$B_{b_1}D_1$	$\bar{C} \bar{C}$
II l	$B_{b_1}B_{t_2}$	$\bar{C} \bar{C}$
III e ^w	$[a_{t_1}b_{t_1}]B_{t_2}$	F-F \bar{C}
III i ^w	$A_1[a_{t_1}b_{t_1}]$	\bar{C} F-F
III k ^w	$[a_{b_1}a_{t_1}b_{t_1}]$	F- \bar{F} -F
III l ^w	$B_{b_1}[a_{b_1}b_{t_1}]$	\bar{C} F-F
III n	$[a_{b_1}a_{t_1}]B_{t_1}$	F-F \bar{C}
III q ^w -2	$[A_1b_{t_1}]B_{t_2}$	C-F \bar{C}
III q ^w -1	$[a_{b_1}b_{t_1}]B_{t_2}$	F-F \bar{C}
III r ^w	$B_{b_1}[b_{b_1}b_{t_1}]$	\bar{C} F-F
III t	$B_{b_1}D_1B_{t_2}$	$\bar{C} \bar{C} \bar{C}$
III x	$[a_{b_1}b_{b_1}]B_{t_2}$	F-F \bar{C}
III y	$B_{b_1}A_1B_{t_2}$	$\bar{C} \bar{C} \bar{C}$
III z	$A_1B_{t_1}B_{t_2}$	$\bar{C} \bar{C} \bar{C}$
IV b ^w	$[a_{t_1}b_{t_1}][b_{t_2}a_{t_2}]$	F-F F-F
IV d ^w	$A_1[a_{t_1}b_{t_1}]B_{t_2}$	\bar{C} F-F \bar{C}
IV h ^w	$[a_{b_1}a_{t_1}][a_{t_1}b_{t_1}]$	F-F F-F
IV q ^w	$A_1[a_{b_1}b_{t_1}]B_{t_2}$	\bar{C} F-F \bar{C}
IV s	$[A_1D_1][D_2A_2]$	C-C C-C
IV t	$[a_{b_1}b_{b_1}]D_1B_{t_2}$	F-F $\bar{C} \bar{C}$
IV x	$[a_{b_1}b_{b_1}][b_{t_2}a_{t_2}]$	F-F F-F
IV y	$[A_1D_1][D_2A_2]$	C-C C-C
IV z	$B_{b_1}[a_{b_1}at_1]B_{t_1}$	\bar{C} F-F \bar{C}
V e ^w	$A_1[a_{t_1}b_{t_1}][b_{t_2}a_{t_2}]$	\bar{C} F-F F-F
V i	$[a_{b_1}b_{b_1}]D_1[b_{t_2}a_{t_2}]$	F-F \bar{C} F-F
V l	$A_1[a_{b_1}b_{b_1}]D_1B_{t_2}$	\bar{C} F-F $\bar{C} \bar{C}$
V n	$A_1[a_{b_1}b_{b_1}][b_{t_1}a_{t_2}]$	\bar{C} F-F F-F
V o	$A_1[a_{b_1}D_1][b_{t_2}a_{t_2}]$	\bar{C} F-C F-F
V p	$[A_1b_{t_1}]D_1[b_{t_2}a_{t_2}]$	C-F \bar{C} F-F
V q	$A_1[a_{t_1}b_{t_1}]D_1B_{t_2}$	\bar{C} F-F $\bar{C} \bar{C}$
V s	$[A_1D_1][b_{t_2}a_{t_2}]A_2$	C-C F-F \bar{C}
VI d	$[A_1b_{t_1}]D_1[b_{t_2}a_{t_2}]A_2$	C-F \bar{C} F-F \bar{C}
VI g	$A_1[a_{t_1}b_{t_1}][b_{t_2}a_{t_2}]A_2$	\bar{C} F-F F-F \bar{C}
VI h	$[A_1D_1]D_2[b_{t_2}a_{t_2}]A_2$	C-C \bar{C} F-F \bar{C}
VI j	$A_1[a_{b_1}b_{b_1}]D_1[b_{t_2}a_{t_2}]$	\bar{C} F-F \bar{C} F-F
VI k	$A_1[a_{b_1}D_1][b_{t_2}a_{t_2}]A_2$	\bar{C} F-C F-F \bar{C}
VI m	$A_1[a_{t_1}b_{t_1}]D_1[b_{t_2}a_{t_2}]$	\bar{C} F-F \bar{C} F-F
VII a	$A_1[a_{b_1}D_1]D_2[b_{t_2}a_{t_2}]A_2$	\bar{C} F-C \bar{C} F-F \bar{C}
VII b	$[A_1b_{t_1}]D_1D_2[b_{t_2}a_{t_2}]A_2$	C-F $\bar{C} \bar{C}$ F-F \bar{C}

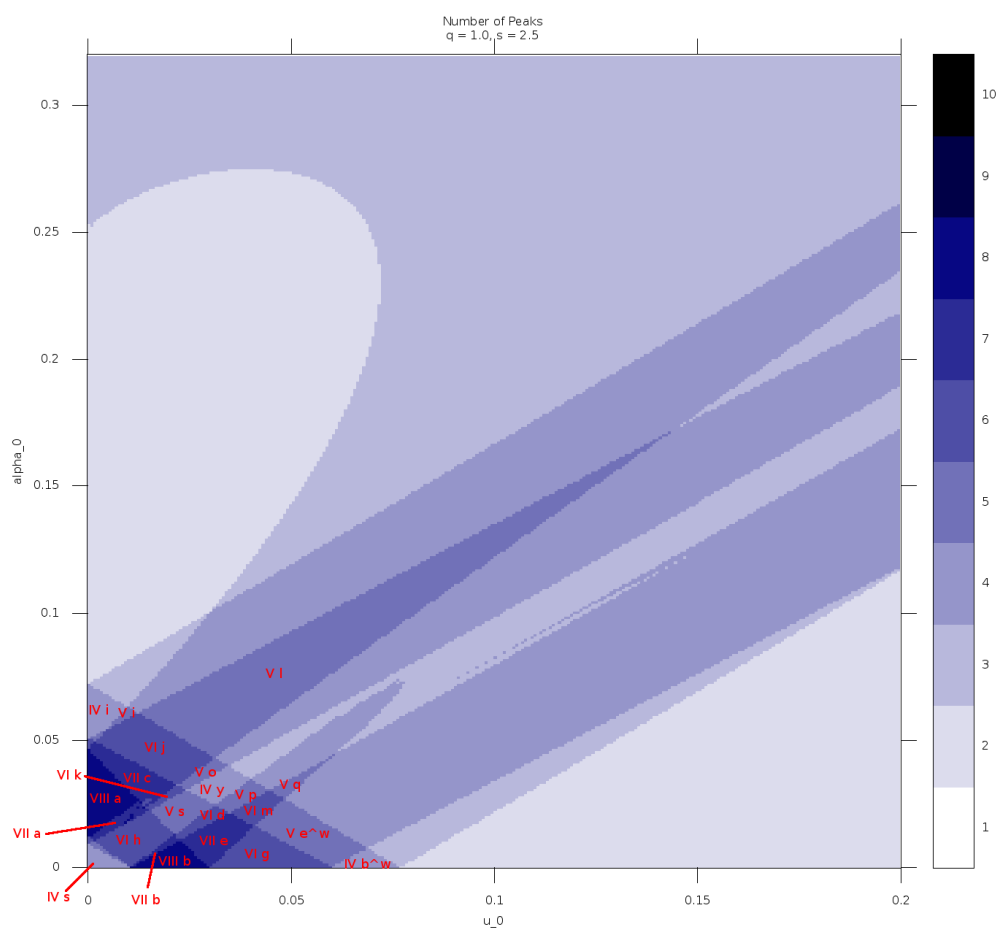
Continued on next page.

Table 14.13: Continued. ($q = 1.0$, $s = 2.5$)

Iso-maxima region	Caustic feature sequence	Morphology class
VII c	$A_1[a_{b_1}b_{b_1}]D_1[b_{t_2}a_{t_2}]A_2$	\bar{C} F-F \bar{C} F-F \bar{C}
VII e	$A_1[a_{t_1}b_{t_1}]D_1[b_{t_2}a_{t_2}]A_2$	\bar{C} F-F \bar{C} F-F \bar{C}
VIII a	$A_1[a_{b_1}b_{b_1}]D_1D_2[b_{t_2}a_{t_2}]A_2$	\bar{C} F-F \bar{C} \bar{C} F-F \bar{C}
VIII b	$A_1[a_{t_1}b_{t_1}]D_1D_2[b_{t_2}a_{t_2}]A_2$	\bar{C} F-F \bar{C} \bar{C} F-F \bar{C}

Table 14.14: Morphology classification of equal-mass binary lens light curves in the case $s = 2.5$. Asymmetric morphologies and their time reversals are classed together.

Morphology class	Iso-maxima regions
\bar{C}	I a, b
\bar{C} \bar{C} F-F	II l, c, j, g II i^w-1 , f^w
C-F \bar{C} \bar{C} \bar{C} \bar{C} F-F \bar{C} F- \bar{F} -F	III q^w-2 III t, y, z III e^w , i^w , l^w , n, q^w-1 , r^w , x III k^w
C-C C-C F-F F-F F-F \bar{C} \bar{C} \bar{C} F-F \bar{C}	IV s, y IV b^w , h^w , x IV t IV d^w , q^w , z
\bar{C} F-F F-F F-F \bar{C} F-F \bar{C} F-C F-F C-F \bar{C} F-F \bar{C} F-F \bar{C} \bar{C} C-C F-F \bar{C}	V e^w , n V i V o V p V l, q V s
C-C \bar{C} F-F \bar{C} \bar{C} F-F F-F \bar{C} \bar{C} F-F \bar{C} F-F \bar{C} F-C F-F \bar{C} C-F \bar{C} F-F \bar{C}	VI h VI g VI j, m VI k VI d
\bar{C} F-C \bar{C} F-F \bar{C} C-F \bar{C} \bar{C} F-F \bar{C} \bar{C} F-F \bar{C} F-F \bar{C}	VII a VII b VII c, e
\bar{C} F-F \bar{C} \bar{C} F-F \bar{C}	VIII a, b

Figure 14.8: Iso-maxima regions (zoom). $s = 2.50$.

Bibliography

- Afonso, C., Albert, J., Andersen, J., Ansari, R., Aubourg, E., Bareyre, P., Beaulieu, J., Blanc, G., Charlot, X., Couchot, E., Coutures, C., Ferlet, R., Fouque, P., Glicenstein, J., Goldman, B., Gould, A., Graff, D., Gros, M., Haissinski, J., Hamadache, C. et al. (2003) Limits on Galactic dark matter with 5 years of EROS SMC data. *Astronomy & Astrophysics*, 400, 951
- Albrow, M.D., Beaulieu, J.P., Caldwell, J.A.R., Depoy, D.L., Dominik, M., Gaudi, B.S., Gould, A., Greenhill, J., Hill, K., Kane, S., Martin, R., Menzies, J., Naber, R.M., Pogge, R.W., Pollard, K.R., Sackett, P.D., Sahu, K.C., Vermaak, P., Watson, R., Williams, A. et al. (1999) A Complete Set of Solutions for Caustic Crossing Binary Microlensing Events. *ApJ*, 522, 1022
- Albrow, M., Beaulieu, J.P., Birch, P., Caldwell, J.A.R., Kane, S., Martin, R., Menzies, J., Naber, R.M., Pel, J.W., Pollard, K., Sackett, P.D., Sahu, K.C., Vreeswijk, P., Williams, A. & Zwaan, M.A.T.P.C. (1998) The 1995 pilot campaign of PLANET: searching for microlensing anomalies through precise, rapid, round-the-clock monitoring. *The Astrophysical Journal*, 509, 687
- Alcock, C., Allen, W.H., Allsman, R.A., Alves, D., Axelrod, T.S., Banks, T.S., Beaulieu, S.F., Becker, A.C., Becker, R.H., Bennett, D.P., Bond, I.A., Carter, B.S., Cook, K.H., Dodd, R.J., Freeman, K.C., Gregg, M.D., Griest, K., Hearnshaw, J.B., Heller, A., Honda, M. et al. (1997) MACHO Alert 95-30: First Real-Time Observation of Extended Source Effects in Gravitational Microlensing. *ApJ*, 491, 436
- Alcock, C., Allsman, R.A., Alves, D., Axelrod, T.S., Becker, A.C., Bennett, D.P., Cook, K.H., Drake, A.J., Freeman, K.C., Griest, K., Lehner, M.J., Marshall, S.L., Minniti, D., Peterson, B.A., Pratt, M.R., Quinn, P.J., Stubbs, C.W., Sutherland, W., Tomaney, A., Vandehei, T. et al. (1999) Difference Image Analysis of Galactic Microlensing. I. Data Analysis. *ApJ*, 521, 602
- Alcock, C., Allsman, R.A., Alves, D., Axelrod, T.S., Bennett, D.P., Cook, K.H., Freeman, K.C., Griest, K., Guern, J., Lehner, M.J., Marshall, S.L., Peterson, B.A., Pratt, M.R., Quinn, P.J., Rodgers, A.W., Stubbs, C.W. & Sutherland, W. (1995) First Observation of Parallax in a Gravitational Microlensing Event. *ApJL*, 454,
- Alcock, C., Allsman, R.A., Alves, D.R., Axelrod, T.S., Becker, A.C., Bennett, D.P., Cook, K.H., Drake, A.J., Freeman, K.C., Geha, M., Griest, K., Keller, S.C., Lehner, M.J., Marshall,

- S.L., Minniti, D., Nelson, C.A., Peterson, B.A., Popowski, P., Pratt, M.R., Quinn, P.J. et al. (2001) Direct detection of a microlens in the Milky Way. *Nature*, 414, 617
- Alcock, C., Akerlof, C.W., Allsman, R.A., Axelrod, T.S., Bennett, D.P., Chan, S., Cook, C.H., Freeman, K.C., Griest, K., Marshall, S.L., Park, H.S., Perlmutter, S., Peterson, B.A., Pratt, M.R., Quinn, P.J., Rodgers, A.W., Stubbs, C.W. & Sutherland, W. (1993) Possible Gravitational Microlensing of a Star in the Large Magellanic Cloud. *Nature*, 365, 621
- An, J.H., Albrow, M.D., Beaulieu, J.P., Caldwell, J.A.R., DePoy, D.L., Dominik, M., Gaudi, B.S., Gould, A., Greenhill, J., Hill, K., Kane, S., Martin, R., Menzies, J., Pogge, R.W., Pollard, K.R., Sackett, P.D., Sahu, K.C., Vermaak, P., Watson, R. & Williams, A. (2002) First Microlens Mass Measurement: PLANET Photometry of EROS BLG-2000-5. *ApJ*, 572, 521
- Aubourg, E., Bareyre, P., Bréhin, S., Gros, M., Lachize-Rey, M., Laurent, B., Lesquoy, E., Magneville, C., Milsztajn, A., Moscoso, L., Queinnec, F., Rich, J., Spiro, M., Vigroux, L., Zylberajch, S., Ansari, R., Cavalier, F., Moniez, M., Beaulieu, J.P., Ferlet, R. et al. (1993) Evidence for Gravitational Microlensing by Dark Objects in the Galactic Halo. *Nature*, 365, 623
- Baade, D., Meisenheimer, K., Iwert, O., Alonso, J., Augusteijn, T., Beletic, J., Bellemann, H., Benesch, W., Böhm, A., Böhnhardt, H., Brewer, J., Deiries, S., Delabre, B., Donaldson, R., Dupuy, C., Franke, P., Gerdes, R., Gilliotte, A., Grimm, B., Haddad, N. et al. (1999) The Wide Field Imager at the 2.2-m MPG/ESO telescope: first views with a 67-million-facette eye. *The Messenger*, 95, 15
- Batista, V., Gould, A.P., Dieters, S., Dong, S., Bond, I., Beaulieu, J.P., Maoz, D., Monard, B., Christie, G.W., McCormick, J., Albrow, M.D., Horne, K., Tsapras, Y., Burgdorf, M.J., Calchi Novati, S., Skottfelt, J., Caldwell, J., Kozłowski, S., Kubas, D., Gaudi, B.S. et al. (2011) MOA-2009-BLG-387Lb: a massive planet orbiting an M dwarf. *A&A*, 529, A102
- Bennett, D.P. (2010) An Efficient Method for Modeling High-magnification Planetary Microlensing Events. *ApJ*, 716, 1408
- Bennett, D.P., Batista, V., Bond, I.A., Bennett, C.S., Suzuki, D., Beaulieu, J.P., Udalski, A., Donatowicz, J., Bozza, V., Abe, F., Botzler, C.S., Freeman, M., Fukunaga, D., Fukui, A., Itow, Y., Koshimoto, N., Ling, C.H., Masuda, K., Matsubara, Y., Muraki, Y. et al. (2014) MOA-2011-BLG-262Lb: A Sub-Earth-Mass Moon Orbiting a Gas Giant Primary or a High Velocity Planetary System in the Galactic Bulge. *ApJ*, 785, 155
- Bennett, D.P., Sumi, T., Bond, I.A., Kamiya, K., Abe, F., Botzler, C.S., Fukui, A., Furu-sawa, K., Itow, Y., Korpela, A.V., Kilmartin, P.M., Ling, C.H., Masuda, K., Matsubara, Y., Miyake, N., Muraki, Y., Ohnishi, K., Rattenbury, N.J., Saito, T., Sullivan, D.J. et al. (2012) Planetary and Other Short Binary Microlensing Events from the MOA Short-event Analysis. *ApJ*, 757, 119

- Bennett, D.P. & Rhie, S.H. (1996) Detecting Earth-Mass Planets with Gravitational Microlensing. *The Astrophysical Journal*, 472, 660
- Bertin, E. & Arnouts, S. (1996) SExtractor: Software for source extraction. *A&AS*, 117, 393
- Bond, I.A., Udalski, A., Jaroszyński, M., Rattenbury, N.J., Paczyński, B., Soszyński, I., Wyrzykowski, L., Szymański, M.K., Kubiak, M., Szewczyk, O., Żebruń, K., Pietrzyński, G., Abe, F., Bennett, D.P., Eguchi, S., Furuta, Y., Hearnshaw, J.B., Kamiya, K., Kilmartin, P.M., Kurata, Y. et al. (2004) OGLE 2003-BLG-235/MOA 2003-BLG-53: A Planetary Microlensing Event. *The Astrophysical Journal*, 606(2), L155
- Boutreux, T. & Gould, A. (1996) Monte Carlo Simulations of MACHO Parallaxes from a Satellite. *ApJ*, 462, 705
- Bozza, V. (2010a) Gravitational lensing by black holes. *General Relativity and Gravitation*, 42, 2269
- Bozza, V., Dominik, M., Rattenbury, N.J., Jørgensen, U.G., Tsapras, Y., Bramich, D.M., Udalski, A., Bond, I.A., Liebig, C., Cassan, A., Fouqué, P., Fukui, A., Hundertmark, M., Shin, I.G., Lee, S.H., Choi, J.Y., Park, S.Y., Gould, A., Allan, A., Mao, S. et al. (2012) OGLE-2008-BLG-510: first automated real-time detection of a weak microlensing anomaly - brown dwarf or stellar binary? *MNRAS*, 424, 902
- Bozza, V. (2001) Trajectories of images in binary microlensing. *Astronomy & Astrophysics*, 374, 13
- Bozza, V. (2010b) Microlensing with an advanced contour integration algorithm: Green's theorem to third order, error control, optimal sampling and limb darkening. *MNRAS*, 1271
- Cassan, A., Kubas, D., Beaulieu, J.P., Dominik, M., Horne, K., Greenhill, J., Wambsganss, J., Menzies, J., Williams, A., Jørgensen, U.G., Udalski, A., Bennett, D.P., Albrow, M.D., Batista, V., Brilliant, S., Caldwell, J.A.R., Cole, A., Coutures, C., Cook, K.H., Dieters, S. et al. (2012) One or more bound planets per Milky Way star from microlensing observations. *Nature*, 481, 167
- Cassan, A. (2008) An alternative parameterisation for binary-lens caustic-crossing events. *A&A*, 491, 587
- Charbonneau, D., Brown, T.M., Latham, D.W. & Mayor, M. (2000) Detection of Planetary Transits Across a Sun-like Star. *ApJL*, 529,
- Daněk, K. & Heyrovský, D. (2011) Critical Curves of Triple Gravitational Lenses. In J. Šafránková & J. Pavlů (Editors) *WDS'11 Proceedings of Contributed Papers: Part III - Physics*, 37–42, Matfyzpress, Prague
- Di Stefano, R. & Perna, R. (1997) Identifying Microlensing by Binaries. *ApJ*, 488, 55

- Dominik, M. (1995) Improved Routines for the Inversion of the Gravitational Lens Equation for a Set of Source Points. *A&AS*, 109, 597
- Dominik, M. (1998) Galactic Microlensing with Rotating Binaries. *Astronomy and Astrophysics*, 329, 361
- Dominik, M. (1999a) Ambiguities in fits of observed binary lens galactic microlensing events. *Astronomy and Astrophysics*, 341, 943
- Dominik, M. (1999b) The binary gravitational lens and its extreme cases. *A&A*, 349, 108
- Dominik, M. (2006) Stochastic distributions of lens and source properties for observed galactic microlensing events. *MNRAS*, 367, 669
- Dominik, M. (2007) Adaptive contouring - an efficient way to calculate microlensing light curves of extended sources. *MNRAS*, 377, 1679
- Dominik, M. (2010) The gravitational bending of light by stars: a continuing story of curiosity, scepticism, surprise, and fascination. *General Relativity and Gravitation*, 1–18, 10.1007/s10714-010-0964-x
- Dominik, M., Albrow, M.D., Beaulieu, J.P., Caldwell, J.A.R., DePoy, D.L., Gaudi, B.S., Gould, A., Greenhill, J., Hill, K., Kane, S., Martin, R., Menzies, J., Naber, R.M., Pel, J.W., Pogge, R.W., Pollard, K.R., Sackett, P.D., Sahu, K.C., Vermaak, P., Watson, R. et al. (2002) The PLANET microlensing follow-up network: results and prospects for the detection of extra-solar planets. *P&SS*, 50, 299
- Dominik, M. & Hirshfeld, A.C. (1996) Evidence for a binary lens in the MACHO LMC No. 1 microlensing event. *A&A*, 313, 841
- Dominik, M., Jørgensen, U.G., Horne, K., Tsapras, Y., Street, R.A., Wyrzykowski, L., Hestman, F.V., Hundertmark, M., Rahvar, S., Wambsganss, J., Scarpetta, G., Bozza, V., Calchi Novati, S., Mancini, L., Masi, G., Teuber, J., Hinse, T.C., Steele, I.A., Burgdorf, M.J. & Kane, S. (2008) Inferring statistics of planet populations by means of automated microlensing searches. *ESA white paper*, arXiv:0808.0004v1
- Dong, S., DePoy, D.L., Gaudi, B.S., Gould, A., Han, C., Park, B.G., Pogge, R.W., Collaboration, M., Udalski, A., Szewczyk, O., Kubiak, M., Szymański, M.K., Pietrzyński, G., Soszyński, I., Wyrzykowski, L., Zeburń, K. & Collaboration, O.G.L.E. (2006) Planetary Detection Efficiency of the Magnification 3000 Microlensing Event OGLE-2004-BLG-343. *ApJ*, 642, 842
- Dong, S., Udalski, A., Gould, A., Reach, W.T., Christie, G.W., Boden, A.F., Bennett, D.P., Fazio, G., Griest, K., Szymański, M.K., Kubiak, M., Soszyński, I., Pietrzyński, G., Szewczyk, O., Wyrzykowski, L., Ulaczyk, K., Wieckowski, T., Paczyński, B., DePoy, D.L., Pogge, R.W. et al. (2007) First Space-Based Microlens Parallax Measurement: Spitzer Observations of OGLE-2005-SMC-001. *ApJ*, 664, 862

- Dyson, F.W., Eddington, A.S. & Davidson, C. (1920) A Determination of the Deflection of Light by the Sun's Gravitational Field, from Observations Made at the Total Eclipse of May 29, 1919. *Royal Society of London Philosophical Transactions Series A*, 220, 291
- Einstein, A. (1916) Die Grundlage der allgemeinen Relativitätstheorie. *Annalen der Physik*, 354, 769
- Einstein, A. (1936) Lens-Like Action of a Star by the Deviation of Light in the Gravitational Field. *Science*, 84, 506
- Erdl, H. & Schneider, P. (1993) Classification of the multiple deflection two point-mass gravitational lens models and application of catastrophe theory in lensing. *Astronomy and Astrophysics*, 268(2), 453
- Gaudi, B.S. (1998) Distinguishing Between Binary-Source and Planetary Microlensing Perturbations. *ApJ*, 506, 533
- Gaudi, B.S. (2010) Exoplanetary Microlensing. *arXiv:1002.0332v2*
- Gaudi, B.S. (2012) Microlensing Surveys for Exoplanets. *ARA&A*, 50, 411
- Gaudi, B.S. & Petters, A.O. (2002) Gravitational Microlensing near Caustics. I. Folds. *ApJ*, 574, 970
- Gaudi, B.S., Bennett, D.P., Udalski, A., Gould, A. et al. (2008) Discovery of a Jupiter/Saturn Analog with Gravitational Microlensing. *Science*, 319, 927
- Gaudi, B.S., Naber, R.M. & Sackett, P.D. (1998) Microlensing by Multiple Planets in High-Magnification Events. *ApJL*, 502, L33
- Gould, A. (1994a) Proper motions of MACHOs. *ApJL*, 421,
- Gould, A. (2013) Geosynchronous Microlens Parallaxes. *ApJL*, 763, L35
- Gould, A. & Horne, K. (2013) Kepler-like Multi-plexing for Mass Production of Microlens Parallaxes. *ApJL*, 779, L28
- Gould, A., Udalski, A., Monard, B., Horne, K., Dong, S., Miyake, N., Sahu, K., Bennett, D.P., Wyrzykowski, .L., Soszyński, I., Szymański, M.K., Kubiak, M., Pietrzyński, G., Szewczyk, O., Ulaczyk, K., Collaboration, O.G.L.E., Allen, W., Christie, G.W., DePoy, D.L., Gaudi, B.S. et al. (2009) The Extreme Microlensing Event OGLE-2007-BLG-224: Terrestrial Parallax Observation of a Thick-Disk Brown Dwarf. *ApJL*, 698,
- Gould, A. & Yee, J.C. (2013) Microlens Terrestrial Parallax Mass Measurements: A Rare Probe of Isolated Brown Dwarfs and Free-floating Planets. *ApJ*, 764, 107
- Gould, A. & Yee, J.C. (2012) Cheap Space-based Microlens Parallaxes for High-magnification Events. *ApJL*, 755, L17

- Gould, A. & Yee, J.C. (2014) Microlens Masses From Astrometry and Parallax in Space-Based Surveys: From Planets to Black Holes. *ApJ*, 784(1), 64
- Gould, A.P. (1994b) MACHO velocities from satellite-based parallaxes. *ApJL*, 421, L75
- Gould, A.P. (2000) A Natural Formalism for Microlensing. *ApJ*, 542, 785
- Gould, A.P., Dong, S., Gaudi, B.S., Udalski, A., Bond, I.A., Greenhill, J., Street, R.A., Dominik, M., Sumi, T., Szymański, M.K., Han, C., Allen, W., Bolt, G., Bos, M., Christie, G.W., DePoy, D.L., Drummond, J., Eastman, J.D., Gal-Yam, A., Higgins, D. et al. (2010) Frequency of Solar-like Systems and of Ice and Gas Giants Beyond the Snow Line from High-magnification Microlensing Events in 2005-2008. *ApJ*, 720, 1073
- Gould, A.P. & Gaucherel, C. (1997) Stokes's Theorem Applied to Microlensing of Finite Sources. *ApJ*, 477, 580
- Gould, A.P. & Loeb, A. (1992) Discovering planetary systems through gravitational microlenses. *The Astrophysical Journal*, 396, 104
- Griest, K. (1991) Galactic microlensing as a method of detecting massive compact halo objects. *ApJ*, 366, 412
- Griest, K. & Hu, W. (1992) Effect of binary sources on the search for massive astrophysical compact halo objects via microlensing. *ApJ*, 397, 362
- Han, C. & Gaudi, B.S. (2008) A Characteristic Planetary Feature in Double-Peaked, High-Magnification Microlensing Events. *ApJ*, 689, 53
- Henry, G.W., Marcy, G.W., Butler, R.P. & Vogt, S.S. (2000) A transiting "51 Peg-like" planet. *ApJL*, 529, L41
- Hundertmark, M., Hessman, F. & Dreizler, S. (2008) An Implementation of the Ray Shooting Method. In *Manchester Microlensing Conference*
- Hwang, K.H., Choi, J.Y., Bond, I.A., Sumi, T., Han, C., Gaudi, B.S., Gould, A., Bozza, V., Beaulieu, J.P., Tsapras, Y., Abe, F., Bennett, D.P., Botzler, C.S., Chote, P., Freeman, M., Fukui, A., Fukunaga, D., Harris, P., Itow, Y., Koshimoto, N. et al. (2013) Interpretation of a Short-term Anomaly in the Gravitational Microlensing Event MOA-2012-BLG-486. *ApJ*, 778, 55
- Irwin, M. & Lewis, J. (2001) INT WFS pipeline processing. *NewAR*, 45, 105
- Jaroszyński, M., Skowron, J., Udalski, A., Kubiak, M., Szymański, M.K., Pietrzyński, G., Soszyński, I., Wyrzykowski, L., Ulaczyk, K. & Poleski, R. (2010) Binary Lenses in OGLE-III EWS Database. Seasons 2006-2008. *AcA*, 60, 197
- Jones, E., Oliphant, T., Peterson, P. et al. (2001-) SciPy: Open source scientific tools for Python

- Kains, N., Street, R.A., Choi, J.Y., Han, C., Udalski, A., Almeida, L.A., Jablonski, F., Tristram, P.J., Jørgensen, U.G., Szymański, M.K., Kubiak, M., Pietrzyński, G., Soszyński, I., Poleski, R., Kozłowski, S., Pietrukowicz, P., Ulaczyk, K., Wyrzykowski, Ł., Skowron, J., Alsubai, K.A. et al. (2013) A giant planet beyond the snow line in microlensing event OGLE-2011-BLG-0251. *A&A*, 552, A70
- Kayser, R., Refsdal, S. & Stabell, R. (1986) Astrophysical applications of gravitational microlensing. *A&A*, 166(1-2), 36
- Keller, H.U., Barbieri, C., Lamy, P., Rickman, H., Rodrigo, R., Wenzel, K.P., Sierks, H., A'Hearn, M.F., Angrilli, F., Angulo, M., Bailey, M.E., Barthol, P., Barucci, M.A., Bertaux, J.L., Bianchini, G., Boit, J.L., Brown, V., Burns, J.A., Büttner, I., Castro, J.M. et al. (2007a) OSIRIS The Scientific Camera System Onboard Rosetta. *SSR*, 128, 433
- Keller, H.U., Küppers, M., Fornasier, S., Gutiérrez, P.J., Hviid, S.F., Jorda, L., Knollenberg, J., Lowry, S.C., Rengel, M., Bertini, I., Cremonese, G., Ip, W.H., Koschny, D., Kramm, R., Kührt, E., Lara, L.M., Sierks, H., Thomas, N., Barbieri, C., Lamy, P. et al. (2007b) Observations of Comet 9P/Tempel 1 around the Deep Impact event by the OSIRIS cameras onboard Rosetta. *Icarus*, 191, 241
- Lang, D., Hogg, D.W., Mierle, K., Blanton, M. & Roweis, S. (2010) Astrometry.net: Blind Astrometric Calibration of Arbitrary Astronomical Images. *AJ*, 139, 1782
- Liebes, S. (1964) Gravitational Lenses. *Physical Review*, 133, 835
- Liebig, C., D'Ago, G., Bozza, V. & Dominik, M. (2014a) Morphology of equal-mass binary microlensing light curves, in preparation
- Liebig, C., Snodgrass, C., Dominik, M., Hundertmark, M., Marnach, S., Grieger, B., Kueppers, M., Conn, B., Sierks, H., Burgdorf, M., Keller, H. U., Udalski, A., Szymański, Michał K., Kubiak, M., Pietrzyński, G., Soszyński, I., Ulaczyk, K., Wyrzykowski, Ł. & Poleski, R. (2014b) Galactic microlensing events observed from the Rosetta spacecraft in 2008, in preparation
- Liebig, C. & Wambsganss, J. (2010) Detectability of extrasolar moons as gravitational microlenses. *A&A*, 520, A68
- Mao, S., Witt, H.J. & An, J.H. (2013) Three-dimensional microlensing. *MNRAS*
- Mao, S. & Di Stefano, R. (1995) Interpretation of gravitational microlensing by binary systems. *ApJ*, 440, 22
- Mao, S. & Paczyński, B. (1991) Gravitational microlensing by double stars and planetary systems. *The Astrophysical Journal*, 374, L37
- Marcy, G.W. & Butler, R.P. (2000) Planets Orbiting Other Suns. *PASP*, 112, 137

- Mayor, M. & Queloz, D. (1995) A Jupiter-Mass Companion to a Solar-Type Star. *Nature*, 378, 355
- Misner, C.W., Thorne, K.S. & Wheeler, J.A. (1973) *Gravitation*. W.H. Freeman and Co., San Francisco
- Miyake, N., Sumi, T., Dong, S., Street, R., Mancini, L., Gould, A., Bennett, D.P., Tsapras, Y., Yee, J.C., Albrow, M.D., Bond, I.A., Fouqué, P., Browne, P., Han, C., Snodgrass, C., Finet, F., Furusawa, K., Harnsøe, K., Allen, W., Hundertmark, M. et al. (2011) A Sub-Saturn Mass Planet, MOA-2009-BLG-319Lb. *ApJ*, 728, 120
- Moffat, A.F.J. (1969) A Theoretical Investigation of Focal Stellar Images in the Photographic Emulsion and Application to Photographic Photometry. *A&A*, 3, 455
- Monet, D.G., Levine, S.E., Canzian, B., Ables, H.D., Bird, A.R., Dahn, C.C., Guetter, H.H., Harris, H.C., Henden, A.A., Leggett, S.K., Levison, H.F., Luginbuhl, C.B., Martini, J., Monet, A.K.B., Munn, J.A., Pier, J.R., Rhodes, A.R., Rieke, B., Sell, S., Stone, R.C. et al. (2003) The USNO-B Catalog. *AJ*, 125, 984
- Muraki, Y., Han, C., Bennett, D.P., Suzuki, D., Monard, L.A.G., Street, R., Jorgensen, U.G., Kundurthy, P., Skowron, J., Becker, A.C., Albrow, M.D., Fouqué, P., Heyrovský, D., Barry, R.K., Beaulieu, J.P., Wellnitz, D.D., Bond, I.A., Sumi, T., Dong, S., Gaudi, B.S. et al. (2011) Discovery and Mass Measurements of a Cold, 10 Earth Mass Planet and Its Host Star. *ApJ*, 741, 22
- Muraki, Y., Sumi, T., Abe, F., Bond, I., Carter, B., Dodd, R., Fujimoto, M., Hearnshaw, J., Honda, M., Jugaku, J., Kabe, S., Kato, Y., Kobayashi, M., Koribalski, B., Kilmartin, P., Masuda, K., Matsubara, Y., Nakamura, T., Noda, S., Pennycook, G. et al. (1999) Search for MACHOS by the MOA Collaboration. *Progress of Theoretical Physics Supplement*, 133, 233
- Night, C., Di Stefano, R. & Schwamb, M. (2008) Beyond Caustic Crossings: Properties of Binary Microlensing Light Curves. *ApJ*, 686, 785
- Paczynski, B. (1986) Gravitational microlensing by the Galactic halo. *ApJ*, 304, 1
- Paczynski, B. (1991) Gravitational microlensing of the Galactic bulge stars. *ApJL*, 371, L63
- Paczynski, B. (1996) Gravitational microlensing in the Local Group. *Annual Review of Astronomy and Astrophysics*, 34, 419
- Penny, M.T. (2013) Speeding up low-mass planetary microlensing simulations and modelling: the Caustic Region Of Influence (CROIN). *arXiv:1311.1050*
- Perryman, M.A.C. (2011) *The Exoplanet Handbook*. Cambridge University Press, The Edinburgh Building, Cambridge CB2 8RU, UK

- Petrou, M. (1981) *Dynamical Models of Spheroidal Systems*. Ph.D. thesis, University of Cambridge
- Petters, A.O., Levine, H. & Wambsganss, J. (2001) *Singularity theory and gravitational lensing*, volume 21 of *Progress in mathematical physics*. Birkhäuser
- Poindexter, S., Afonso, C., Bennett, D.P., Glicenstein, J.F., Gould, A., Szymański, M.K. & Udalski, A. (2005) Systematic Analysis of 22 Microlensing Parallax Candidates. *ApJ*, 633, 914
- Poleski, R., Udalski, A., Dong, S., Szymański, M.K., Soszyński, I., Kubiak, M., Pietrzyński, G., Kozłowski, S., Pietrukowicz, P., Ulaczyk, K., Skowron, J., Wyrzykowski, Ł. & Gould, A. (2014) Super-massive Planets around Late-type Stars — the Case of OGLE-2012-BLG-0406Lb. *ApJ*, 782, 47
- Pratt, M.R., Alcock, C., Allsman, R.A., Alves, D., Axelrod, T.S., Becker, A., Bennett, D.P., Cook, K.H., Freeman, K.C., Griest, K., Guern, J., Lehner, M., Marshall, S.L., Peterson, B.A., Quinn, P.J., Reiss, D., Rodgers, A.W., Stubbs, C., Sutherland, W. & Welch, D. (1995) Real-time Detection of Gravitational Microlensing. *arXiv:astro-ph/9508039*
- Proft, S., Demleitner, M. & Wambsganss, J. (2011) Prediction of astrometric microlensing events during the Gaia mission. *A&A*, 536, A50
- Rattenbury, N.J., Bond, I.A., Skuljan, J. & Yock, P.C.M. (2002) Planetary microlensing at high magnification. *MNRAS*, 335, 159
- Refsdal, S. (1966) On the possibility of determining the distances and masses of stars from the gravitational lens effect. *MNRAS*, 134, 315
- Rhie, S.H. (1997) Infimum microlensing amplification of the maximum number of images of n-point lens systems. *The Astrophysical Journal*, 484, 63
- Sahu, K.C., Bond, H.E., Anderson, J. & Dominik, M. (2014) Microlensing Events by Proxima Centauri in 2014 and 2016: Opportunities for Mass Determination and Possible Planet Detection. *ApJ*, 782, 89
- Sahu, K.C., Casertano, S., Livio, M., Gilliland, R.L., Panagia, N., Albrow, M.D. & Potter, M. (2001) Gravitational microlensing by low-mass objects in the globular cluster M22. *Nature*, 411, 1022
- Schneider, P., Ehlers, J. & Falco, E.E. (1992) *Gravitational Lenses*. Springer
- Schneider, P. & Weiß, A. (1986) The two-point-mass lens: detailed investigation of a special asymmetric gravitational lens. *A&A*, 164, 237
- Schramm, T. & Kayser, R. (1987) A simple imaging procedure for gravitational lenses. *A&A*, 174, 361

- Skowron, J., Udalski, A., Gould, A., Dong, S., Monard, L.A.G., Han, C., Nelson, C.R., McCormick, J., Moorhouse, D., Thornley, G., Maury, A., Bramich, D.M., Greenhill, J., Kozłowski, S., Bond, I., Poleski, R., Wyrzykowski, L., Ulaczyk, K., Kubiak, M., Szymanski, M.K. et al. (2011) Binary microlensing event OGLE-2009-BLG-020 gives a verifiable mass, distance and orbit predictions. *ApJ*, 738, 87
- Skowron, J., Wyrzykowski, Ł., Mao, S. & Jaroszyński, M. (2009) Repeating microlensing events in the OGLE data. *MNRAS*, 393, 999
- Snodgrass, C., Horne, K. & Tsapras, Y. (2004) The abundance of Galactic planets from OGLE-III 2002 microlensing data. *MNRAS*, 351(3), 967
- Street, R.A., Choi, J.Y., Tsapras, Y., Han, C., Furusawa, K., Hundertmark, M., Gould, A., Sumi, T., Bond, I.A., Wouters, D., Zellem, R., Udalski, A., Collaboration, T.R., Snodgrass, C., Horne, K., Dominik, M., Browne, P., Kains, N., Bramich, D.M., Bajek, D. et al. (2013) MOA-2010-BLG-073L: An M-dwarf with a Substellar Companion at the Planet/Brown Dwarf Boundary. *ApJ*, 763, 67
- Sumi, T., Kamiya, K., Bennett, D.P., Bond, I.A., Abe, F., Botzler, C.S., Fukui, A., Furusawa, K., Hearnshaw, J.B., Itow, Y., Kilmartin, P.M., Korpela, A., Lin, W., Ling, C.H., Masuda, K., Matsubara, Y., Miyake, N., Motomura, M., Muraki, Y., Nagaya, M. et al. (2011) Unbound or distant planetary mass population detected by gravitational microlensing. *Nature*, 473, 349
- Szymański, M.K., Udalski, A., Soszyński, I., Kubiak, M., Pietrzyński, G., Poleski, R., Wyrzykowski, L. & Ulaczyk, K. (2011) The Optical Gravitational Lensing Experiment. OGLE-III Photometric Maps of the Galactic Bulge Fields. *AcA*, 61, 83
- Thompson, A.C., Fluke, C.J., Barnes, D.G. & Barsdell, B.R. (2010) Teraflop per second gravitational lensing ray-shooting using graphics processing units. *NewA*, 15, 16
- Tsapras, Y., Horne, K., Kane, S. & Carson, R. (2003) Microlensing limits on numbers and orbits of extrasolar planets from the 1998-2000 OGLE events. *MNRAS*, 343, 1131
- Udalski, A. (2003) The Optical Gravitational Lensing Experiment. Real Time Data Analysis Systems in the OGLE-III Survey. *AcA*, 53, 291
- Udalski, A., Szymanski, M., Kaluzny, J., Kubiak, M., Mateo, M., Krzeminski, W. & Paczynski, B. (1994) The Optical Gravitational Lensing Experiment. The Early Warning System: Real Time Microlensing. *AcA*, 44, 227
- Udalski, A., Szymański, M., Kałużny, J., Kubiak, M., Krzeminski, W., Mateo, M., Preston, G.W. & Paczynski, B. (1993) The Optical Gravitational Lensing Experiment. Discovery of the first candidate microlensing event in the direction of the Galactic bulge. *Acta Astronomica*, 43, 289
- Udalski, A., Szymański, M., Kałużny, J., Kubiak, M. & Mateo, M. (1992) The Optical Gravitational Lensing Experiment. *Acta Astronomica*, 42, 253

- Vermaak, P. (2007) *Fitting binary lens gravitational microlensing events with example-based algorithms*. Ph.D. thesis, University of Cape Town
- Wambsganss, J. (1990) *Gravitational Microlensing*. Ph.D. thesis, Ludwig-Maximilians-Universität München
- Wambsganss, J. (1997) Discovering Galactic planets by gravitational microlensing: magnification patterns and light curves. *MNRAS*, 284(2), 172
- Wambsganss, J. (1999) Gravitational lensing: numerical simulations with a hierarchical tree code. *Journal of Computational and Applied Mathematics*, 109, 353
- Witt, H.J. & Mao, S. (1994) Can lensed stars be regarded as pointlike for microlensing by MACHOs? *ApJ*, 430, 505
- Witt, H.J. & Petters, A.O. (1993) Singularities of the one- and two-point mass gravitational lens. *Journal of Mathematical Physics*, 34, 4093
- Witt, H.J. (1990) Investigation of high amplification events in light curves of gravitationally lensed quasars. *A&A*, 236, 311
- Wolszczan, A. & Frail, D.A. (1992) A planetary system around the millisecond pulsar PSR1257 + 12. *Nature*, 355, 145
- Yee, J.C. (2013) WFIRST Planet Masses from Microlens Parallax. *ApJL*, 770, L31
- Yee, J.C., Shvartzvald, Y., Gal-Yam, A., Bond, I.A., Udalski, A., Kozłowski, S., Han, C., Gould, A., Skowron, J., Suzuki, D., Abe, F., Bennett, D.P., Botzler, C.S., Chote, P., Freeman, M., Fukui, A., Furusawa, K., Itow, Y., Kobara, S., Ling, C.H. et al. (2012) MOA-2011-BLG-293Lb: A Test of Pure Survey Microlensing Planet Detections. *ApJ*, 755, 102
- Zub, M., Cassan, A., Heyrovský, D., Fouqué, P., Stempels, H.C., Albrow, M.D., Beaulieu, J.P., Brilliant, S., Christie, G.W., Kains, N., Kozłowski, S., Kubas, D., Wambsganss, J., Batista, V., Bennett, D.P., Cook, K., Coutures, C., Dieters, S., Dominik, M., Dominis Prester, D. et al. (2011) Limb-darkening measurements for a cool red giant in microlensing event OGLE 2004-BLG-482. *A&A*, 525, A15